

**AD-A251 590**

PL-TR-91-2286



2

YIELD AND DISCRIMINATION STUDIES IN  
STABLE CONTINENTAL REGIONS

Brian J. Mitchell

Saint Louis University  
221 N. Grand Blvd.  
St. Louis, MO 63103

18 November 1991

DTIC  
ELECTE  
MAY 20 1992  
S D

Final Report  
16 February 1989-9 July 1991

APPROVED FOR PUBLIC RELEASE: DISTRIBUTION UNLIMITED.

**92-13359**



PHILLIPS LABORATORY  
AIR FORCE SYSTEMS COMMAND  
HANSOM AIR FORCE BASE, MASSACHUSETTS 01731-5000

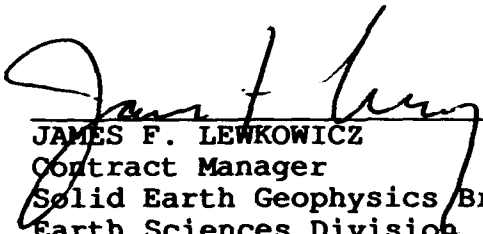
92 5 19 029

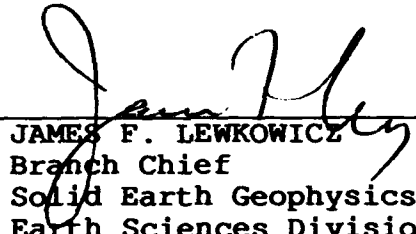
SPONSORED BY  
Defense Advanced Research Projects Agency  
Nuclear Monitoring Research Office  
ARPA ORDER NO. 5307


MONITORED BY  
Phillips Laboratory  
Contract F19628-89-K-0021

The views and conclusions contained in this document are those of the authors and should not be interpreted as representing the official policies, either expressed or implied, of the Defense Advanced Research Projects Agency or the U.S. Government.

This technical report has been reviewed and is approved for publication.

  
JAMES F. LEWKOWICZ  
Contract Manager  
Solid Earth Geophysics Branch  
Earth Sciences Division

  
JAMES F. LEWKOWICZ  
Branch Chief  
Solid Earth Geophysics Branch  
Earth Sciences Division

  
DONALD H. ECKHARDT, Director  
Earth Sciences Division

This report has been reviewed by the ESD Public Affairs Office (PA) and is releasable to the National Technical Information Service (NTIS).

Qualified requestors may obtain additional copies from the Defense Technical Information Center. All others should apply to the National Technical Information Service.

If your address has changed, or if you wish to be removed from the mailing list, or if the addressee is no longer employed by your organization, please notify PL/IMA, Hanscom AFB, MA 01731-5000. This will assist us in maintaining a current mailing list.

Do not return copies of this report unless contractual obligations or notices on a specific document requires that it be returned.

# REPORT DOCUMENTATION PAGE

Form Approved  
OMB No. 0704-0188

Public reporting burden for this collection of information is estimated to average 1 hour per response, including the time for reviewing instructions, searching existing data sources, gathering and maintaining the data needed, and completing and reviewing the collection of information. Send comments regarding this burden estimate or any other aspect of this collection of information, including suggestions for reducing this burden, to Washington Headquarters Services, Directorate for Information Operations and Reports, 1215 Jefferson Davis Highway, Suite 1204 Arlington, VA 22202-4302, and to the Office of Management and Budget, Paperwork Reduction Project (0704-0188), Washington, DC 20503.

1. AGENCY USE ONLY (Leave blank) 2. REPORT DATE  
Nov. 18, 1991 3. REPORT TYPE AND DATES COVERED  
Final Technical Report (2/16/89-7/9/91)

4. TITLE AND SUBTITLE  
Yield and Discrimination Studies in  
Stable Continental Regions 5. FUNDING NUMBERS  
Contract F19628-89-K-0021  
PE 61101E  
PR 9A10 TADA WUAK

6. AUTHOR(S)  
Brian J. Mitchell

7. PERFORMING ORGANIZATION NAME(S) AND ADDRESS(ES)  
Saint Louis University  
Office of Research Administration  
221 N. Grand Blvd.  
St. Louis, MO 63103 8. PERFORMING ORGANIZATION  
REPORT NUMBER

9. SPONSORING/MONITORING AGENCY NAME(S) AND ADDRESS(ES)  
Phillips Laboratory  
Hanscom AFB, MA 01731-5000  
Contract Manager: James Lewkowicz/GEH 10. SPONSORING/MONITORING  
AGENCY REPORT NUMBER  
PL-TR-91-2286

11. SUPPLEMENTARY NOTES

12a. DISTRIBUTION/AVAILABILITY STATEMENT  
Approved for public release  
Distribution unlimited 12b. DISTRIBUTION CODE

13. ABSTRACT (Maximum 200 words)  
This report presents the results of several studies related to research on yield determination and discrimination between earthquakes and explosions. The work proceeded along two lines: (1) the determination of attenuation of Lg coda and intermediate-period surface waves, and (2) discrimination between small earthquakes and explosions in the central United States.  
The attenuation studies in the first four chapters of this report conclude that (1) that the high frequency dependence of Lg coda Q in the Basin and Range can be caused by a rapid increase of Q at mid-crustal depths, (2) that patterns of upper crustal Q and upper mantle Q correlate throughout the western United States, (3) that Lg coda Q values in the southern USSR, China and southeastern Asia vary between 200 and 700, and (4) that attenuation across the Arabian Peninsula is high for a shield region. Discrimination studies indicate (1) that a neural network approach can be effective in determining source depth, and (2) decreases of amplitude with frequency in the central United States are more rapid for earthquakes than for explosions.

14. SUBJECT TERMS  
Attenuation Lg Waves Yield Discrimination  
Neural networks Q 15. NUMBER OF PAGES  
192 16. PRICE CODE

17. SECURITY CLASSIFICATION  
OF REPORT  
Unclassified 18. SECURITY CLASSIFICATION  
OF THIS PAGE  
Unclassified 19. SECURITY CLASSIFICATION  
OF ABSTRACT  
Unclassified 20. LIMITATION OF ABSTRACT  
SAR

# TABLE OF CONTENTS

Chapter 1 . . . . .	1
The Frequency Dependence of $Q_{Lg}$ and its Relation to Crustal Anelasticity in the Basin and Range Province	
Chapter 2 . . . . .	25
Upper Mantle Anelasticity and Tectonic Evolution of the Western United States from Surface Wave Attenuation	
Chapter 3 . . . . .	77
Lg Coda Q Variation across Eurasia	
Chapter 4 . . . . .	92
Attenuation of Surface Waves across the Arabian Penninsula	
Chapter 5 . . . . .	126
Learned Estimation of Focal Depths with Multilayered Neural Networks: Application to Continental and Oceanic Earthquakes	
Chapter 6 . . . . .	170
Discrimination Studies Using Regional Phases in the Central United States	



Accession For	
NTIS GRA&I	<input checked="" type="checkbox"/>
DTIC TAB	<input type="checkbox"/>
Unannounced	<input type="checkbox"/>
Justification	
By	
Distribution/	
Availability Codes	
Dist	Avail and/or Special
A-1	

# **Chapter 1**

**The frequency Dependence of  $Q_{Lg}$  and its  
Relation to Crustal Anelasticity in the  
Basin and Range Province**

**by**

**Brian J. Mitchell**

## Abstract

Observed  $Q$  values for 1-Hz  $L_g$  waves which traverse the Basin and Range province exhibit a dependence on frequency which varies as  $f^{0.4-0.6}$ . By contrast, the frequency dependence of intrinsic  $Q$  for shear waves in the crust of the same region is much lower and may be nonexistent. These apparently conflicting observations can be explained by a frequency-independent layered model of shear-wave  $Q$  which has very low values in the upper crust and rapidly increasing values at greater depths. The shear-wave  $Q$  model which best explains reported values of  $Q_{L_g}$  and its frequency dependence consists of an 8-km thick low- $Q$  layer (60 or less) overlying  $Q$  values as high as 1000 or more at mid-crustal depths. The low  $Q_\beta$  values in the upper crust are best explained by the presence of fluids in interconnected cracks and pore space. At greater depths, increasing lithostatic pressure closes the cracks, leading to the higher  $Q_\beta$  values. This model also predicts fundamental-mode Rayleigh wave attenuation coefficients which agree with observed values. The result of this study contrasts with that of earlier work in high- $Q$  regions of the eastern United States where shear-wave  $Q$  in the upper crust must vary with frequency to explain the observed attenuation of both fundamental-mode Rayleigh waves and  $L_g$ .

These results indicate that whereas the frequency-dependence of shear-wave  $Q$  is an intrinsic property of crustal material, the frequency dependence of  $Q_{L_g}$  arises from both the intrinsic frequency dependence of crustal material and its layered structure. A notation is suggested which distinguishes between the frequency dependence of  $Q_{L_g}$  and shear-wave  $Q$ .

## Introduction

Data that can be used to study the attenuation of the phase Lg and its coda, especially at frequencies near 1 Hz, has increased tremendously in recent years. Observations indicate that  $Q$  for these waves varies regionally, being relatively high in old stable regions and relatively low in younger, tectonically active regions (Nuttli, 1973; Singh and Herrmann, 1983; Cong and Mitchell, 1988).  $Q$  values for both Lg ( $Q_{Lg}$ ) and its coda ( $Q_c$ ) at frequencies near 1 Hz exhibit similar values, being within 10-15% of one another for all regions in the world where both have been determined (Nuttli, 1988). The regional variations of  $Q_{Lg}$  and  $Q_c$  occur in patterns which vary in the same way as regional variations in crustal shear wave  $Q$  ( $Q_\beta$ ) in the upper crust obtained from surface wave attenuation studies (Mitchell, 1975; Cheng and Mitchell, 1981; Hwang and Mitchell, 1987). The frequency dependences of  $Q_{Lg}$  and  $Q_c$  also vary regionally, but in the opposite sense as the  $Q$  values; they are lower in stable regions and higher in tectonically active regions (Nuttli, 1988).

Since Lg is a guided wave, controlled predominantly by crustal properties, it can be expected that the regional variation of  $Q_{Lg}$  and  $Q_c$  and their frequency dependences are caused by lateral changes in the anelastic and scattering properties of crustal rock. Models of  $Q_\beta$  which explain the attenuation of both Lg waves at 1 Hz and fundamental-mode surface waves at intermediate frequencies have been developed for several regions of the world, including the eastern United States (Mitchell, 1980) and western United States (Mitchell, 1981). An important result of those studies is that the frequency dependence of  $Q_\beta$  must be relatively high in the high- $Q$  crust of the central and eastern United States, but is low or non-existent in the low- $Q$  crust of the western United States for frequencies of about 1 Hz and lower. Later work

(Cong and Mitchell, 1988) confirmed the earlier results in North America and showed that the same conclusion also holds for South America and India.

The results described above, that the frequency dependence of  $Q_{Lg}$  usually decreases with increasing values of  $Q_{Lg}$  whereas the frequency dependence of  $Q_{\beta}$  increases with increasing  $Q_{\beta}$ , seem to be contradictory. The main purpose of this paper is to explain that apparent inconsistency. It will be shown that the frequency dependence of  $Q_{Lg}$  in the Basin-and Range can be produced by a layered  $Q_{\beta}$  structure. Thus, frequency dependence of  $Q_{\beta}$ , such as that which characterizes crustal rocks of the eastern United States, is not required in the Basin and Range. A standard notation will be proposed which distinguishes between the frequency dependence of  $Q_{Lg}$ ,  $Q_c$ , and  $Q_{\beta}$ .



## Observations of $Q_{Lg}$ and $Q_c$ in the Basin-and-Range

Xie and Mitchell (1990) have recently determined  $Q$  and its frequency dependence for both  $Lg$  and  $Lg$  coda waves in the Basin-and-Range province. Using the relation  $Q_{Lg}(f) = Q_0 f^\eta$ , where  $Q_0$  is  $Q_{Lg}$  at 1 Hz and  $\eta$  is a frequency-dependence exponent, they found that  $Q_{Lg}$  can be described by  $Q_{Lg}(f) = (267 \pm 56)f^{(0.37 \pm 0.06)}$  and that  $Lg$  coda  $Q$  can be described by  $Q_c(f) = (275 \pm 26)f^{(0.36 \pm 0.03)}$  at frequencies between 0.2 and 2.5 Hz. Their determinations utilized a stacked spectral ratio (SSR) method (Xie and Nuttli, 1988) which provides stable determinations of  $Q$  with variances which are much smaller than those associated with previously used methods. Singh and Herrmann (1983) obtained  $Q_c(f) = (250 \pm 50)f^{(0.45 \pm 0.05)}$  using a predominant frequency analysis and Chavez and Priestley (1986) obtained  $Q_c(f) = (214 \pm 15)f^{(0.54 \pm 0.09)}$  as average values over a somewhat broader region centered in the Basin-and-Range province.

The similarity of the  $Q$  values for  $Lg$  waves and coda waves and the similarity of their frequency dependences found by Xie and Mitchell (1990) suggest that  $Q_{Lg}$  and  $Q_c$  can be used interchangeably when using those waves to infer anelastic properties of the crust or in using the attenuation of one or the other of those waves to measure magnitudes of earthquakes or nuclear explosions from  $Lg$  waves, at least in low- $Q$  regions like the Basin-and-Range province. That similarity is particularly convenient when determining crustal models of  $Q_\beta$  which explain  $Lg$  attenuation. It means that amplitudes of  $Lg$  waves from synthetic seismograms at various distances can be used to determine  $Q_{Lg}$  values predicted by crustal models and these can be compared with observed  $Q_c$  values which are more abundant than observed  $Q_{Lg}$  values.

Implications of the equivalence of  $Q_{Lg}$  and  $Q_c$  were discussed by Xie and Mitchell (1990). They noted that if the energy flux model of Frankel and Wennerberg (1987) is valid at distances of several hundred to 2000 km in the Basin and Range province the equivalence would suggest that intrinsic  $Q$  is the dominant factor affecting wave attenuation there and the effect of scattering  $Q$  is much smaller. Very low values of  $Q_\beta$  in the upper crust of the Basin-and-Range have been reported by Cheng and Mitchell (1981), Patton and Taylor (1984), and Lin (1989) from studies of surface waves at intermediate frequencies. Because of the relatively long wavelengths used in the surface wave studies (20 - 150 km) it is likely that those low  $Q_\beta$  values correspond to intrinsic values. Because those  $Q_\beta$  values are so low (50 - 100), it is likely that attenuation over the frequency range 0.2 to 2.5 Hz used by Xie and Mitchell (1990) is also dominated by intrinsic  $Q$  effects, as suggested by Frankel and Wennerberg (1987) for the Anza region of southern California. In the following sections, we consequently assume that attenuation at both low frequencies and frequencies near 1 Hz is dominated by intrinsic  $Q$  and can be modeled using that assumption.

### Crustal $Q_\beta$ Models for the Basin-and-Range

Crustal  $Q_\beta$  models for the Basin-and-Range province have recently been obtained by Patton and Taylor (1984) and Lin (1989). Although they both exhibit  $Q_\beta$  values which are low compared to models for eastern North America, they differ from one another in the distribution of those values.  $Q_\beta^{-1}$  values for the model of Patton and Taylor (1984) increase continuously from the near surface to upper mantle depths whereas the model of Lin (1989) includes a high-Q zone (low  $Q_\beta^{-1}$ ) at depths between about 12 and 25 km (Figure 1). Both models were obtained using the assumption that  $Q_\beta$  is independent of frequency. Frequency-independent models can explain the attenuation of both fundamental-mode surface waves and 1 Hz Lg waves in that region (Mitchell, 1981). Figure 1 also shows a model of the eastern United States (Cong and Mitchell, 1988) which must be frequency dependent in order to explain the attenuation of both fundamental-mode surface waves and Lg.

Differences between the two Basin-and-Range models probably occur because the two studies used different methods to determine the attenuation of surface waves. Patton and Taylor (1984) used the method of Tsai and Aki (1969) which obtains spectral amplitudes at many stations surrounding a seismic event and solves simultaneously for fundamental-mode surface wave attenuation coefficients and the moment of the events. The method is most effective in regions where Q has little lateral variation, but is susceptible to systematic errors, which can give attenuation values which are either too high or too low, depending on path configuration, in regions where Q varies laterally (Yacoub and Mitchell, 1977). Observations by Singh and Herrmann (1983) in the Basin-and-Range indicate that Lg coda Q varies between about 200 and 300 in that region. Thus, the model of Patton and Taylor (1984)

could be biased due to systematic errors in surface wave attenuation determinations.

The model of Lin (1989) was obtained by inverting two-station measurements of both fundamental-mode and first higher-mode Rayleigh waves. Those measurements should give average values even along paths where  $Q$  varies laterally. That model includes a high- $Q$  zone at mid-crustal depths. Hough and Anderson (1988), in a study of local earthquake recordings, reported a similar zone of high  $Q$  values at somewhat shallower depths (5-12 km) beneath the Anza array in southern California.

The model of Lin (1989) will be used as a starting point for the computations of this study. Three modified forms of his model are used, all of which include a low- $Q_\beta$  layer with a value of 60 in the upper crust. Stacked spectral ratios are computed for three models, one in which the low- $Q$  layer is 6 km, another 8 km, and another 10 km thick. At greater depths the  $Q_\beta$  values of Lin (1989) are used.

### Predicted Values for $Q_{Lg}$

If attenuation in the Basin-and-Range province is dominated by intrinsic effects, then the attenuation of Lg can be predicted for crustal models which have been determined for that region. In the present study, synthetic seismograms for the Lg phase were computed at several distances for velocity and  $Q_\beta$  models for the crust and upper mantle of the Basin-and-Range and the attenuation of Lg was determined using the stacked spectral ratio (SSR) method of Xie and Nuttli (1988); predicted Lg Q values were thus determined using the same method that was used to obtain observed Q values. The SSR method was applied to synthetic seismograms of Lg computed by mode summation (e.g., Wang, 1981). 20 seismograms were computed over the distance range 300 - 1250 km for  $Q_\beta$  models and velocity models obtained by Patton and Taylor (1984) and Lin (1989). Example seismograms computed at distances between 400 km and 1200 km appear in Figure 2 for the velocity and Q models of Lin (1989). The rapid loss of high frequencies caused by low-Q material in the upper crust is readily apparent.

The solid lines in Figure 3 denote stacked spectral ratios predicted by three modified forms of the model of Lin (1989) in which a low- $Q_\beta$  surface layer overlies much higher  $Q_\beta$  values at greater depths. The calculated values for those models are compared to observed values of Xie and Mitchell (1990) over the frequency range 0.3 - 3.0 Hz. The best-fitting model is that with an 8 km thick low-Q zone; the SSR for this model is described by the relation  $Q_{Lg} = (248 \pm 27)f^{(0.5 \pm 0.2)}$ . The model with a 6 km thick low-Q layer produces higher  $Q_0$  and  $\eta$  values and the model with a 10 km thick low-Q layer produces lower values. Results for the model with an 8 km thick layer compare well with the relation  $Q_{Lg} = (267 \pm 56)f^{(0.4 \pm 0.1)}$  obtained by Xie and Mitchell (1990) from stacked spectral ratios of observed Lg waves. The model

also predicts attenuation coefficient values of the fundamental Rayleigh mode at intermediate periods (6 - 35 s) which agree satisfactorily with the observed value of Lin (1989) as shown in Figure 4. The only discrepancy is at a period of 6 s where the predicted value is slightly outside the one standard deviation range of the observations. The model with a 10 km thick low-Q zone predicts values which are in even better agreement in the 6 - 7 s range, whereas the model with the 6 km thick layer predicts values which are substantially lower than observed values. Because it provides the best fit to both Lg and fundamental Rayleigh wave data, the model with an 8 km thick low-Q zone is taken as the best model for this region. The dramatic increase of  $Q_\beta$  at mid-crustal depths is most easily explained as being caused by the closure of cracks due to increasing lithostatic pressure. As suggested by Mitchell (1975, 1980), the low  $Q_\beta$  values in the upper crust imply the presence of fluid-filled cracks and pore space. Reductions in Q due to fluid movement through the crust have been described quantitatively by Mavko and Nur (1975) and O'Connell and Budiansky (1977). Brace and Kohlstedt (1980) summarized the results of Brace (1972) and Brace (1980) indicating that relatively high crustal permeability extends to 8 km and could extend to greater depths. The depth to the high- $Q_\beta$  zone obtained in this study is therefore consistent with depths commonly associated with enhanced crustal permeability. The dashed line in Figure 3 was produced by the model of Patton and Taylor (1984). The absence of a high-Q layer in that model causes observed  $Q_{Lg}$  values and frequency-dependence values to be too low.

The modified  $Q_\beta$  model of Lin (1989) which produced excellent agreement with observed values of  $Q_{Lg}$  and its frequency dependence is a frequency-independent model. This result indicates that the frequency dependence of  $Q_{Lg}$  near 1 Hz which is observed in the Basin and Range can

be produced by a layered structure in which  $Q_\beta$  increases rapidly with depth at mid-crustal depths. It is possible, however, that  $Q_\beta$  in the deeper portions of the model, particularly the high-Q region, can be frequency dependent. When  $Q_\beta$  is high, resolution of  $Q_\beta$  values is relatively poor, so that frequency dependence cannot easily be detected (Mitchell, 1980).

A high-Q layer was also inferred by Hough and Anderson (1988) using body waves from local earthquakes at frequencies between 15 and 100 Hz for the Anza region in southern California. Their  $Q_\beta$  model consisted of a high-Q layer ( $> 2000$ ) at depths between 5 and 12 km sandwiched between a 5-km thick surface layer with  $Q_\beta$  values of about 500 and deeper material with  $Q_\beta$  values of about 800. Those values are much higher than those of the present study even though  $Q_c$  values there are lower than those of the Basin and Range (Singh and Herrmann, 1983). Their model therefore suggests that crustal  $Q_\beta$  values increase with frequency beginning at frequencies somewhere between 5 Hz and 15 Hz.

The depth range of the high-Q zone in the model of Hough and Anderson (1988) corresponds to the range over which most earthquakes occur in that region. The high-Q zone in the model of Lin (1989) lies between depths of about 12 and 25 km. The depth distribution of earthquakes has been determined in the western Great Basin in a region near the western extent of our region of study (Vetter and Ryall, 1983). The greatest number of earthquakes occur at depths between 10 and 15 km in a zone which overlaps the high-Q zone of the model of Lin (1989), and earthquakes occur in smaller numbers at depths down to the base of the high-Q zone. Thus, it is possible that the depth distribution of earthquakes in the Basin-and-Range province is related to the  $Q_\beta$  distribution there.

## A Classification for the Frequency Dependence of $Q_{Lg}$ , $Q_c$ , and $Q_\beta$

Expressions for the internal friction ( $Q^{-1}$ ) of surface waves, assuming that damping losses are small enough that  $Q^{-2}$  can be neglected, were given by Anderson *et al.* (1965). The equation for Rayleigh waves is

$$Q_R^{-1}(\omega) = \sum_{l=1}^L \left[ \left( \frac{\beta_l}{C_R} \frac{\partial C_R}{\partial \beta_l} \right)_{\omega\alpha} Q_{\beta l}^{-1} + \left( \frac{\alpha_l}{C_R} \frac{\partial C_R}{\partial \alpha_l} \right)_{\omega\beta} Q_{\alpha l}^{-1} \right] \quad (1)$$

where the subscript  $l$  is the layer index, the subscripts  $R$ ,  $\alpha$  and  $\beta$  identify Rayleigh, compressional, and shear waves, respectively,  $\omega$  is angular frequency, and  $C_R$  is Rayleigh wave phase velocity. The subscripts  $\omega$ ,  $\alpha$ , and  $\beta$  indicate that those quantities are held constant when the partial derivatives are computed.

This equation can be used to calculate  $Q_R^{-1}$  for any Rayleigh mode by using the appropriate velocities, partial derivatives, and intrinsic  $Q$  values. Mitchell (1980) extended this expression to incorporate shear-wave  $Q$  values which vary with frequency as

$$Q_{\beta l}(f) = C_l f^\zeta \quad (2)$$

where  $\zeta$  is an exponent which describes the frequency dependence of  $Q_\beta$ . Nuttli (1986) assumed that the frequency dependence described by Mitchell (1980) for  $Q_\beta$  also pertained to  $Q_{Lg}$ . However, equations (1) and (2) indicate that frequency dependence of  $Q_R^{-1}$  can be caused either by frequency-dependent  $Q_\beta$  in the crust or by an appropriately layered structure in which  $Q_\beta$  is independent of frequency. Results of the present study indicate that the layered structure in the Basin and Range causes  $Q_{Lg}$  to increase with frequency. That increase occurs because higher frequencies include a greater number of higher modes than low frequencies and those higher-order modes sample more deeply in the crust than lower order modes. A high- $Q$  lower



crust will therefore produce a positive frequency dependence of  $Q_{Lg}$ . Thus, the frequency dependence of  $Q_{Lg}$  and  $Q_\beta$  should be described by two different parameters. I therefore propose that the frequency dependence of the attenuation of Lg waves be described by the parameter  $\eta$  and that the frequency dependence of internal friction for shear waves be described by the parameter  $\zeta$ .  $Q_{Lg}$  would then be described by

$$Q_{Lg}(f) = Q_0 f^\eta. \quad (3)$$

If the crust and upper mantle were comprised of flat layers with laterally uniform elastic and anelastic properties, equations (1) and (2) could provide a good approximation for the effect of anelasticity on the attenuation of Lg waves which, as indicated by equation (3), may have a different frequency dependence. It is known, however, that heterogeneities distributed throughout the lithosphere produce a long coda following the Lg wave which cannot be replicated in synthetic seismograms computed for plane-layered structures (Aki and Chouet, 1975). Since the Lg coda is composed of scattered waves which travel longer paths than that taken by Lg, it appears that the frequency dependence of the attenuation of Lg coda should be described by yet a third parameter which I tentatively designate  $\eta'$ . Then

$$Q_c(f) = Q_0' f^{\eta'}. \quad (4)$$

In low-Q regions, such as the Basin-and-Range, it appears that very low intrinsic Q material in the crust attenuates scattered waves at the same rate as it attenuates the direct Lg wave. Thus the relations  $Q_0' = Q_0$  and  $\eta' = \eta$  may be appropriate for all low-Q regions. Further work, using methods capable of providing stable measurements of  $Q_{Lg}$  and  $Q_c$  and their frequency dependences, will be necessary in high-Q regions to see if the relations  $Q_0' = Q_0$  and  $\eta' = \eta$  hold everywhere.

## Conclusions

All of the frequency dependence of  $Q_{Lg}$  in the Basin and Range province can be explained by a layered frequency-independent model in which  $Q_\beta$  increases rapidly with depth from very low values ( $< 100$ ) in the upper 8 km of the crust to high values at greater depths. It is possible that the high- $Q$  layer is frequency dependent, but that that dependence cannot be detected because of poor resolution in high- $Q$  material. The change from low to high values of  $Q_\beta$  most likely occurs because of the closure of cracks produced by increasing lithostatic pressure with depth. The frequency independence of this model contrasts with results from the central and eastern United States where frequency dependence of  $Q_\beta$  in the upper crust is required to explain the attenuation of both fundamental-mode Rayleigh waves and  $Lg$  waves.

Frequency dependence of  $Q_{Lg}$  and its coda at frequencies near 1 Hz can therefore be caused by at least two factors, by layering in a frequency-independent  $Q_\beta$  model or by an intrinsic frequency dependence of  $Q_\beta$ . It is likely that both factors will prevail in many regions. The frequency dependence ( $\eta$ ) of  $Q_{Lg}$  and the frequency dependence ( $\zeta$ ) of  $Q_\beta$  are thus fundamentally different parameters and can differ greatly from one another. The frequency dependence ( $\eta'$ ) of  $Q_c$  may, in general, be different from both  $\eta$  and  $\zeta$ , but in the Basin and Range, at least it appears that  $\eta = \eta'$ , at least near 1 Hz. Since that equivalence occurs because of the rapid attenuation of scattered waves, it is likely that  $\eta = \eta'$  in other low- $Q$  regions. Further work is necessary to ascertain whether or not this is also true of high- $Q$  regions.

### **Acknowledgment**

I am grateful to Jia-kang Xie for providing his program for computing stacked spectral ratio values and to Wen-jack Lin who provided the Q model for the Basin-and-Range province used in this paper. The program for computing the synthetic seismograms used for the theoretical stacked spectral ratios was written by C.Y. Wang and R.B. Herrmann. This research was supported by the Advanced Research Projects Agency of the Department of Defense and was monitored by the Geophysics Laboratory under contract F19628-89-K-0021.

## References

- Aki, K., and B. Chouet, Origin of coda waves: source, attenuation, and scattering effects, *J. Geophys. Res.*, 80, 3322-3342, 1975.
- Anderson, D.L., A. Ben-Menahem, and C.B. Archambeau, Attenuation of seismic energy in the upper mantle, *J. Geophys. Res.*, 70, 1441-1448, 1965.
- Brace, W.F., Pore pressure in geophysics, in *Flow and Fracture of Rocks*, *Geophys. Mono. Ser.*, 16, edited by H.C. Heard, I.Y. Borg, N.L. Carter, and C.B. Raleigh, 265-273, AGU, Washington, DC, 1972.
- Brace, W.F., Permeability of crystalline and orgillaceous rocks, *Int. J. Rock Mech. Min. Sci.*, 17, 241-251, 1980.
- Brace, W.F., and D.L. Kohlstedt, Limits on lithospheric stress imposed by laboratory experiments, *J. Geophys. Res.*, 85, 6248-6252, 1980.
- Cheng, C.C., and B.J. Mitchell, Crustal Q structure in the United States from multi-mode surface waves, *Bull. Seism. Soc. Am.*, 71, 161-181, 1981.
- Cong, L., and B.J. Mitchell, Frequency dependence of crustal  $Q_\beta$  in stable and tectonically active regions, *PAGEOPH*, 127, 581-605, 1988.
- Frankel, A., and L. Wennerberg, Energy-flux model for seismic coda: separation of scattering and intrinsic attenuation, *Bull. Seism. Soc. Am.*, 77, 1223-1251, 1987.
- Hough, S.E., and J.G. Anderson, High-frequency spectra observed at Anza, California: Implications for Q structure, *Bull. Seism. Soc. Am.*, 78, 692-707, 1988.

- Hwang, H.J., and B.J. Mitchell, Shear velocities,  $Q_\beta$ , and the frequency dependence of  $Q_\beta$  in stable and tectonically active regions from surface wave observations, *Geophys. J. Roy. Ast. Soc.*, 90, 575-613, 1987.
- Lin, W.J., Rayleigh Wave Attenuation in the Basin and Range Province, M.S. Thesis, Saint Louis University, 55 pp., 1989.
- Mavko, G.M., and A. Nur, Melt squirt in the asthenosphere, *J. Geophys. Res.*, 80, 1444-1447, 1975.
- Mitchell, B.J., Regional Rayleigh wave attenuation in North America, *J. Geophys. Res.*, 80, 4904-4916, 1975.
- Mitchell, B.J., Frequency dependence of shear wave internal friction in the continental crust of eastern North America, *J. Geophys. Res.*, 85, 5212-5218, 1980.
- Mitchell, B.J., Regional variation and frequency dependence of  $Q$  in the crust of the United States, *Bull. Seism. Soc. Am.*, 78, 1531-1538, 1981.
- Nuttli, O.W., Seismic wave attenuation and magnitude relations for eastern North America, *J. Geophys. Res.*, 78, 876-885, 1973.
- Nuttli, O.W., Yield estimates of Nevada Test Site explosions obtained from seismic Lg waves, *J. Geophys. Res.*, 91, 2137-2151, 1986.
- Nuttli, O.W., Lg magnitudes and yield estimates for underground Novaya Zemlya nuclear explosions, *Bull. Seism. Soc. Am.*, 78, 873-884, 1988.
- O'Connell, R.J., and B. Budiansky, Viscoelastic properties of fluid-saturated cracked solids, *J. Geophys. Res.*, 82, 5719-5735, 1977.

- Patton, H.J., and S.R. Taylor, Q structure of the Basin and Range from surface waves, *J. Geophys. Res.*, 89, 6929-6940, 1984.
- Singh, S.K., and R.B. Herrmann, Regionalization of crustal coda Q in the continental United States, *J. Geophys. Res.*, 88, 527-538, 1983.
- Tsai, Y.B., and K. Aki, Simultaneous determination of the seismic moment and attenuation of seismic surface waves, *Bull. Seism. Soc. Am.*, 59, 275-287, 1969.
- Vetter, U.R., and A.S. Ryall, Systematic change of focal mechanism with depth in the western Great Basin, *J. Geophys. Res.*, 88, 8237-8250, 1983.
- Wang, C.Y., Wave Theory for Seismogram Synthesis, Ph.D. Dissertation, Saint Louis University, 235 pp., 1981.
- Xie, J., and B.J. Mitchell, Attenuation of multiphase surface waves in the Basin and Range province, Part I: Lg and Lg coda, *Geophys. J. Int.*, in press, 1990.
- Xie, J., and O.W. Nuttli, Interpretation of high-frequency coda at large distances: stochastic modelling and method of inversion, *Geophys. J.*, 95, 579-595, 1988.
- Yacoub, N.K., and B.J. Mitchell, Attenuation of Rayleigh wave amplitudes across Eurasia, *Bull. Seism. Soc. Am.*, 67, 751-769, 1977.

## Figure Captions

Figure 1. Models of  $Q_\beta^{-1}$  obtained from surface wave attenuation. The solid lines indicate a frequency-dependent model for the eastern United States for which  $Q_\beta$  varies as  $f^{0.5}$  (Cong and Mitchell, 1988). The dashed line is a frequency-independent model for the Basin-and-Range province. Both models explain the attenuation of fundamental-mode surface waves and 1-Hz Lg waves in the regions they represent.

Figure 2. Synthetic Lg seismograms computed by model summation (Wang, 1981) for distances between 400 and 1200 km. The seismograms were computed for along an azimuth of  $45^\circ$  from a vertical strike-slip fault at a depth of 5 km and oriented in a north-south direction. Seismograms were computed at 20 distances and stacked to obtain stacked spectral ratios using the method of Xie and Nuttli (1988). The time scale is reduced at each distance  $R$  using a reduction velocity of 5.0 km/s.

Figure 3. Stacked spectral ratios (circles) obtained by Xie and Mitchell (1990) for the Basin-and-Range province over frequencies between 0.3 and 3.0 hz. A least squares fit to this data gives  $Q_{Lg} = (267 \pm 56)f^{(0.4 \pm 0.1)}$ . The solid lines represent theoretically predicted values for modified versions of the model of Lin (1989) in which the upper crust is assigned a  $Q_\beta$  value of 60 and allowed to vary in thickness between 6 and 10 km. The dashed line represents theoretically predicted values for the model of Patton and Taylor (1984).

Figure 4. Attenuation coefficient values observed by Lin (1989) in the Basin and Range province. Vertical bars denote one standard deviation. Solid lines indicate values predicted by the  $Q_\beta$  model of the lower crust and

upper mantle in Figure 1 combined with an upper crust with a  $Q_\beta$  of 60. The thickness of that upper crustal layer varies, being 6, 8, and 10 km thick for three computations.



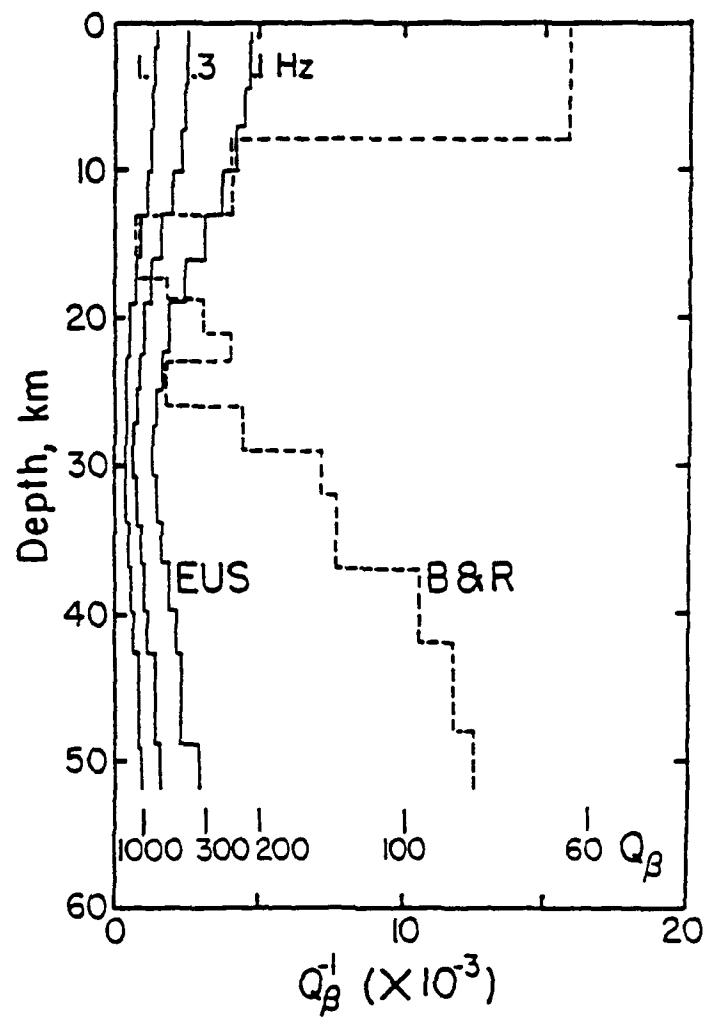


Figure 1

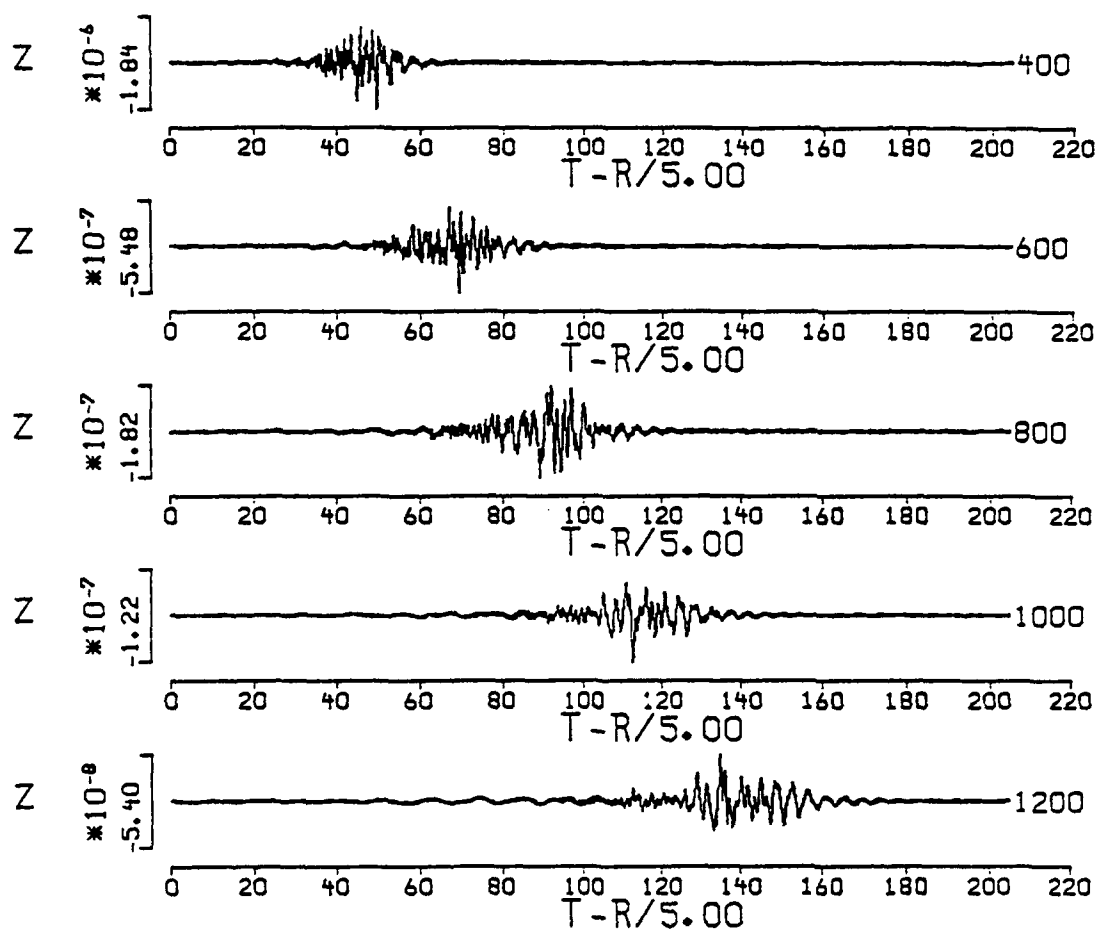


Figure 2

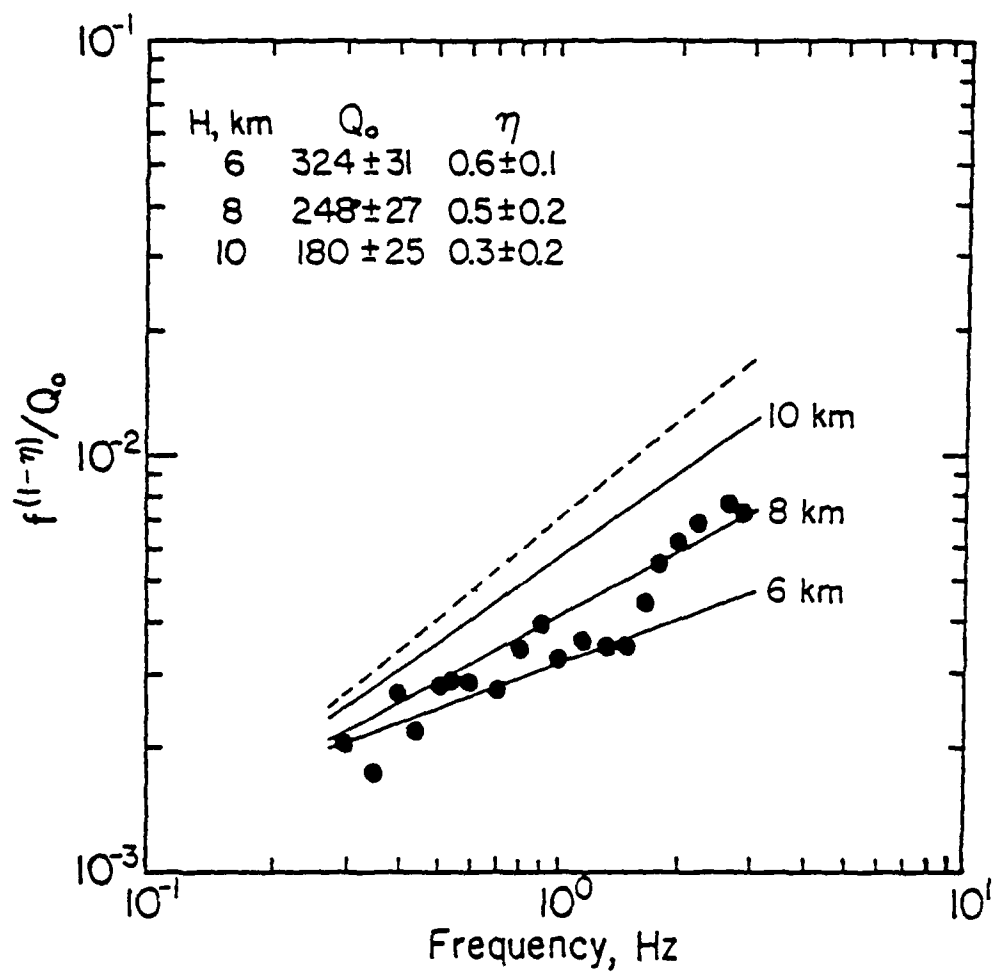


Figure 3

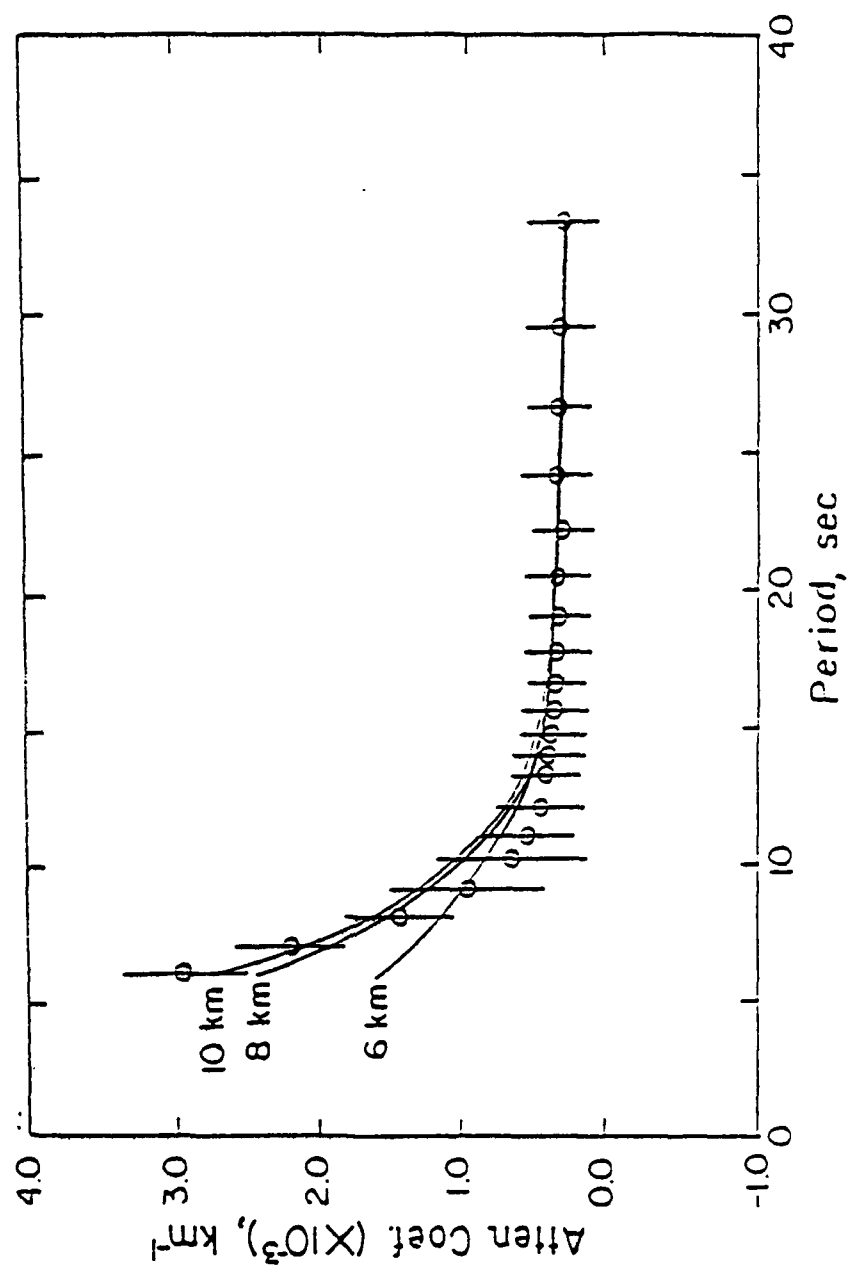


Figure 4

## **Chapter 2**

**Upper Mantle Anelasticity and Tectonic  
Evolution of the Western United States  
from Surface Wave Attenuation**

**by**

**Hanan H. Al-Khatib and Brian J. Mitchell**

## ABSTRACT

Rayleigh wave phase and group velocities and attenuation coefficients in the period range 18 to 120 sec have been determined for three regions along nine paths across the western United States using a two-station technique. The attenuation coefficients were found to increase from east to west between the Rocky Mountains and the Pacific coast.

Rayleigh wave group and phase velocities were inverted, using a differential procedure, to obtain shear wave velocity models for three regions. These velocity models were then used in an inversion process where  $Q_\beta^{-1}$  as a function of depth was obtained from observations of Rayleigh wave attenuation. The inversion results show that  $Q_\beta$  values in the upper mantle of the western United States are lowest for the coastal regions and westernmost Basin and Range, highest for the Rocky Mountains and western Great Plains. Intermediate  $Q_\beta$  values appear to occur in the upper mantle beneath the Basin and Range and the Columbia and Colorado Plateaus, although uncertainties in the data prevent a clear separation between that region and coastal regions. Low values of  $Q_\beta$  occur in the upper crust, higher values in the lower crust, and highest values in the uppermost 20 km of the mantle of all these regions. These overlie an upper mantle low-Q zone in which  $Q_\beta$  values decrease from east to west, lowest values (15-20) being similar to those observed above descending slabs in the western Pacific.

The regional pattern of upper mantle shear wave Q values is similar to that observed for upper crustal shear wave Q values inferred from surface wave studies and for Lg coda Q values. The patterns of upper crustal and upper mantle Q variations correlate with the temporal sequence of tectonic and magmatic activity in the western United States, lowest Q values in both

depth ranges occurring where tectonic activity has been most recent. Partial melting and/or enhanced dislocation motion in the mantle and variations in the volume of interstitial hydrothermal fluids in cracks in the upper crust may both be ultimately due to processes which occurred during plate consumption and interaction near the western margin of the United States.

## INTRODUCTION

Several early studies revealed that the upper mantle of the western United States is characterized by abnormally low seismic velocities (Johnson, 1967; Archambeau *et al.*, 1969; Julian, 1970). Attenuation studies using both body waves (Solomon and Toksöz, 1970; Der *et al.*, 1980; Der *et al.*, 1982) and surface waves (Lee and Solomon, 1975; Patton and Taylor, 1984; Chen, 1985; Hwang and Mitchell, 1987) have shown that the upper mantle there is also more absorptive of seismic energy than the upper mantle of more stable regions. These studies have presented strong evidence for both low-velocity and low-Q zones in the upper mantle; however, there is still considerable uncertainty about their regional and depth distributions. Moreover, we have little understanding of the physical mechanisms which produce lateral heterogeneity of the zones. It is presumably associated with the tectonic development of the region and, if so, can be correlated with surface tectonics or with heterogeneity in the crust which may be easier to observe than that at mantle depths. The main thrust of the present paper will be to determine the extent of heterogeneity of shear-wave Q ( $Q_\beta$ ) across the western United States using Rayleigh waves and to see if it relates to variations in Q obtained at crustal depths. The nature of that relationship may provide insight into the nature of evolution of the upper mantle and crust of that region.

Early studies of lateral variations in mantle velocities in the western United States utilized body waves from distant sources. Solomon and Toksöz (1970) found significant lateral variations in attenuation of long period P and S waves beneath the United States, attenuation values being high between the Rocky Mountains and the Sierra Nevada - Cascade ranges. Lower attenuation was seen at stations along the Pacific coast. Der *et al.* (1975) investigated the regional distribution of anelastic attenuation of short period



P and S waves and found that the observed regional distribution pattern shows high attenuation in the western United States, including California. In more recent work, Lay and Wallace (1988) observed whole-mantle attenuation using ScS waves. They found  $Q_{ScS} = 95 \pm 4$ , beneath the northern Basin and Range, along with very slow shear velocities. They found much lower attenuation along the Pacific Borderlands, particularly in the Pacific Northwest, where  $Q_{ScS} = 344 \pm 88$ ; shear velocities, however, were found to be comparable to those in the Basin and Range. Their results suggested that strong variations in  $Q_{ScS}$  within tectonic North America are not closely correlated with shear velocity variations.

Studies of shear wave Q ( $Q_\beta$ ) in the upper crust of the same region using surface waves have shown that the upper crust attenuates seismic energy much more severely than does the upper crust in stable regions (Mitchell, 1975; Cheng and Mitchell, 1981; Patton and Taylor, 1984). The high anelastic attenuation produced by those low Q values in the crust also produces lower than normal values of Q for regional phases such as Pg and Lg (Sutton *et al.*, 1967; Singh and Herrmann, 1983).

In this study we determine Rayleigh wave attenuation coefficients over several paths in the western United States, including the first such determinations for the western margin region, and use that information to study the lateral variation of the anelastic properties of the crust and upper mantle. Surface waves should be more sensitive to lateral changes in rock properties than body waves since body waves sample the mantle in a vertical sense and will be more sensitive to the vertical variations than to the lateral variations of rock properties. Another advantage of using surface waves in such studies is that different wavelengths sample different depths, and by inverting these measurements we can constrain the depth extent of the attenuation hetero-

geneity beneath the western United States. This cannot be done reliably using body waves since they measure attenuation along whole-mantle paths (e.g.  $Q_{scs}$ ) or average differences in attenuation along mantle-ray paths (e.g. P and S waves). In this study we emphasize upper mantle variations of  $Q_\beta$ , but show that low values of  $Q_\beta$  in the mantle and upper crust appear to be closely related to one another and both can be explained by a simple evolutionary model which is consistent with our knowledge of the tectonic development of the western United States.

### DATA ACQUISITION

We have used a two-station method to determine fundamental-mode Rayleigh-wave velocities and attenuation coefficients over several paths in the western United States (Figure 1). Nine stations belonging to the World-Wide Standard Seismograph Network (WWSSN) and one station of the Canadian Seismograph Network (CSN) provided data for this study. Since we restricted our study to Rayleigh waves only long-period vertical component data were utilized.

We searched for earthquakes which were recorded by two stations for which the great circle path between stations differed from that between the epicenter and stations by 4 degrees or less. We found 26 events which met that criterion and were well recorded at two stations (Table 1).

We divided the western United States into three regions and assumed that elastic and anelastic properties of the crust and upper mantle are relatively laterally uniform within each of the regions. The paths between any two stations were selected so that they are totally or nearly totally located within a single region. In order to minimize the effect of lateral hetero-

geneities we tried, as far as possible, to select paths which were parallel or subparallel to the strike of the tectonic features.

The path JCT-EDM covers the first region which we designate as the Eastern Rockies (ER). This region includes a small part of the Great Plains in addition to the eastern Rockies area. The second region, designated the Intermountain region (IM), is covered by 6 paths, LON-ALQ, LON-DUG, COR-DUG, DUG-TUC, TUC-LUB, and TUC-JCT. This region includes the Basin and Range province, the Colorado and Columbia plateaus. The third region, which we call the Western Margin (WM), is covered by two paths, COR-GSC and COR-BKS. This region includes the westernmost Basin and Range, the Sierra Nevada, the Cascades, and the Pacific coast ranges.

## DISPERSION AND ATTENUATION MEASUREMENTS

Analog records for all stations were digitized and processed using the multiple-filter method (Dziewonski *et al.*, 1969), after proper correction for geometrical spreading and instrument response, to provide group velocities and amplitude spectra for surface wave modes of interest. The group delay for the fundamental mode on each seismogram was used to calculate the phase which, in turn, was used to calculate an initial estimate of wave number. This estimate was then used as input to a frequency-variable filter (FVF) (Russell *et al.*, 1988) for refining the spectral amplitudes and group velocities.

This technique combines the beneficial aspects of a time-variable filter and a phase-matched filter. It is similar to the time-variable filter (Landisman *et al.*, 1969) except that the phase of the mode of interest is first removed to minimize spectral distortions due to phase fluctuations.

After frequency-variable filtering of each seismogram, we applied a frequency-domain Wiener filter (Hwang and Mitchell, 1986) to determine the interstation Green's function ( $G$ ) between the station pairs according to the relation

$$G = \frac{H}{R} \quad (1)$$

where  $H$  is the crosscorrelation function matrix between the input signal (at station 1) and output signal (at station 2), and  $R$  is the autocorrelation matrix of the input signal. Frequency-domain Wiener filtering guarantees the removal of random noise and provides more stable and accurate estimates of group and phase velocities and attenuation coefficients than other methods, e.g. the spectral ratio technique.

Knowledge of the Green's function allows us to measure interstation phase and group velocities and attenuation coefficients. Interstation phase velocities were calculated from the phase spectra of the transfer functions using the formula (Taylor and Toksöz, 1982)

$$c(f) = \frac{f\Delta x}{ft_0 + (\phi(f) \pm N)}, \quad (2)$$

where  $\Delta x$  is the interstation distance in kilometers,  $t_0$  is the first time point of the Green's function and  $\phi(f)$  is the phase of the Green's function in cycles. Following Hwang and Mitchell (1986), attenuation coefficients of the interstation medium were calculated using

$$\gamma(r) = -\ln \left| G(r) \right| \frac{\sqrt{\sin\Delta_1/\sin\Delta_2}}{\Delta x} \quad (3)$$

where  $\Delta_1$  and  $\Delta_2$  are the epicentral distances in degrees for stations 1 and 2, respectively, and  $G(f)$  is the interstation Green's function. The interstation group velocities were calculated using

$$U(f) = \frac{x_2 - x_1}{t_2 - t_1} \quad (4)$$

where  $x_1$  and  $x_2$  are epicentral distances in kilometers for stations 1 and 2, respectively, and  $t_1$  and  $t_2$  are arrival times.

Several possible sources of error will contribute to the uncertainty in the measurements of phase and group velocities and attenuation coefficients of surface waves. These have been discussed in detail by several authors (e.g., Forsyth, 1975; Kijko and Mitchell, 1983). Systematic errors may be caused by interference by other phases, incomplete separation of modes, and lateral refraction. Horizontal refraction in an inhomogeneous medium can cause multiple arrivals of energy (Capon, 1970, 1971), beating (Pilant and Knopoff, 1964), or unusual amplitude variations (McGarr, 1969) which are produced by focusing and defocusing. If multiple arrivals are out of phase and spatially separated, then phase-matched filtering (PMF) will take care of these and isolate the fundamental mode from other arrivals. If, however, these multiple arrivals are in phase, then the PMF cannot discriminate between them. If that occurs energy may be enhanced, by focusing, at one station relative to the other, sometimes resulting in negative or unrealistically high attenuation coefficient values.

Russell *et al.* (1988) showed that using the PMF and FVF will guarantee the removal of the phase of the mode of interest and will minimize spectral distortions due to phase fluctuation. Also, the amount of spectral biasing due to windowing (especially when there is significant curvature in the amplitude spectrum) is controlled by using the correct window, a curvature correction, and changing time windows appropriate for the period of interest.

Capon (1970) and Forsyth (1975) demonstrated that most late arrivals of surface-wave energy could be attributed to refraction at continental margins. We expect the same situation in the present study because many of the events used in this study are located in the Pacific Ocean near the Central

and South American coasts. Other sources of systematic errors are mislocation of the source and uncertainties in origin time. For two-station measurements, however, such errors will cancel. Random errors can be caused by errors in digitization and scattering.

## INTERSTATION VELOCITIES

### *The Eastern Rockies Region (ER)*

Five two-station events along the path JCT-EDM were used to determine interstation phase and group velocities for the ER region, spanning a period range from 13 to 92 sec. Table 2 and Figure 2a show the means and standard deviations of these five events which will be used later to invert for a velocity model of the region. The group velocities at shorter periods exhibit greater scatter than the phase velocities and the group velocities at longer periods. This may occur because velocities at shorter periods are more sensitive to the lateral variation of shallower structure than longer periods.

### *The Intermountain Region (IM)*

Thirteen events along 6 paths, COR-DUG, LON-DUG, LON-ALQ, DUG-TUC, TUC-LUB, and TUC-JCT, were used to determine interstation phase and group velocities in the IM region for the period range 16 to 80 sec (Table 3 and Figure 2b). Velocities at long periods show scatter which is just as large as that at short periods for this region. Scatter at longer periods might suggest that the lateral variations in structure extend to very great depths. Large standard deviations of the data are anticipated in this region since it is a vast area which covers more than one physiographic province. However, the uncertainties in the data do not mask the main features of the dispersion curves; they are sufficiently clear so that we can consider the velo-

city structure derived from these dispersion data to represent an average model for the entire region.

#### *The Western Margin Region (WM)*

For this region we selected paths which are parallel or subparallel to the strike of the mountain ranges in order to minimize the effect of lateral variations in the structure. Seven two-station events were used along two paths, BKS-COR and COR-GSC, to determine interstation phase and group velocities for the period range 13 to 120 sec. Table 4 and Figure 2c show the means and standard deviations for these seven events.

The largest standard deviations in the dispersion data for the three different regions occur for the IM region, whereas they are lowest for the ER region and intermediate for the WM region. This comparison reflects the complexity of the IM region, in which multipathing and scattering in surface wave propagation could be greater than that in the other two regions.

### INVERSION FOR VELOCITY STRUCTURE

The phase and group velocity values determined earlier have been used to invert for shear velocity structure. Bloch *et al.* (1969) showed that group velocities are more sensitive than phase velocities to small differences in physical parameters. Thus inverting group velocities can produce a more detailed velocity structure than inverting the phase velocities. However, it is important to acquire phase velocity information because group velocities are subject to an additional degree of nonuniqueness compared to phase velocities (Pilant and Knopoff, 1970). We have therefore simultaneously inverted the two types of velocities in order to place tighter constraints on possible models and to improve structural resolution over that obtained by inverting

either group velocities or phase velocities alone (Der and Landisman, 1972).

In the present study we have adopted a half-space as the initial model so that our final model is not biased by any assumptions made concerning the location of velocity discontinuities in the initial model. Numerical experiments show that stochastic inversion fails to give a stable solution when starting from a half-space model, but the differential inversion method works well. Thus we used the differential inversion approach for the determination of all velocity models. Details of that approach are given by Hwang and Mitchell (1987). A half-space with a shear velocity of 5.0 km/sec was used as a starting model for all inversions. Poisson's ratio was taken to be 0.25 for the crust and 0.27 for the upper mantle. To test the sensitivity of the final velocity model to initial values in the half-space, we also ran the inversion process with starting velocities of 4.5 km/sec. Velocities in the final model were within the uncertainty ranges of velocities obtained using a starting model with velocities of 5.0 km/sec.

Resolving kernels were computed for all models. For any features derived from the model to be well resolved, the width of the resolving kernels should be narrower than the thickness of that feature at the corresponding depth.

#### *The Eastern Rockies Region (ER)*

Figure 3a shows the velocity model along with its resolving kernels for the Eastern Rockies region (ER). The theoretical dispersion values predicted by the model are compared to observed values in Figure 2a. The shear velocity model suggests that there is a low-velocity zone in the upper mantle which seems to be resolvable since the width of the resolving kernel is roughly the same as the thickness of the low-velocity zone at the correspond-



ing depth. This low-velocity zone starts at a depth of 110 km where the shear velocity decreases from its maximum value of 4.72 km/sec and reaches its minimum value of 4.30 km/sec at 250 km depth. There is about a 9% decrease in shear wave velocity compared to that at 110 km depth. At greater depths, velocities are poorly resolved, since resolution decreases with increasing depth.

#### *The Intermountain Region (IM)*

Figure 3b presents the shear-velocity model along with its resolving kernels for the Intermountain region (IM). The theoretical dispersion values predicted by the model are compared to observed dispersion values in Figure 2b. The model in Figure 3b has large standard deviation bars throughout all depths because the large standard deviations in the dispersion data have been mapped into errors in the model. A low-velocity zone starting at a depth of about 50 km in the upper mantle, however, seems to be marginally resolvable since the width of the resolving kernel is similar to the thickness of the low-velocity zone at the corresponding depth. Shear velocities decrease from 4.5 km/sec to a minimum velocity of 4.0 km/sec at a depth of about 75 km and continues down to a depth of about 130 km. Because of the poor resolution at those depths, it is possible that the low-velocity zone could extend considerably deeper.

#### *The Western Margin Region (WM)*

For the Western Margin, the upper mantle is characterized by very low velocities of about 4.1 km/sec (Figure 3c). Thus, the upper mantle lid in this region may be either very thin or absent. A similar result was found by Archambeau *et al.* (1969) for P waves in the Basin-and-Range province and Grand and Helmberger (1984) for S waves through a broad region of the western United States. It is interesting that a high-velocity region which

seems marginally resolvable occurs at depths between 180 and 250 km. This might be a high-velocity lithospheric plate within the upper mantle which is the remnant of a paleosubduction zone. The presence of such a zone in the same depth range has been identified by Koizume *et al.* (1973).

The shear velocity models in Figure 3 indicate no systematic regional changes in velocity which persist at all depths, but at depths in the uppermost mantle (55-150 km) where resolution is relatively good, velocities are higher in the ER region than they are in the two other regions. The similarity in average velocities for the IM and WM regions is consistent with the results of Lay and Wallace (1988) who found that both Basin and Range and Pacific Borderland have comparable velocities and are associated with very slow paths.

### RAYLEIGH WAVE ATTENUATION

A two-station method was also used to obtain attenuation coefficients of fundamental-mode Rayleigh waves. Interstation attenuation coefficients were determined from the interstation Green's function as described earlier. These measurements were much more difficult than those for phase and group velocities, with large uncertainties which may have been produced by focussing and defocussing effects described in an earlier section. Such effects have been documented by Tanimoto (1990) for part of the region of this study. We attempted to minimize this problem by using several events and paths for the determination of attenuation coefficients and by processing the data with modern filtering techniques. Even so, some of the data were characterized by large uncertainties and negative attenuation coefficient values sometimes occurred.

Focussing of waves that have traveled different paths, but which have nearly the same path from epicenter to station, results in an increase of amplitude but may have no effect on the wave form. In addition, because of lateral refraction, the spectral amplitudes observed at two stations may not correspond to waves which left the same portion of the radiation pattern of the earthquake. If this occurs, and is not recognized, amplitude variations at the source may be erroneously attributed to the effect of anelasticity along the path between stations. For these reasons, great care must be taken in selecting data used in attenuation studies. One method of checking the quality of the data is to determine the particle motion of the waves of interest. Fundamental-mode Rayleigh waves should be retrograde elliptical and the plane of the ellipse should be along the propagation path. Plots of particle motion were made in several cases where departures from a great-circle path were suspected and data were discarded if observed motion departed greatly from that expected for pure Rayleigh waves.

#### *The Eastern Rockies Region (ER)*

Attenuation coefficient values of the fundamental Rayleigh mode for the ER region were measured for five events at periods between 25 and 93 sec. The means and standard deviations of these values are given in Table 5 and Figure 4. Attenuation values at short periods were excluded because they exhibited very large scatter. For periods where only one attenuation coefficient value is available we assigned the maximum standard deviation found for other periods when inverting for a Q model.

#### *The Intermountain Region (IM)*

Interstation attenuation coefficient values for the IM region were measured for 14 events spanning a period range of 18 to 102 sec. The means and

standard deviations of these values are given in Table 6 and Figure 4. The data have greater scatter in the period range 18 to 50 sec than at longer periods. This might be due to variations in crustal structure throughout this region since paths traverse the Basin and Range province, the Columbia Plateau, and the Colorado Plateau.

#### *The Western Margin Region (WM)*

Table 7 and Figure 4 give the means and standard deviations of the attenuation coefficient values in the WM region measured for 7 events covering a period range of 18 to 120 sec. The data display much scatter, which reflects the complexity of this region, especially at shorter periods which sample the crustal structure.

A comparison of the attenuation values in the three regions (Figure 4) shows that, without considering the error bars, there is a systematic increase in attenuation coefficient values from east to west between the Rocky Mountains and the Pacific coast. If we take the uncertainties of the estimates into account, even though there is much scatter in the data, especially at short periods, we still can detect some systematic variation at longer periods. This separation is obvious between the ER and WM regions which exhibit the highest and lowest values throughout the long-period range. Values for the IM region lie between the ER and WM values at all periods, but are distinct from them at only a few periods.

### INVERSION FOR $Q_{\beta}^{-1}$

The inverse problem for obtaining the depth dependence of  $Q$  from surface waves has been discussed by a number of authors such as Anderson *et al.* (1965), Mitchell (1975), Lee and Solomon (1975, 1978), and Hwang and

Mitchell (1987). In the present study we have used a differential inverse procedure which is similar to the one used for obtaining velocity models in this study. The velocity models were used to compute partial derivatives of phase velocity with respect to compressional and shear velocities which are needed for the inversion process.

An initial half-space  $Q_\beta$  model with  $Q_\beta = 100$  ( $Q_\beta^{-1} = 0.01$ ) was used in the inversion process for all regions. This value is based on results of a previous study in the Basin-and-Range Province (Patton and Taylor, 1984). We tried several different initial  $Q_\beta$  values, including the case of infinite  $Q_\beta$  ( $Q_\beta^{-1} = 0$ ), and we found that the starting model had only a small effect on the resulting  $Q_\beta$  models.

The inversion process was applied to fundamental-mode Rayleigh wave attenuation coefficients values chosen from Tables 5, 6 and 7 which represent the means and standard deviations of the ER, IM, and WM regions, respectively. To avoid anomalous values we excluded values on the maxima and minima of the attenuation coefficient plots and selected only the points which we considered to be representative of the attenuation coefficient mean values for each region. These points were chosen at well-separated periods so that their errors could be considered to be independent (Der *et al.*, 1970). Therefore, for the inversion of attenuation measurements we used an underdetermined system where the number of observations is less than the number of layers. All of the inversions started with the initial  $Q_\beta^{-1}$  value of 0.01 and iterated until a model was obtained that gave the best fit between the theoretical attenuation values derived from that model and the observed values.

#### *The Eastern Rockies Region (ER)*

The  $Q_\beta^{-1}$  model obtained for the ER region using an initial  $Q_\beta^{-1}$  value of

0.01 is shown in Figure 5 along with the resolving kernels plotted for selected depths. The same figure also shows the fit between the theoretical attenuation coefficient values derived from the resulting model and the observed values. The model parameters are listed in Table 8. For upper crustal depths,  $Q_\beta$  values are about 70. At greater crustal depths  $Q_\beta$  values are higher, ranging between 100 and 250. The uncertainties of the crustal values are likely to be fairly high, both because of the lack of data at periods below 20 s and because of the large scatter in the short-period data. Greater confidence can be assigned to the upper mantle where values are highest (700 - 850) in the uppermost 20 km at depths between 50 and 70 km. A low-Q zone which seems resolvable starts at a depth of 70 km where  $Q_\beta$  values start to decrease and attain minimum values ( $\approx 35$ ) at about 150 to 200 km depths. At depths greater than 200 km,  $Q_\beta$  values increase slightly but resolution becomes very poor.

The model resulting from the inversion, using  $Q_\beta^{-1} = 0$  as the starting model is plotted in Figure 6, along with its resolving kernels. The same figure also shows the fit of the observed attenuation coefficient values with the theoretical values predicted from the model. A comparison of this model with that in Figure 5 shows that the two models are nearly identical. Thus the differential inversion approach assures the initial  $Q_\beta^{-1}$  values will not bias the resulting  $Q_\beta$  model even if those values are zero.

#### *The Intermountain Region (IM)*

Figure 7 shows the resulting  $Q_\beta^{-1}$  model of IM region, along with the resolving kernels plotted for selected depths. It also shows the fit between observed attenuation coefficient values and the predicted values derived from the resulting model. The large standard deviations of the observed data are transformed into large error bars in the resulting model. The theoretical

attenuation values predicted from the model, however, match the observed values well. The model parameters are listed in Table 9. The model is characterized by low  $Q_\beta$  values ( $\approx 50$ ) at upper crustal depths and relatively high  $Q_\beta$  values ( $\approx 130$ ) at lower crustal depths. As for the ER region, the uncertainties in these values must be large. The highest  $Q_\beta$  values ( $\approx 700$ -300) again occur in the uppermost 20 km of the upper mantle at depths between 30 and 50 km. A zone of very low  $Q$  values, which seems resolvable, starts at about 50 km depth and attains minimum values ( $\approx 20$ ) at about 175-250 km depth. At greater depths,  $Q_\beta$  starts to increase slightly but resolution is very poor at those depths.

#### *The Western Margin Region (WM)*

The resulting  $Q_\beta^{-1}$  model for the WM region is characterized by very low  $Q_\beta$  values ( $\approx 30$ ) in the upper crust, and higher, but still low, values ( $\approx 90$ ) in the lower crust. Again, large uncertainties must be associated with those values. The highest  $Q_\beta$  values (about 300) occur in the uppermost 20 km of the upper mantle at 40-60 km depth. A zone of extremely low  $Q$  values, which seems resolvable, starts at about 60 km depth and attains lowest values ( $\approx 15$ ) at about 175-250 km depth. At larger depths, standard deviations become large and resolution is very poor. Table 10 lists the model parameters and Figure 8 represents the model with its resolving kernels plotted for selected depths. Figure 8 also shows the fit between the observed and the theoretical attenuation coefficient values derived from this model.

A comparison of the  $Q_\beta^{-1}$  models of the three regions, ER, IM, and WM, is presented in Figure 9 along with standard deviations. There is an increase in the  $Q_\beta^{-1}$  values at upper mantle depths from east to west;  $Q_\beta^{-1}$  values are lowest for the ER region, intermediate for the IM region and highest for the WM region. The increase in  $Q_\beta^{-1}$  values between the IM region and the WM

region at upper mantle depths is, however, within the overlap of the error bars and cannot strictly be concluded to occur. The difference between the IM region and the ER region is, however, unequivocal.

## DISCUSSION

The pattern of upper mantle values of  $Q_\beta$  obtained from Rayleigh wave attenuation coefficients in the western United States is, in a gross sense, similar to that inferred from short-period (1-Hz) body-waves. Der *et al.* (1975) and Der *et al.* (1982) found upper mantle attenuation in the southwestern United States, including the Basin-and-Range and California, to be greater than elsewhere in the United States. The small number of available stations and the wide variation in individual values, however, prevent the detection of any systematic variations between the Basin-and-Range and California. The results of those studies, therefore, while consistent with our results that upper mantle  $Q$  values decrease between the eastern Rocky Mountains (ER) and western margin (WM) region, neither support nor argue against a decrease in upper mantle  $Q$  values between the Intermountain region (IM) and western margin (WM).

Solomon and Toksöz (1970), using long-period mantle  $S$  waves, and Lay and Wallace (1988) using long-period  $ScS$  waves, found upper mantle  $Q$  values to be higher to the west of the Basin-and-Range province than within it. Lay and Wallace (1988) pointed out that their observed pattern of attenuation correlates with observed heat flow in the western United States and inferred that extensive partial melting must thus occur beneath the Basin-and-Range. The difference in the inferred pattern of upper mantle attenuation obtained using long-period body waves from those obtained using short-period body waves is not easily explained, but is probably related to the



complex structure of the region. One or both results could be biased if stations were located such that they recorded waves which traverse local anomalous features, such as a penetrating slab or a local zone of partial melting. The number of stations in California used for all studies was small: two for direct long-period body waves (Solomon and Toksöz, 1970), one (and one event) for long-period ScS (Lay and Wallace, 1988), and four for short-period body waves (Der *et al.*, 1982). Resolution of this question may be possible when sufficient data become available from a broad-band network currently being installed in southern California.

Our results from inversions of Rayleigh wave attenuation coefficient data agree better with patterns of attenuation, observed for short-period body waves, than with those observed for long-period body waves. The results of Der *et al.* (1975) and Der *et al.* (1982) show patterns of low  $Q$  associated with the upper mantle over a broad region of the southwestern United States. Our results suggest the possibility of a decrease in upper mantle  $Q$  values going from the Basin-and-Range province westward, but there is much overlap in the uncertainties of measured surface wave attenuation and in the resulting models of  $Q_\beta^{-1}$ . Consequently the same upper mantle model could satisfy the attenuation data (within data uncertainties) in both the IM and WM regions. Changes in  $Q_\beta^{-1}$  between the ER and IM regions are, however, substantial and indicate that upper mantle  $Q$  values must decrease more rapidly between the eastern Rockies (ER region) and the Basin-and-Range (IM region) than between the Basin-and-Range and the western margin (WM) regions.

Singh and Herrmann (1983) mapped  $Q$  values for 1 Hz Lg in the United States and found that  $Q_{Lg}$  decreases from about 800-850 to about 200-300 between the Rocky Mountains and Basin-and-Range and decreases further to

about 150 in coastal California. Thus, crustal values of shear wave  $Q$  which control  $L_g$   $Q$  values appear to decrease drastically between the Rocky Mountains and Basin-and-Range, but decrease much less severely between the Basin-and-Range and California. This pattern resembles the variation in upper mantle  $Q$  values inferred from our study of surface wave attenuation. Evidence for decreasing crustal  $Q_\beta$  values from east to west within the western United States were first found by Cheng and Mitchell (1981) in a study of multi-mode Rayleigh waves. Several studies using various types of seismic data therefore indicate that both upper mantle  $Q$  values and upper crustal values decrease in similar patterns from east to west in the western United States. The similarity in these pattern suggests that the anomalously low values of  $Q$  in both the crust and upper mantle, as well as the systematic decrease in values from east to west, have a single underlying cause.

A large body of literature has linked the tectonic regimes and magmatic activity in the crust and mantle of western United States to plate consumption and the interaction of the former Farallon plate and the Pacific plate with the North American plate. The Laramide structure, including the Rocky Mountains, was formed generally between about 70 and 45 m.y. B.P. during the early Cretaceous and early to middle Eocene (Coney, 1972). During the mid-Cenozoic, arc magmatism shifted toward the Pacific coast as the angle of plate descent beneath the Cordillera changed gradually from shallow to steep between 40 to 45 and 20 to 25 m.y. B.P. (Coney and Reynolds, 1977). By the beginning of Neogene time, a continuous magmatic arc extended along a line parallel to the continental margin in the western Cordillera. This Neogene arc was later disrupted by the development of the San Andreas transform (Dickinson and Snyder, 1978). Along the Pacific coast, tectonic activity in the Coast Ranges is of late Cenozoic age (Hamilton and Myers, 1966) and both

tectonic and magmatic activity are still occurring there.

This temporal pattern of tectonic and magmatic activity corresponds with the spatial pattern of  $Q$  values in the upper crust and upper mantle of the western United States. The correspondence between lowest upper mantle  $Q$  values and recent tectonic and magmatic activity suggests that those regions are sites of most extensive partial melting or the greatest degree of dislocation motion in the upper mantle. The former mechanism is favored by Shankland *et al.* (1981) as being the cause for low seismic velocities and  $Q$  values in the upper mantle, whereas the latter is favored by Geuguen and Mercier (1973) and Minster and Anderson (1980). Because different attenuation mechanisms are additive in  $Q^{-1}$  (Shankland *et al.*, 1981), it is possible that solid-state mechanisms and partial melt mechanisms act together to produce the high attenuation observed in the upper mantle of the western United States.

Mitchell (1975, 1980) suggested that  $Q_\beta$  in the upper crust is controlled by the volume of interstitial fluids contained in cracks and microcracks. Such fluids could be hydrothermal in nature, being released during periods of tectonic activity when temperatures rose to high levels or when crustal extension caused reduced pressure at crustal depths. If that is the case, we would expect a correlation between upper crustal  $Q$  and upper mantle  $Q$  as observed in this study. It is interesting that those two low- $Q$  regions are separated by a zone of high  $Q$  values. That high- $Q$  region may occur at depths where pressure or ductile flow closes the cracks which occur at shallower depths and where temperature is not yet high enough for melting or dislocation motion to occur.

At upper mantle depths,  $Q_\beta$  values were found to be extremely low, especially for the IM and WM regions (minimum  $Q_\beta \approx 15 - 20$ ). These values are comparable with other upper mantle  $Q_\beta$  values obtained behind several

island arcs in the Pacific (Barazangi and Isacks, 1971; Kanamori, 1970; Mooney, 1970). This similarity suggests that the thermal properties and temperature of the upper mantle in western North America remain about the same as they were when active subduction was occurring during the Cenozoic era.

## CONCLUSIONS

Our study of observed surface wave dispersion and attenuation in the western United States leads to the following conclusions:

1. Rayleigh wave attenuation coefficients and upper mantle  $Q_\beta^{-1}$  values increase systematically from east to west beneath the western United States between the Rocky Mountains and the Pacific coast in a pattern which correlates with the temporal sequence of tectonic episodes and magmatic activity. Highest upper mantle  $Q_\beta^{-1}$  values (lowest  $Q_\beta$ ) occur through the western margin of the United States where the occurrence of tectonic activity is most recent, whereas lowest values (highest  $Q_\beta$ ) occur in the Rocky Mountain region where the last episode of tectonic activity occurred much earlier.
2. The attenuation pattern found in this study is similar to that of short-period teleseismic body wave attenuation patterns determined by Der *et al.* (1975). This similarity suggests that the regional variation in attenuation of both short-period body waves and surface waves is due to variations in the anelasticity of the upper 200 km of the mantle.
3. The attenuation pattern is also similar to the pattern of upper crustal  $Q_\beta$  (Cheng and Mitchell, 1981) and of Lg coda  $Q$  at about 1 Hz (Singh and Herrmann, 1983) in the western United States. This suggests that the underlying cause for  $Q$  variations in the upper mantle may be the same

as that which produces lateral variations of  $Q$  in the upper crust.

4. All  $Q_\beta$  models are characterized by a low- $Q$  zone within the upper mantle starting at about 50 - 70 km depth.  $Q_\beta$  values at those depths for the Intermountain and Western Margin regions are extremely low, being similar to upper mantle  $Q_\beta$  values obtained behind several island arcs in the western Pacific.

### ACKNOWLEDGMENTS

The programs for surface wave analysis and inversion used in this study were written by David Russell, Robert Herrmann, and Hafidh Ghalib. This research was supported by the Advanced Research Projects Agency of the Department of Defense and monitored by the Geophysics Laboratory under Contract F19628-89-K-0021.

## REFERENCES

- Anderson, D.L., A. Ben-Menahem and C.B. Archambeau, Attenuation of seismic energy in the upper mantle, *J. Geophys. Res.*, 70, 1441-1448, 1965.
- Archambeau, C.B., E.A. Flinn, and D.G. Lambert, Fine structure of the upper mantle, *J. Geophys. Res.*, 74, 5825-5865, 1969.
- Barazangi, M. and B. Isacks, Lateral variation of seismic wave attenuation in the upper mantle above the inclined earthquake zone of Tonga island arc: deep anomaly in the upper mantle, *J. Geophys. Res.*, 76, 8493-8516, 1971.
- Bloch, S., A.L. Hales, and M. Landisman, Velocities in the crust and upper mantle of southern Africa from multi-mode surface wave dispersion, *Bull. Seism. Soc. Am.*, 59, 1599-1629, 1969.
- Capon, J., Analysis of Rayleigh wave multipath propagation at LASA, *Bull. Seism. Soc. Am.*, 60, 1701-1731, 1970.
- Capon, J., Comparison of Love and Rayleigh wave multipath propagation at LASA, *Bull. Seism. Soc. Am.*, 61, 1327-1344, 1971.
- Cheng, C.C. and B.J. Mitchell, Crustal Q structure in the United States from multi-mode surface waves, *Bull. Seism. Soc. Am.*, 71, 161-181, 1981.
- Coney, P.J., Cordilleran tectonics and North America plate motion, *Am. Jour. Sci.*, 272, 603-628, 1972.

Coney, P.J. and S.J. Reynolds, Cordilleran Benioff zones, *Nature*, 270, 403-406, 1977.

Der, Z.A. and M. Landisman, Theory of error, resolution, and separation of unknown variables in inverse problems, with application to the mantle and the crust in southern Africa and Scandinavia, *Geophys. J.R. Astr. Soc.*, 27, 137-178, 1972.

Der, Z.A., R.P. Masse, and M. Landisman, Effects of observational errors on the resolution of surface waves at intermediate distances, *J. Geophys. Res.*, 75, 3399-3409, 1970.

Der, Z.A., R.P. Masse, and J.P. Gurski, Regional attenuation of short period P and S waves in the United States, *Geophys. J.R. Astr. Soc.*, 40, 85-106, 1975.

Der, Z.A., E. Smart, and A. Chaplin, Short period S-wave attenuation under the United States, *Bull. Seism. Soc. Am.*, 70, 101-125, 1980.

Der, Z.A., T.W. McElfresh, and A. O'Donnell, An investigation of the regional variation and frequency dependence of anelastic attenuation in the mantle under the United States in the 0.5 - 4 Hz band, *Geophys. J.R. Astr. Soc.*, 69, 67-99, 1982.

Dickinson, W.R. and W.S. Snyder, Plate tectonics of the Laramide orogeny, in *Laramide folding associated with basement block faulting in the western United States*, edited by V. Mathews III, *Mem. Geol. Soc. Am.*, 151, 355-366, 1978.

- Dziewonski, A., S. Bloch, and M. Landisman, A technique for the analysis of transient seismic signals, *Bull. Seism. Soc. Am.*, 59, 427-444, 1969.
- Forsyth, D.A., The early structural evolution and anisotropy of the oceanic upper mantle, *Geophys. J.R. Astr. Soc.*, 43, 103-162, 1975.
- Grand, S.P. and D.V. Helmberger, Upper mantle shear structure of North America, *Geophys. J.R. Astr. Soc.*, 76, 399-438, 1984.
- Gueguen, Y. and J.M. Mercier, High attenuation and the low velocity zone, *Phys. Earth Planet. Int.*, 7, 39-46, 1973.
- Hamilton, W.B. and W.B. Myers, Cenozoic tectonics of the western United States, *Rev. Geophysics*, 4, 509-549, 1966.
- Hwang, H.J. and B.J. Mitchell, Interstation surface wave analysis by frequency domain wiener deconvolution and modal isolation, *Bull. Seism. Soc. Am.*, 76, 847-864, 1986.
- Hwang, H.J. and B.J. Mitchell, Shear velocities,  $Q_\beta$ , and the frequency dependence of  $Q_\beta$  in stable and tectonically active regions from surface wave observation, *Geophys. J.R. Astr. Soc.*, 90, 575-613, 1987.
- Johnson, L.R., Array measurements of P velocities in the upper mantle, *J. Geophys. Res.*, 72, 6309-6325, 1967.
- Julian, B.R., Regional variations in upper mantle structure beneath North America, Ph.D. dissertation, California Institute of Technology, Pasadena,



CA, 208 pp., 1970.

Kanamori, H., Mantle beneath the Japanese arc, *Phys. Earth Planet. Inter.*, 3, 475-483, 1970.

Kijko, A., and B.J. Mitchell, Multimode Rayleigh wave attenuation and  $Q_\beta$  in the crust of the Barents shelf, *J. Geophys. Res.*, 88, 3315-3328, 1983.

Koizumi, C.J., A. Ryall, and K. Priestly, Evidence for a high-velocity lithospheric plate under northern Nevada, *Bull. Seism. Soc. Am.*, 63, 2135-2144, 1973.

Landisman, M., A. Dziewonski, and Y. Sato, Recent improvements in the analysis of surface wave observations, *Geophys. J.R. Astr. Soc.*, 17, 369-403, 1969.

Lay, T., and T.C. Wallace, Multiple ScS attenuation and travel times beneath western North America, *Bull. Seism. Soc. Am.*, 78, 2041-2061, 1988.

Lee, W.B. and S.C. Solomon, Inversion schemes for surface wave attenuation and  $Q$  in the crust and the mantle, *Geophys. J.R. Astr. Soc.*, 43, 47-71, 1975.

Lee, W.B. and S.C. Solomon, Simultaneous inversion of surface wave phase velocity and attenuation: Love waves in western North America, *J. Geophys. Res.*, 83, 3389-3400, 1978.

McGarr, A., Amplitude variations of Rayleigh waves - horizontal refractions, *Bull. Seism. Soc. Am.*, 59, 1307-1334, 1969.

- Minster, J.B. and D.L. Anderson, Dislocations and nonelastic processes in the mantle, *J. Geophys. Res.*, 85, 6347-6352, 1980.
- Mitchell, B.J., Regional Rayleigh wave attenuation in North America, *J. Geophys. Res.*, 81, 4904-4916, 1975.
- Mitchell, B.J., Frequency dependence of shear wave internal friction in the continental crust of eastern North America, *J. Geophys. Res.*, 85, 5212-5218, 1980.
- Mooney, H.M., Upper mantle inhomogeneity beneath New Zealand - seismic evidence, *J. Geophys. Res.*, 75, 285-309, 1970.
- Patton, H.J. and S.R. Taylor, Q structure of the Basin and Range from surface waves, *J. Geophys. Res.*, 89, 6929-6940, 1984.
- Pilant, W.L. and L. Knopoff, Observations of multiple seismic event, *Bull. Seism. Soc. Am.*, 54, 19-39, 1964.
- Pilant, W.L. and L. Knopoff, Inversion of phase and group slowness, *J. Geophys. Res.*, 15, 2135-2136, 1970.
- Russell, D.R., R.B. Herrmann, and H.J. Hwang, Application of frequency variable filters to surface wave amplitude analysis, *Bull. Seism. Soc. Am.*, 78, 339-354, 1988.
- Shankland, T.J., R.J. O'Connell, and H.S. Waff, Geophysical constraints on partial melt in the upper mantle, *Rev. Geophys. Space Phys.*, 19, 394-406,

1981.

Singh, S. and R.B. Herrmann, Regionalization of crustal coda Q in the continental United States, *J. Geophys. Res.*, 88, 527-538, 1983.

Solomon, S.C. and N. Toksöz, Lateral variation of attenuation of P and S waves beneath the United States, *Bull. Seism. Soc. Am.*, 60, 819-838, 1970.

Sutton, G.H., W. Mitronovas, and P.W. Pomeroy, Short period seismic energy radiation patterns from underground nuclear explosions and small magnitude earthquakes, *Bull. Seism. Soc. Am.*, 57, 249-267, 1967.

Tanimoto, T., Modelling curved surface wave paths: membrane surface wave synthetics, *Geophys. J. Int.*, 102, 89-100, 1990.

Taylor, S. and N. Toksöz, Measurement of interstation phase and group velocities and Q using Wiener filtering, *Bull. Seism. Soc. Am.*, 72, 73-91, 1982.

Department of Earth and Atmospheric Sciences  
Saint Louis University  
3507 Laclede  
St. Louis, MO 63103

TABLE 1. Earthquakes Used in This Study

Date	Origin Time UT	Latitude, deg	Longitude, deg	Depth, km	Ms	Path
April 20, 1964	1156:41.6	61.4	-147.3	30	5.7	COR-GSC
July 11, 1964	2025:40.3	59.7	-146.2	40	5.6	COR-GSC
March 28, 1965	1322:57.6	55.1	162.1	33	5.9	LON-DUG
April 16, 1965	2322:18.6	64.7	-160.1	5	5.8	COR-GSC
June 20, 1965	1916:20.9	25.4	-109.4	33	5.8	TUC-DUG
Dec. 23, 1965	2047:35.5	60.6	-140.7	11	5.8	COR-GSC
Aug. 18, 1966	1033:17.7	14.6	-91.7	85	5.6	ALQ-LON
Nov. 3, 1966	1624:32.7	19.2	-68.0	33	5.6	JCT-TUC
Nov. 4, 1967	1626:48.2	-2.8	-77.7	99	6.0	ALQ-LON
Dec. 29, 1969	051:47.2	16.2	-59.7	17	5.6	JCT-TUC
Nov. 18 1970	2010:58.2	-28.7	-112.7	33	5.6	BKS-COR
April 18 1971	1741:27.9	-0.2	-91.4	33	5.7	JCT-EDM
Aug. 20, 1971	2136:9.6	13.4	-92.4	33	5.8	JCT-EDM
Aug. 2, 1972	2138:50.4	56.1	163.2	33	5.6	LON-DUG
Aug. 12 1972	1315:48.1	5.0	-82.6	33	5.7	LON-DUG
Oct. 20, 1972	433:48.9	20.6	-29.7	33	5.7	LUB-TUC
June 22, 1974	812:47.5	-22.1	-113.6	33	5.9	BKS-COR
June 27, 1974	149:8.1	33.8	139.2	16	5.7	DUG-COR
Oct. 2 1974	254:59.7	-5.9	-81.1	5	5.7	LON-DUG
Feb. 26, 1975	448:54.7	85.0	98.0	33	5.4	BKS-COR
Aug. 19, 1975	1457:12.3	16.2	-94.1	85	5.8	JCT-EDM
Nov. 21, 1975	115:0.8	7.5	-77.6	36	5.8	DUG-COR
May 23, 1976	1632:33.0	-10.5	-78.3	73	5.9	LON-DUG
April 4, 1978	2111:41.8	10.0	-78.0	35	5.8	DUG-COR
June 4, 1979	626:42.7	15.7	-93.6	80	5.7	JCT-EDM
July 21, 1979	1212:14.0	14.0	-93.4	26	5.7	JCT-EDM

**TABLE 2. Means and Standard Deviations  
of Fundamental Mode Rayleigh Wave  
Velocities in the Eastern  
Rockies Region**

Period, s	Group Velocity, km/s	Standard Deviation, km/s	Phase Velocity, km/s	Standard Deviation, km/s
13.0	2.70	0.56	3.12	0.08
14.0	2.73	0.20	3.17	0.04
15.0	2.71	0.17	3.20	0.03
16.0	2.80	0.31	3.25	0.01
17.0	2.71	0.28	3.27	0.03
18.0	2.72	0.27	3.31	0.05
19.0	2.71	0.21	3.36	0.07
20.0	2.67	0.16	3.41	0.08
21.0	2.58	0.24	3.46	0.08
22.0	2.67	0.19	3.51	0.08
23.0	2.88	0.32	3.56	0.08
24.0	2.96	0.29	3.59	0.08
25.0	2.98	0.18	3.63	0.08
26.0	3.03	0.17	3.66	0.08
27.0	3.09	0.17	3.68	0.07
28.0	3.15	0.17	3.71	0.07
29.0	3.19	0.16	3.73	0.07
30.0	3.22	0.15	3.76	0.08
32.0	3.27	0.13	3.80	0.08
34.0	3.34	0.07	3.83	0.08
36.0	4.42	0.02	3.86	0.09
38.0	3.48	0.04	3.89	0.09
40.0	3.54	0.04	3.91	0.10
43.0	3.61	0.04	3.94	0.10
46.0	3.69	0.05	3.96	0.11
48.0	3.74	0.05	3.97	0.12
51.0	3.83	0.04	3.98	0.13
53.0	3.89	0.04	3.99	0.13
56.0	3.98	0.05	3.99	0.14
59.0	4.07	0.08	3.99	0.16
61.0	4.05	0.06	4.07	0.03
64.0	4.06	0.05	4.07	0.04
68.0	4.06	0.01	4.07	0.04
72.0	4.07	0.01	4.09	0.04
76.0	4.08	0.02	4.08	0.04
80.0	4.08	0.02	4.08	0.05
84.0	4.07	0.03	4.08	0.05
88.0	4.06	0.04	4.08	0.06
92.0	4.05	0.05	4.08	0.07

**TABLE 3. Means and Standard Deviations of  
Fundamental Mode Rayleigh Wave Velocities  
in the Intermountain Region**

Period, s	Group Velocity, km/s	Standard Deviation, km/s	Phase Velocity, km/s	Standard Deviation, km/s
16.0	3.05	0.04	3.30	0.10
17.0	2.97	0.42	3.28	0.24
18.0	3.03	0.38	3.32	0.21
20.0	3.14	0.54	3.44	0.20
21.0	3.09	0.41	3.47	0.20
22.0	3.08	0.38	3.49	0.21
23.0	3.08	0.35	3.52	0.21
24.0	3.12	0.35	3.54	0.25
25.0	3.17	0.35	3.57	0.24
26.0	3.19	0.36	3.60	0.25
27.0	3.22	0.37	3.62	0.25
28.0	3.29	0.36	3.64	0.26
29.0	3.37	0.37	3.66	0.27
30.0	3.44	0.40	3.67	0.28
32.0	3.54	0.45	3.70	0.28
34.0	3.59	0.46	3.72	0.28
36.0	3.61	0.41	3.74	0.29
38.0	3.56	0.36	3.76	0.30
40.0	3.60	0.38	3.78	0.31
43.0	3.64	0.38	3.82	0.34
46.0	3.62	0.37	3.87	0.39
48.0	3.63	0.36	3.90	0.41
51.0	3.65	0.36	3.94	0.44
53.0	3.67	0.38	3.97	0.47
56.0	3.69	0.41	4.01	0.52
59.0	3.69	0.46	4.09	0.60
61.0	3.70	0.52	4.14	0.69
64.0	3.60	0.48	4.28	0.80
68.0	3.73	0.40	4.07	0.54
72.0	3.73	0.42	4.11	0.59
76.0	3.76	0.50	4.20	0.72
80.0	3.77	0.53	4.25	0.77

**TABLE 4. Means and Standard Deviations  
of Fundamental Mode Rayleigh Wave  
Velocities in the Western  
Margin Region**

Period, s	Group Velocity, km/s	Standard Deviation, km/s	Phase Velocity, km/s	Standard Deviation, km/s
13.0	2.62	0.04	3.25	0.03
14.0	2.87	0.29	3.31	0.05
15.0	3.01	0.43	3.37	0.10
16.0	2.91	0.35	3.38	0.10
17.0	2.95	0.22	3.41	0.12
18.0	2.95	0.22	3.45	0.14
19.0	3.06	0.25	3.49	0.14
20.0	3.12	0.24	3.51	0.14
21.0	3.08	0.21	3.54	0.15
22.0	3.18	0.33	3.56	0.16
23.0	3.30	0.40	3.58	0.17
24.0	3.33	0.35	3.59	0.18
25.0	3.34	0.30	3.60	0.20
26.0	3.34	0.23	3.61	0.21
27.0	3.32	0.18	3.63	0.22
28.0	3.29	0.16	3.64	0.23
29.0	3.27	0.19	3.65	0.24
30.0	3.27	0.21	3.67	0.24
32.0	3.29	0.23	3.72	0.22
34.0	3.31	0.24	3.75	0.21
36.0	3.30	0.22	3.79	0.21
38.0	3.39	0.19	3.82	0.21
40.0	3.41	0.17	3.85	0.22
43.0	3.48	0.15	3.80	0.12
46.0	3.53	0.13	3.83	0.12
48.0	3.55	0.12	3.80	0.08
51.0	3.60	0.13	3.82	0.08
53.0	3.58	0.13	3.83	0.09
56.0	3.59	0.13	3.84	0.09
59.0	3.60	0.13	3.86	0.09
61.0	3.60	0.14	3.86	0.09
64.0	3.61	0.14	3.88	0.09
68.0	3.62	0.15	3.90	0.09
72.0	3.65	0.15	3.91	0.09
76.0	3.69	0.15	3.93	0.09
80.0	3.73	0.15	3.94	0.09
84.0	3.79	0.15	3.95	0.09
88.0	3.84	0.15	3.96	0.10
92.0	3.90	0.15	3.96	0.10
96.0	3.97	0.16	3.96	0.11
100.0	4.03	0.16	3.96	0.12
105.0	4.09	0.09	4.05	0.08
110.0	4.14	0.09	4.05	0.09

TABLE 5. Means and Standard  
Deviations of Attenuation  
Coefficients in the  
Eastern Rockies  
Region

Period, s	$\gamma \times 10^{-4}$ , $\text{km}^{-1}$	Standard Deviation $\times 10^{-4}$ , $\text{km}^{-1}$
25.3	4.35	1.75
25.9	4.40	1.75
26.6	4.19	1.75
27.3	3.85	1.75
28.1	3.47	1.75
28.8	3.10	1.75
29.3	2.10	0.72
29.7	2.77	1.75
30.1	2.14	0.42
30.6	2.48	1.75
31.0	2.17	0.29
31.5	2.26	1.75
32.0	1.71	1.05
33.0	1.81	0.96
34.1	1.92	0.85
35.3	1.62	1.10
36.6	1.71	1.03
37.9	1.76	0.96
39.4	1.77	0.88
41.0	1.72	0.83
42.7	1.64	0.88
44.5	2.01	0.55
45.5	2.11	1.75
46.5	2.11	0.54
47.6	2.12	1.75
48.8	2.19	0.66
50.0	2.17	1.75
51.2	2.17	0.70
53.9	2.06	0.63
56.9	1.71	0.81
60.2	1.78	0.86
64.0	2.05	0.64
66.1	2.35	1.75
68.3	1.81	0.61
70.6	2.11	1.75
73.1	1.87	0.19
75.9	1.78	1.75
78.8	1.65	0.10
81.9	1.27	1.75
85.3	1.30	0.46
89.0	0.55	1.75
93.1	0.22	0.04



**TABLE 6. Means and Standard Deviations of Attenuation  
Coefficients in the Intermountain Region**

Period s	$\gamma$ $\times 10^{-4}$ $\text{km}^{-1}$	Standard Deviation $\times 10^{-4}$ $\text{km}^{-1}$	Period s	$\gamma$ $\times 10^{-4}$ $\text{km}^{-1}$	Standard Deviation $\times 10^{-4}$ $\text{km}^{-1}$
18.1	10.49	5.11	33.0	4.52	2.79
18.3	10.13	4.86	33.6	4.32	2.99
18.4	9.68	4.50	34.1	3.85	2.79
18.6	9.11	4.10	34.7	3.89	2.77
18.7	8.42	3.69	35.3	3.69	2.33
19.0	7.61	3.30	35.9	3.67	2.14
19.1	6.68	3.05	36.6	3.37	1.78
19.3	5.63	3.09	37.2	3.32	1.81
19.5	5.58	2.95	38.6	3.23	2.34
19.7	5.52	3.35	39.4	3.26	2.45
19.9	5.07	3.33	40.2	3.75	2.86
20.3	4.21	3.63	41.0	3.65	3.01
20.5	4.59	2.26	41.8	3.88	3.45
20.9	4.96	2.89	42.7	3.66	3.50
21.3	4.86	3.29	43.6	4.19	3.90
21.8	4.44	3.22	44.5	3.79	3.64
22.0	4.83	3.41	45.5	3.79	3.70
22.3	3.84	2.92	46.5	3.78	3.28
22.5	3.94	3.20	47.6	3.39	3.08
22.8	3.16	2.62	48.8	3.37	2.67
23.0	3.00	3.06	49.9	3.31	2.52
23.3	2.82	2.94	51.2	3.21	1.96
23.5	2.93	3.90	52.5	2.87	1.72
24.1	2.58	3.48	53.9	3.02	1.43
24.7	2.31	3.06	55.4	2.59	1.13
25.3	2.15	2.67	56.9	2.63	1.22
26.3	2.95	2.98	58.5	2.59	1.47
26.6	3.38	3.46	60.2	2.09	1.09
27.0	3.36	2.96	62.1	1.91	1.22
27.3	3.83	3.45	64.0	2.23	1.19
27.7	3.77	3.02	66.1	2.40	1.17
28.1	4.28	3.53	68.3	2.90	1.18
28.4	4.17	3.16	70.6	3.19	1.36
28.8	4.74	3.36	73.1	3.28	1.76
29.3	4.56	3.12	75.9	3.11	2.19
29.7	4.52	3.47	78.8	3.74	2.58
30.1	4.47	3.14	81.9	3.31	2.23
30.6	4.82	3.30	85.3	2.38	1.41
31.0	4.69	2.98	89.0	2.87	0.01
31.5	4.68	3.04	93.1	3.16	1.31
32.0	4.53	2.83	97.5	3.45	1.81
32.5	4.73	2.97	102.4	3.61	1.55

TABLE 7. Means and Standard Deviations of Attenuation  
Coefficients in the Western Margin Region

Period s	$\gamma$ $\times 10^{-4}$ $\text{km}^{-1}$	Standard Deviation $\times 10^{-4}$ $\text{km}^{-1}$	Period s	$\gamma$ $\times 10^{-4}$ $\text{km}^{-1}$	Standard Deviation $\times 10^{-4}$ $\text{km}^{-1}$
18.3	12.21	5.51	30.6	4.49	3.54
18.5	10.60	7.13	34.1	5.04	3.98
18.6	11.00	7.33	34.7	5.02	3.99
18.8	11.36	7.52	35.3	4.99	3.99
19.0	11.60	7.65	35.9	4.96	3.99
19.1	11.67	7.69	36.6	4.92	3.98
19.3	11.56	7.62	37.2	4.89	3.96
19.5	11.34	7.50	37.9	4.87	3.92
19.7	9.50	7.84	38.6	4.86	3.85
19.9	9.28	7.51	39.4	4.85	3.74
20.1	9.02	7.15	40.2	4.17	3.49
20.3	8.73	6.79	41.0	3.51	3.21
20.5	8.42	6.44	41.8	3.65	3.00
20.7	8.09	6.12	42.7	3.76	2.82
20.9	7.74	5.84	43.6	3.86	2.68
21.1	7.40	5.61	44.5	3.94	2.60
21.3	7.05	5.43	45.5	3.99	2.57
21.6	6.71	5.28	46.5	4.04	2.61
21.8	6.38	5.15	47.6	3.46	2.71
22.0	6.06	5.03	48.8	4.49	2.12
22.3	5.75	4.88	50.0	4.73	1.93
22.5	6.40	4.38	51.2	4.99	1.76
22.8	6.10	4.14	52.5	5.10	1.98
23.0	5.80	3.89	53.9	5.46	1.97
23.3	5.49	3.64	55.4	5.71	1.99
23.5	5.18	3.38	56.9	5.81	2.03
23.8	4.86	3.14	58.5	5.74	2.08
24.1	4.54	2.91	60.2	5.49	2.09
24.4	4.24	2.73	62.1	5.09	1.99
24.7	3.95	2.58	64.0	4.58	1.73
25.0	4.28	2.26	66.1	4.05	1.29
25.3	4.08	2.12	68.3	3.61	0.69
25.6	3.89	2.06	70.6	3.33	0.11
25.9	3.70	2.09	73.1	3.28	0.55
26.3	4.17	1.91	75.9	3.49	0.94
26.6	4.02	2.12	78.8	3.91	1.22
26.9	3.86	2.45	81.9	4.39	1.53
27.3	3.50	3.13	85.3	4.80	1.97
27.7	3.62	3.17	89.0	4.59	2.30
28.1	3.74	3.23	93.1	5.07	2.67
28.4	3.86	3.29	97.5	5.47	3.15
28.8	3.98	3.35	102.4	5.73	3.57
29.3	4.10	3.41	107.8	4.75	6.06
29.7	4.22	3.45	113.8	4.56	5.67
30.1	4.35	3.94	120.5	3.79	4.23

**TABLE 8.  $Q_{\beta}^{-1}$  Model of the  
Eastern Rockies Region**

Depth km	Thickness km	$Q_{\beta}$	$Q_{\beta}^{-1}$ $\times 10^{-3}$	Standard Deviation $\times 10^{-3}$
5.0	10.0	65	15.3	3.0
15.0	10.0	65	15.3	2.9
25.0	10.0	74	13.4	2.6
35.0	10.0	109	9.1	1.9
45.0	10.0	226	4.4	1.3
55.0	10.0	722	1.4	1.6
65.0	10.0	834	1.2	2.3
75.0	10.0	252	4.0	2.7
85.0	10.0	111	9.0	2.8
100.0	20.0	65	15.3	2.6
120.0	20.0	46	21.7	2.1
140.0	20.0	38	26.4	1.8
162.5	25.0	35	28.9	2.1
187.5	25.0	34	29.1	2.5
212.5	25.0	36	27.6	2.6
237.5	25.0	40	24.9	2.5
262.5	25.0	46	21.6	2.2
287.5	25.0	56	17.9	1.6
312.5	0.0	71	14.1	1.0

TABLE 9.  $Q_{\beta}^{-1}$  Model of the  
Intermountain Region

Depth km	Thickness km	$Q_{\beta}$	$Q_{\beta}^{-1}$ $\times 10^{-3}$	Standard Deviation $\times 10^{-3}$
5.0	10.0	45	22.3	8.2
15.0	10.0	57	17.7	6.5
25.0	10.0	133	7.5	3.7
35.0	10.0	469	2.1	6.6
45.0	10.0	334	3.0	9.8
55.0	10.0	128	7.8	11.4
65.0	10.0	71	14.1	11.4
75.0	10.0	50	20.1	10.7
85.0	10.0	39	25.7	10.0
100.0	20.0	32	31.0	10.2
120.0	20.0	27	37.0	11.0
140.0	20.0	23	43.6	12.5
162.5	25.0	20	49.8	14.2
187.5	25.0	19	54.1	15.1
212.5	25.0	18	55.0	14.9
237.5	25.0	19	52.3	13.6
262.5	25.0	22	46.2	11.4
287.5	25.0	27	37.4	8.4
312.5	0.0	38	26.4	4.9

TABLE 10.  $Q_{\beta}^{-1}$  Model of the Western  
Margin Region

Depth km	Thickness km	$Q_{\beta}$	$Q_{\beta}^{-1}$ $\times 10^{-3}$	Standard Deviation $\times 10^{-3}$
5.0	10.0	28	35.7	19.6
15.0	10.0	29	34.2	18.2
25.0	10.0	40	25.1	12.5
35.0	10.0	86	11.6	9.0
45.0	10.0	314	3.2	14.4
55.0	10.0	297	3.4	18.2
65.0	10.0	99	10.1	18.7
75.0	10.0	50	20.1	17.4
85.0	10.0	32	31.2	16.0
100.0	20.0	24	42.4	15.5
120.0	20.0	19	52.4	14.6
140.0	20.0	16	61.3	15.4
162.5	25.0	14	68.8	18.6
187.5	25.0	14	73.9	21.8
212.5	25.0	13	75.8	23.7
237.5	25.0	14	73.7	23.7
262.5	25.0	15	67.6	21.7
287.5	25.0	17	57.5	17.9
312.5	0.0	23	43.7	12.8

## List of Figure Captions

Fig. 1. Map showing two-station paths in the area of study. Triangles denote the seismograph stations.

Fig. 2. Interstation fundamental mode Rayleigh phase and group velocity values (squares) for the three regions: (a) the Eastern Rockies, (b) the Intermountain region, and (c) the Western Margin. Vertical bars represent standard deviation. The solid curves are theoretical dispersion curves predicted by the models shown in Figure 3.

Fig. 3. Shear velocity model (left) obtained by inverting group and phase velocities of the fundamental Rayleigh mode for the three regions: (a) the Eastern Rockies, (b) the Intermountain region, and (c) the Western Margin. Dashed lines indicate the initial half-space model. Resolving kernels, each normalized to unity, corresponding to several depths are also plotted.

Fig. 4. Comparison of attenuation coefficients of the fundamental Rayleigh mode for the three regions: Western Margin region (circles), Intermountain region (crosses), and Eastern Rockies region (squares). Vertical and diagonal lines denote standard deviation values.

Fig. 5.  $Q_\beta^{-1}$  model (top left) obtained by inverting fundamental Rayleigh mode attenuation coefficients in the Eastern Rockies region. Initial  $Q_\beta^{-1} = 0.01$  (dashed line). Normalized resolving kernels at several depths are also shown. Theoretical attenuation coefficients (solid line) predicted by the  $Q_\beta^{-1}$  model are compared to observed values (squares) in the lower diagram. Vertical bars represent standard deviations.

Fig. 6.  $Q_\beta^{-1}$  model (top left) obtained by inverting fundamental Rayleigh mode attenuation coefficients in the Eastern Rockies region. Initial  $Q_\beta^{-1} = 0.0$ . Normalized resolving kernels (top right) at several depths are also shown. Theoretical attenuation coefficients (solid line) predicted by the  $Q_\beta^{-1}$  model are compared to observed values (squares) in the lower diagram. Vertical bars represent standard

deviations.

Fig. 7.  $Q_\beta^{-1}$  model (top left) obtained by inverting fundamental Rayleigh mode attenuation coefficients in the Intermountain region. Initial  $Q_\beta^{-1} = 0.01$  (dashed line). Normalized resolving kernels (top right) at several depths are also shown. Theoretical attenuation coefficients (solid line) predicted by the  $Q_\beta^{-1}$  model are compared to observed values (squares) in the lower diagram. Vertical bars represent standard deviations.

Fig. 8.  $Q_\beta^{-1}$  model (top left) obtained by inverting fundamental Rayleigh mode attenuation coefficients in the Western Margin region. Initial  $Q_\beta^{-1} = 0.01$  (dashed line). Normalized resolving kernels (top right) at several depths are also shown. Theoretical attenuation coefficients (solid line) predicted by the  $Q_\beta^{-1}$  model are compared to observed values (squares) in the lower diagram. Vertical bars represent standard deviations.

Fig. 9. Comparison of  $Q_\beta^{-1}$  models of Eastern Rockies (long-dashed line), Intermountain (short-dashed line), and Western Margin (solid line). Horizontal bars denote one standard deviation.

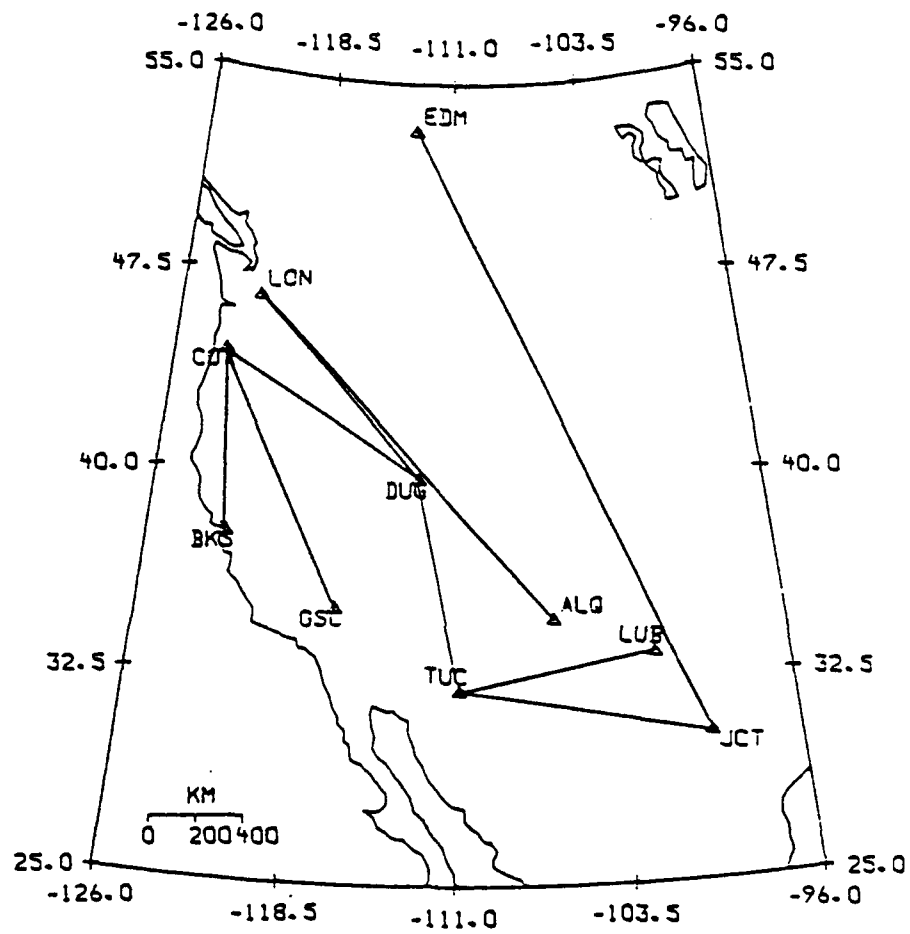


Figure 1



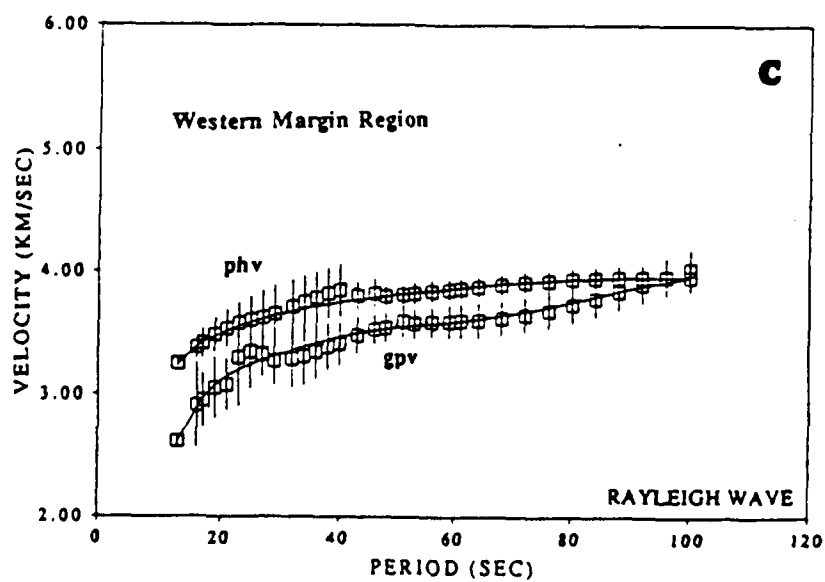
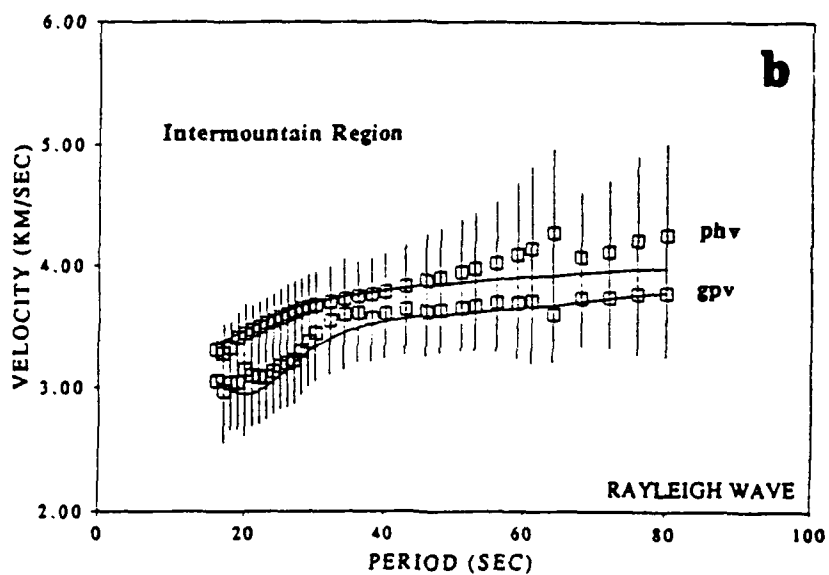
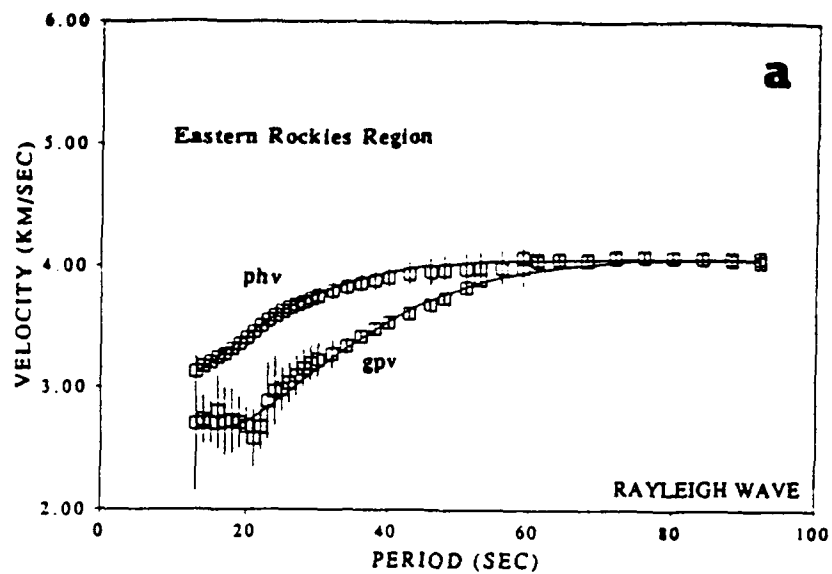


Figure 2  
69

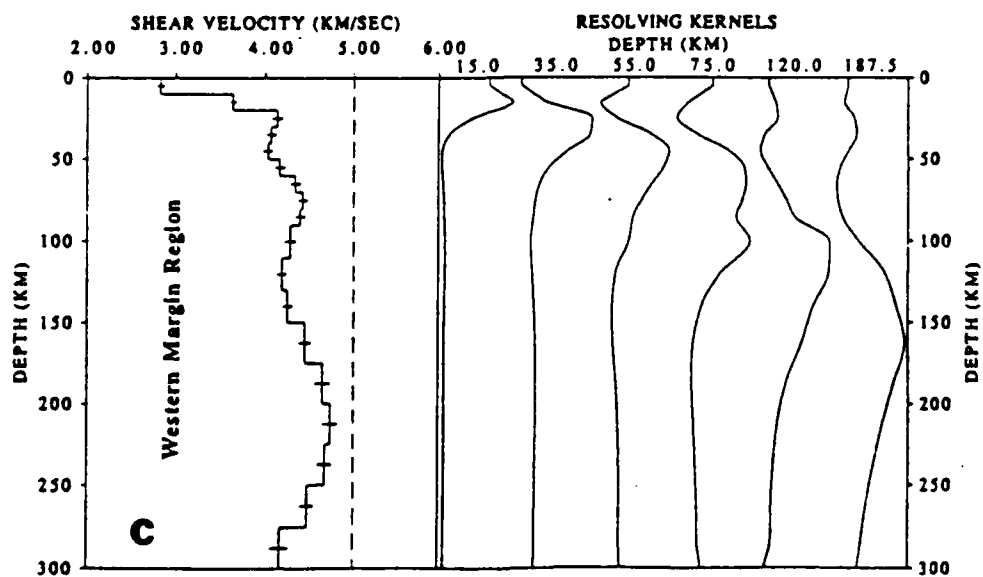
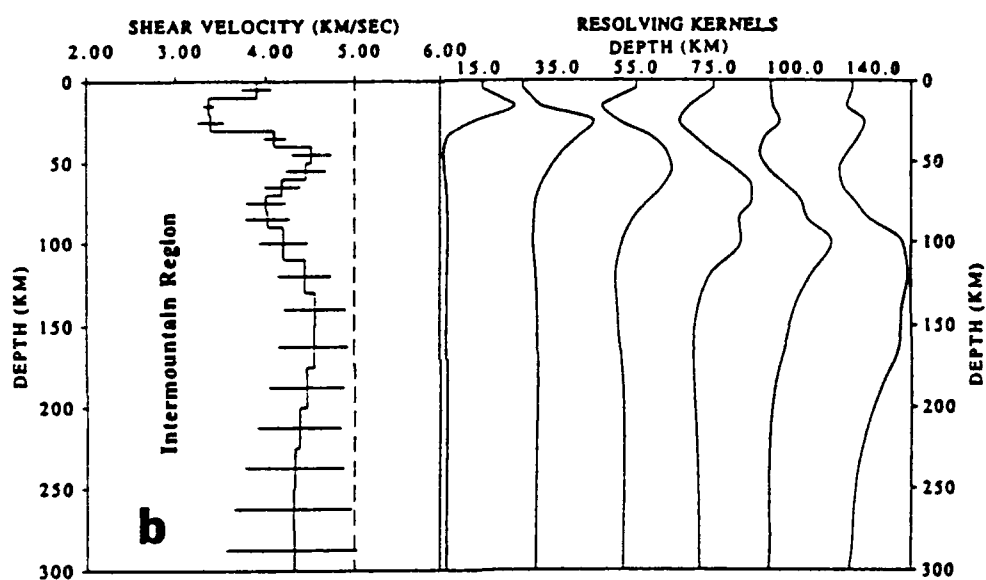
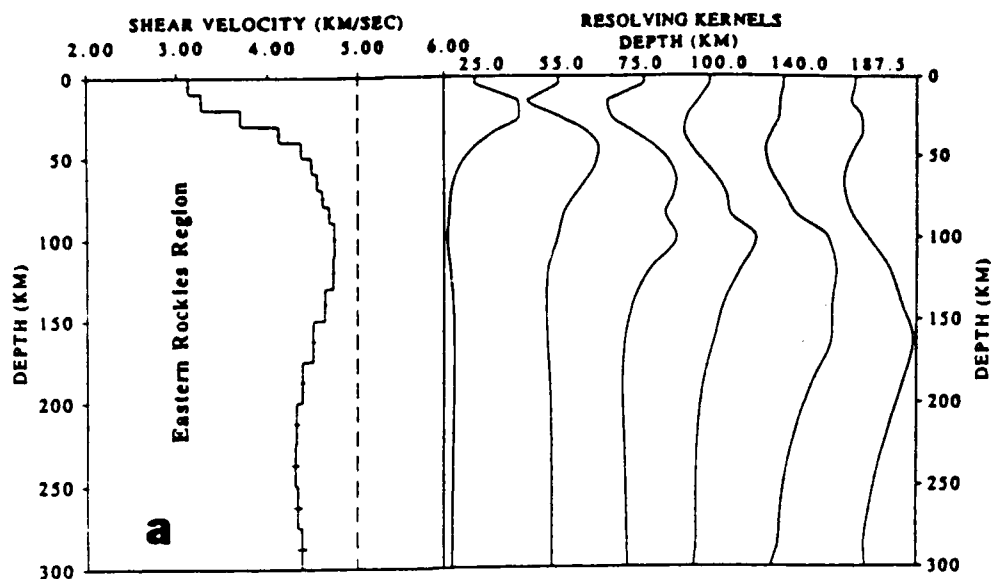


Figure 3  
70

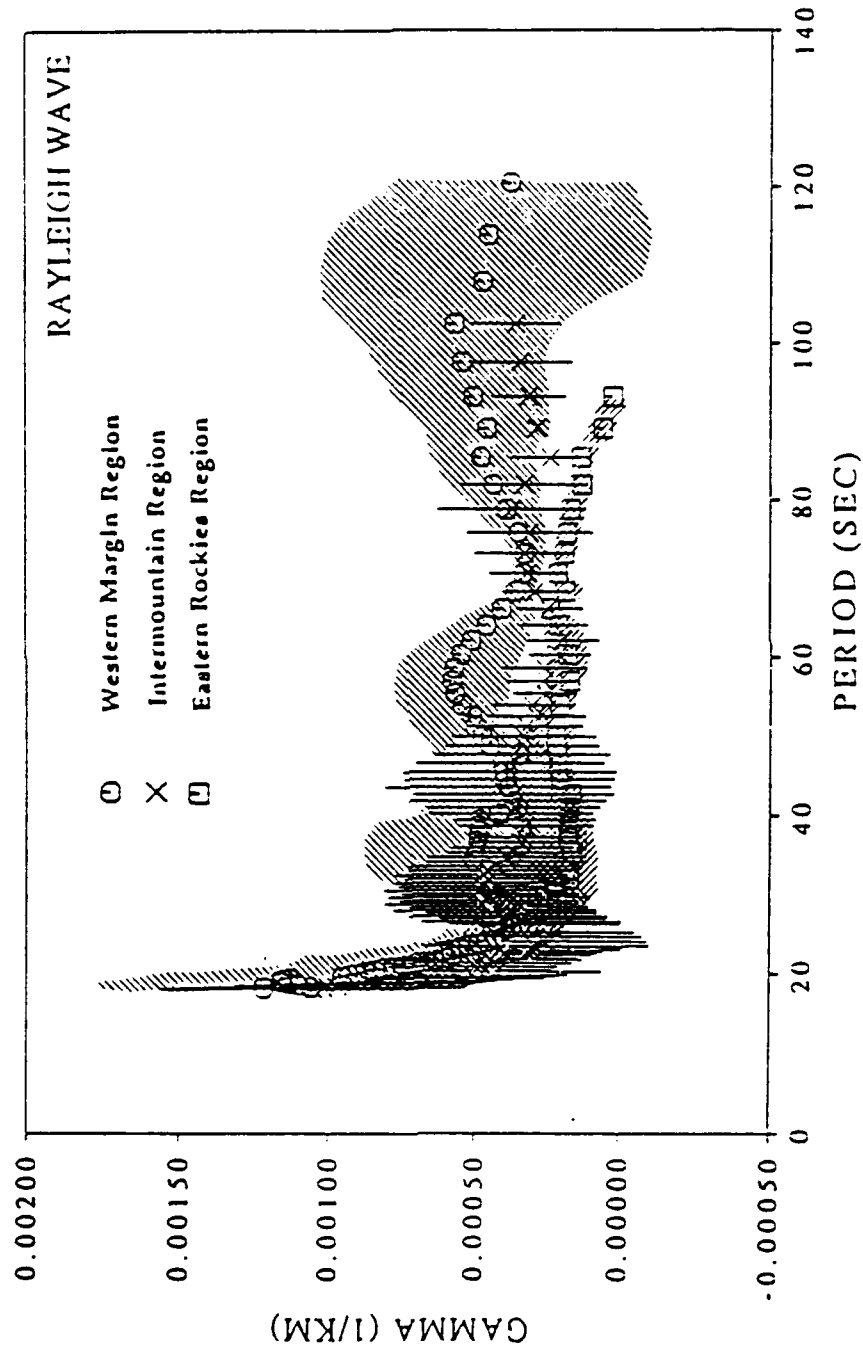


Figure 4

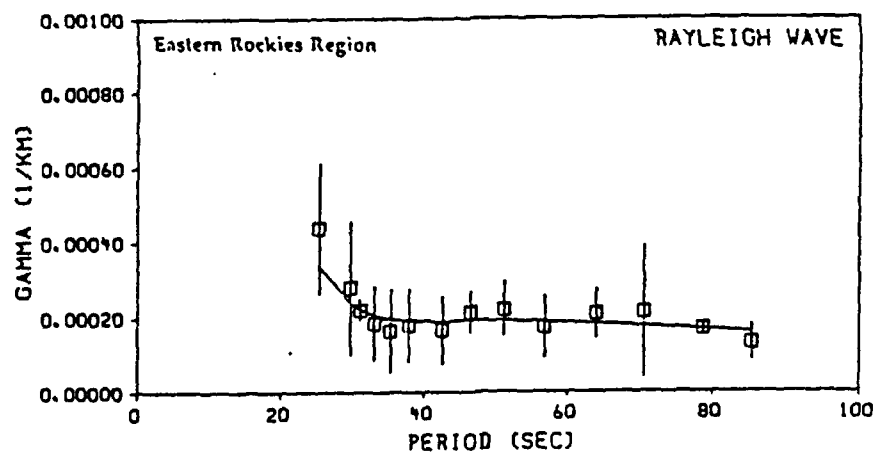
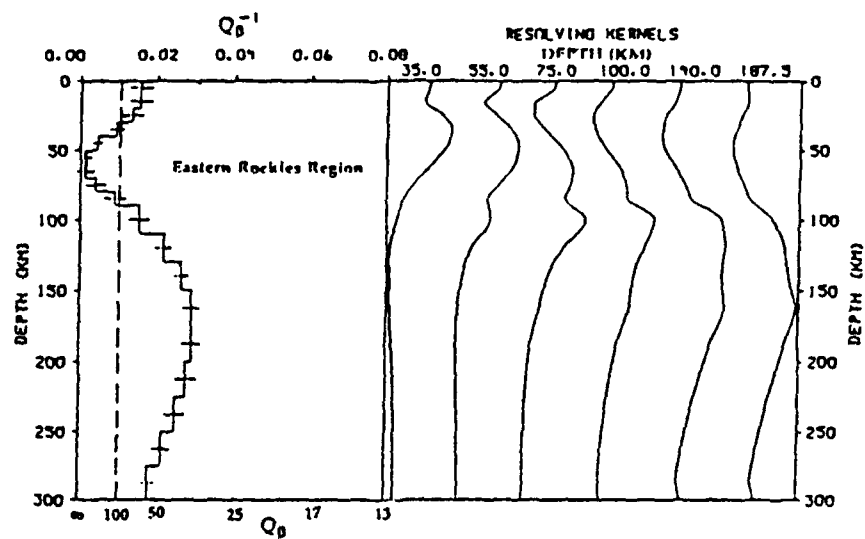


Figure 5

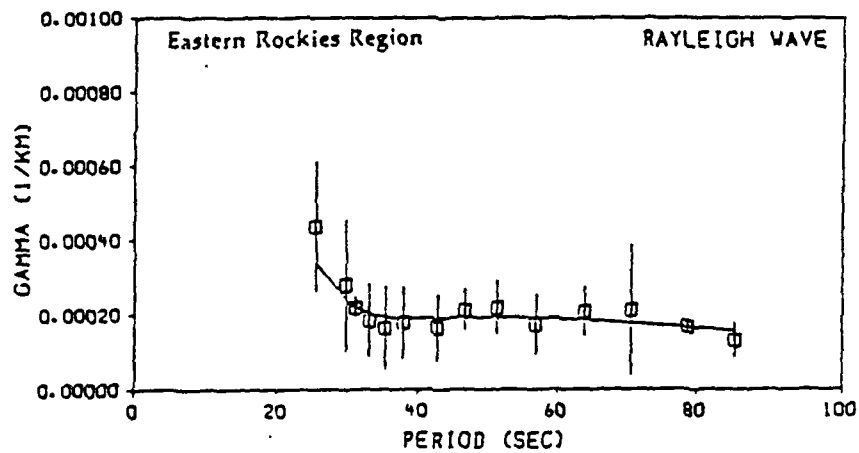
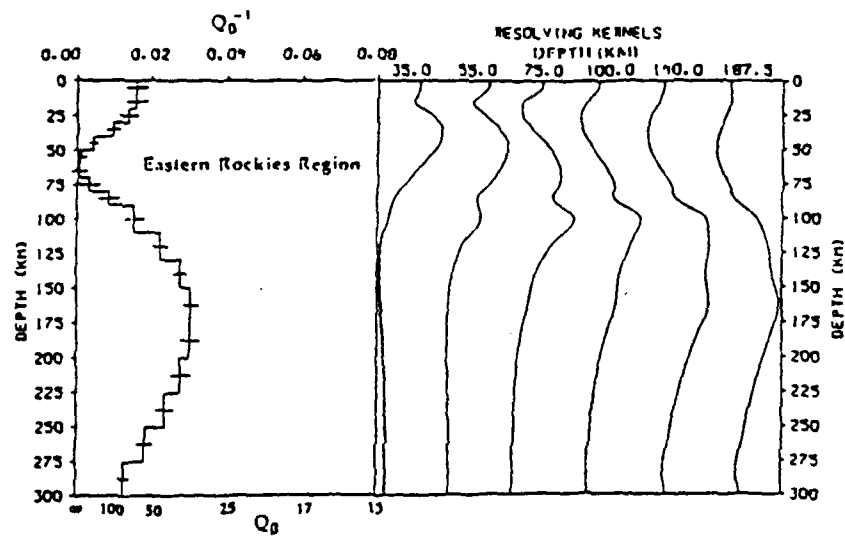


Figure 6

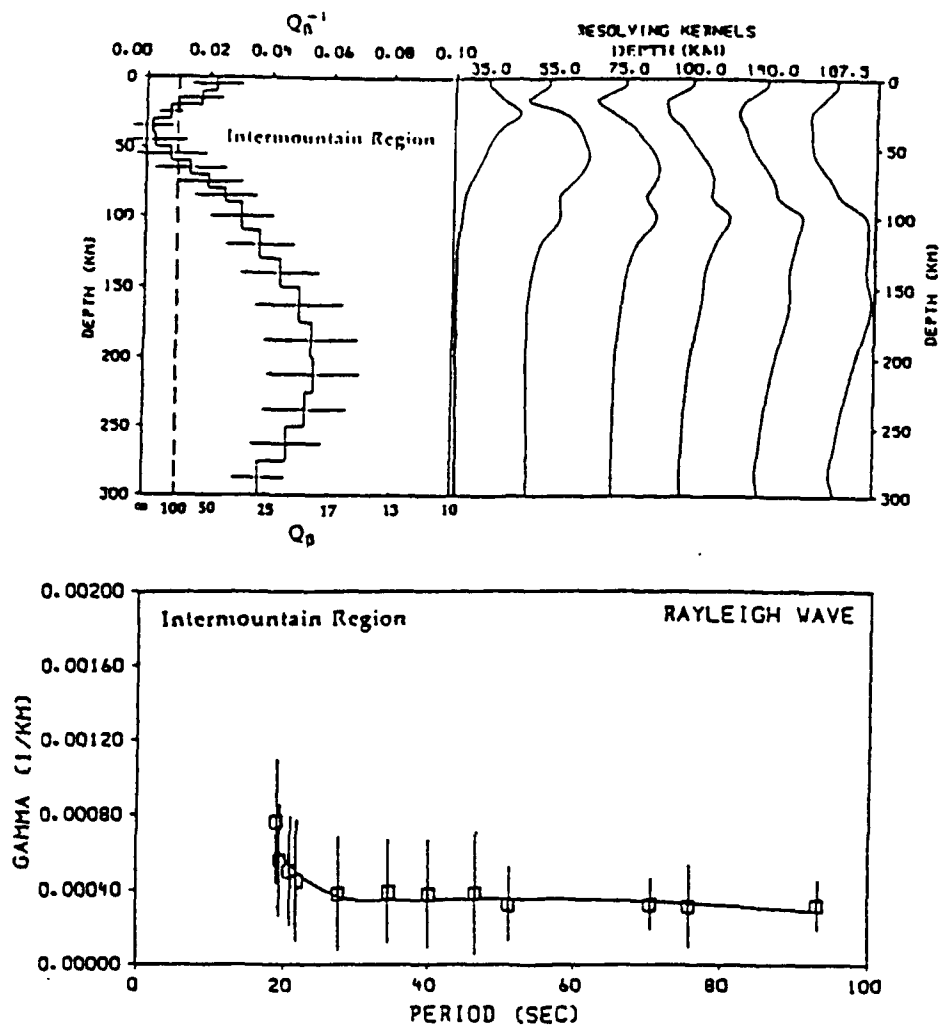


Figure 7

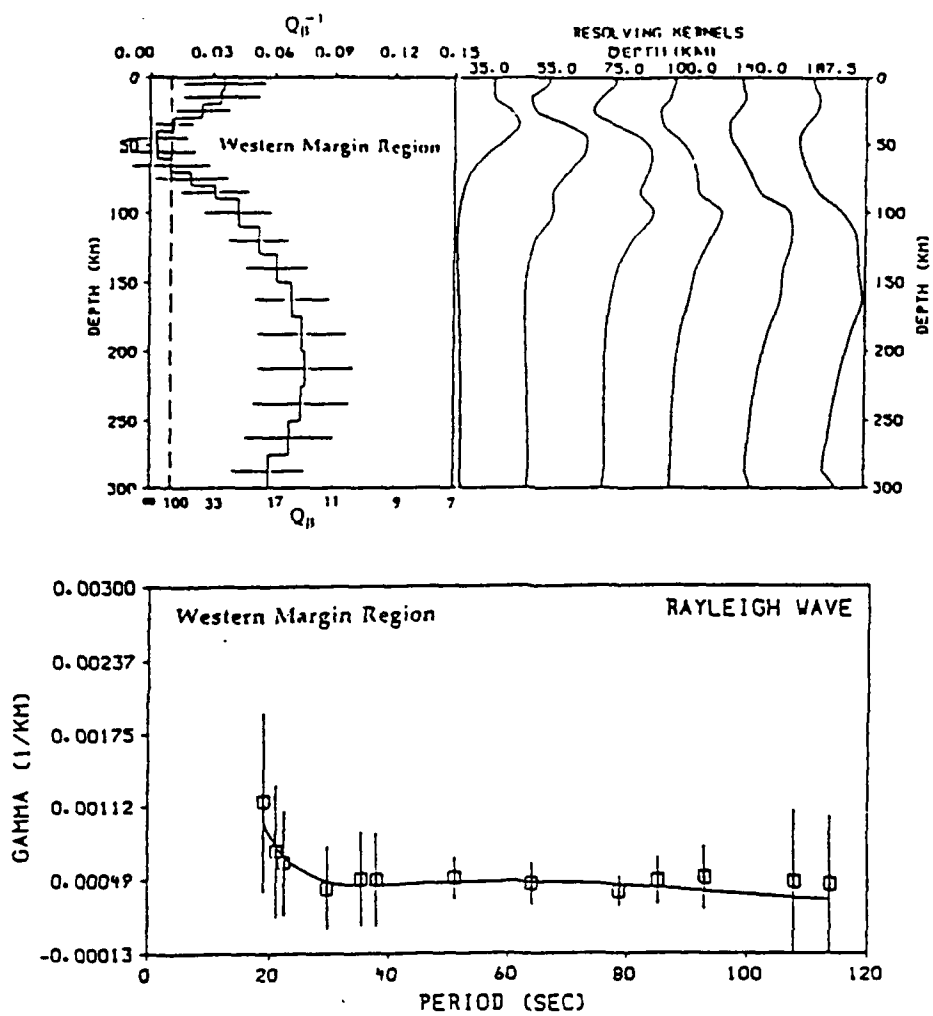


Figure 8

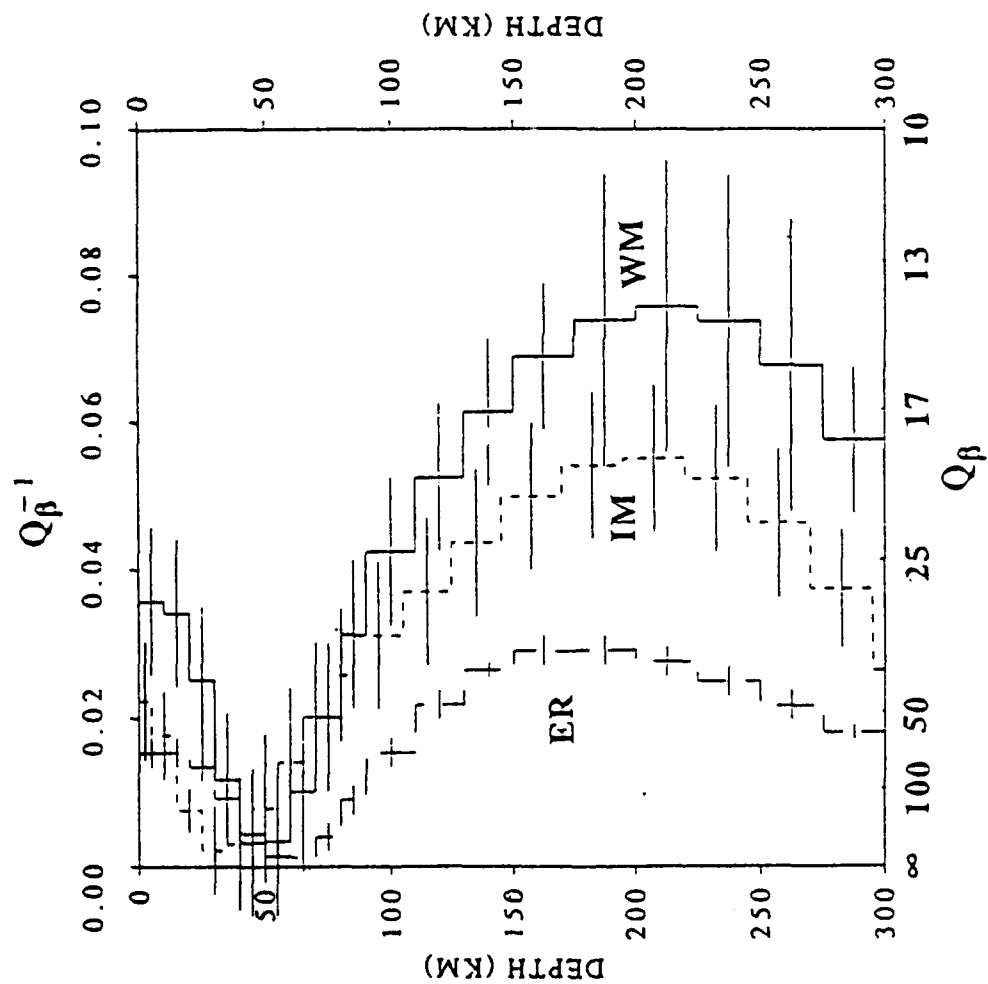


Figure 9



## **Chapter 3**

### **Lg Coda Q Variation Across Eurasia**

**by**

**Jia-kang Xie and Brian J. Mitchell**

## ABSTRACT

Broad-band digital data from four IRIS, six CDSN, and three GDSN stations in the USSR, China, and southeast Asia have been collected to study Lg coda  $Q$  in Eurasia. More than 200 records from earthquakes and underground nuclear explosions have been analyzed with a stacked spectral ratio method. Assuming that Lg coda  $Q$  satisfies the relationship  $Q(f) = Q_0 f^\eta$ , where  $Q_0$  and  $\eta$  are  $Q$  at 1 Hz and the power law frequency dependence of  $Q$ , respectively. A tomographic inversion results in a complex pattern of  $Q_0$  values. Maximum  $Q_0$  values are about 700, relatively low for a stable region. The broadest region of low  $Q_0$  values (200-300) occurs through western China, northern India and adjacent regions of central Asia where plate collision has produced intense tectonic activity. Other regions of low  $Q_0$  values lie in, and east of, the Caspian Sea, and in western Turkey. High values of  $Q_0$  (up to 700) occur throughout most of northern Europe and Asia. Bands of moderately high values of  $Q_0$  (450-550) lie between the Black and Caspian Seas and in eastern China. Frequency dependence values show no clear relationship to the  $Q_0$  values. They are highest (1.0) in a region of northern Siberia where  $Q_0$  takes on intermediate values.

Uncertainties in the  $Q_0$  and  $\eta$  estimates are relatively high in some regions such as the Arabian peninsula, India, eastern China and the northwestern portion of our area of study. It is expected that digital stations currently being installed, or planned for the near future, will considerably improve  $Q_0$  and  $\eta$  estimates for some of those regions and that analog records will improve them for others.

## INTRODUCTION

Although seismic tomography has been used successfully for several years to study lateral variations of velocity, it has only recently been used to study lateral variations of  $Q$  (Xie and Mitchell, 1990). This development required that Lg coda  $Q$  be measured with relatively high precision. Such precision was achieved with the stacked spectral ratio (SSR) method of Xie and Nuttli (1988).

### Stacked Spectral Ratios

The SSR method is applied to the coda of Lg waves (Figure 1) and provides information on  $Q$  averaged over the areas of ellipses (Figure 2) which represent areas over which scattered waves sample. We used a total of more than 200 Lg coda time series. Each of the coda time series were segmented by many windows with centered lapse times starting at roughly the arrival of group velocity of  $3.15 \text{ km s}^{-1}$  and increasing to successively cover the entire signal which can be distinguished from the ambient noise. We used a 10% Hanning window with a length of 30 s for the digitized analogue data and a length of 25.6 s for the digital GDSN data. The reference noise spectra for each record were obtained in the way described by Xie and Nuttli (1988), i.e., from the portion of the trace prior to the P arrival. The Fast Fourier

transform (FFT) was performed on both signal and noise and the effect of noise was empirically reduced by subtracting the reference power spectra of noise from power spectra of the signal. The SSR was then obtained for single-trace  $Q$  measurements. Figure 3 gives some examples of the SSR analysis over the frequency band from 0.2 to 2.0 Hz.

In order to stabilize the  $Q$ -inversion using the random coda signal, many windows are needed in the SSR method; thus we must use the later part of coda. The increased stability and the reduced uncertainty due to using the later coda, however, is achieved at the cost of poorer spatial resolving power of later coda since it samples a larger area. Eventually one achieves an acceptable uncertainty in coda  $Q$  inversion with limited spatial resolution.

The effect of random noise preserved in single-trace  $Q$  estimates on the final image can be empirically tested utilizing the sample standard error in  $Q_n$  due to the randomness of SSRs (Xie and Nuttli, 1988). To do so we denote the standard error associated with  $Q_n$  by  $\delta Q_n$ ,  $n = 1, 2, 3, \dots, N_g$  (note that  $\delta Q_n$  is always positive due to the way standard error is estimated), and assume that  $\delta Q_n$  gives a good measure of the absolute value of real error preserved in the corresponding  $Q$  measurements. We then empirically construct a number of noise series, whose  $n$ th member has an absolute value equal to  $\delta Q_n$  and a sign that is chosen randomly. The  $n$ th term of this noise series is then added to  $Q_n$ , which we shall denote as

$$\overline{Q}'_n = \overline{Q}_n + \delta Q_n$$

$\overline{Q}'_n$  values were then inverted to obtain a new  $Q_m$  model. The difference between the new image of  $Q_m$  values using  $\overline{Q}'_n$  and the original image of  $Q_m$  values will give us an error estimation for the  $Q_m$  values. This process empirically measures the effect of random noise on the  $Q_m$  image. The sign of the  $\delta Q_n$  series can be simulated by pseudorandom binary generators in a computer and the process must be repeated several times to obtain an average, and more stable error measurement of  $Q_m$  values.

### Lg Coda Tomography

Xie and Mitchell (1990) developed a back-projection method which they applied to Lg coda to obtain a tomographic image of Lg coda  $Q$  in Africa. That continent was divided into several grids ( $N_g$ ) where  $Q_m$  was assumed to be constant within the  $n$ th grid. If the areal average of Lg coda  $Q$  ( $Q_n$ ) in the elliptical area sampled by coda waves is obtained at maximum lapse time, then denoting the area of the  $n$ th ellipse that overlaps the  $n$ th grid by  $S_{mn, N_g}$ , we have

$$\frac{1}{Q_n} = \frac{1}{S_n} \sum_{N_g}^{m=1} \frac{S_{mn}}{Q_m} + E_n \quad n = 1, 2, \dots, N_d \quad (1)$$

where  $S_n$  is the summation of  $s_n$  over the ellipse and  $E_n$  is the residual due to errors in modelling Lg coda and in the  $Q$  measurement.

### Lateral Variations of Lg Coda Q

The back projection method described above is applied to image lateral variations of Lg coda Q in central and southern Eurasia. We have divided the whole area into grids with widths equal to  $3^\circ$  in latitude and longitude. The grids cover about 75% of the region between latitudes  $10^\circ$  to  $60^\circ$  north and  $25^\circ$  to  $135^\circ$  east.

Figure 4 is the image of Lg coda Q variation at 1 Hz. Several features are apparent from that map. A broad region of low  $Q_0$  values, between 200 and 300, spans western China, northern India, and adjacent regions of central Asia. More localized regions of low  $Q_0$  values lie within, and near, the Caspian Sea and in western Turkey. High values of  $Q_0$  (up to 700) occur across most of northern Europe and Asia. Bands characterized by intermediate values of  $Q_0$  (450-550) lie between the Black and Caspian Seas and in eastern China. The error distribution of the  $Q_0$  appears in Figure 5. As expected the regions with largest errors occur near the periphery of the map where path coverage is sparsest. Frequency dependence values near 1 Hz were determined in the same way as that in Africa (Xie and Mitchell, 1990). Those values for frequency dependence in Figure 6 show no clear relationship to the  $Q_0$  values. They are highest (1.0) in a portion of northern Siberia where  $Q_0$  values are high and lowest (0.0) in southeast Asia where  $Q_0$  takes on intermediate values. It should be noted, however, that the presently available values in southeast Asia, as well as some others (Figure 7), are characterized by relatively large errors.

### Resolution and Errors

The imaging of Lg coda Q variations is inherently limited because of the trade-off between the stability and the spatial resolving power. For this reason it is important that any study of Lg coda Q variations include an analysis of resolution and error. We have calculated point spreading functions (psf) to estimate the resolving power at the locations where these grids are centered. All of the psf determinations were normalized such that the maximum values are unity. In general, the degree of spreading of psf's increases as the density of coverage decreases.

Figure 8 shows example point spreading functions centered on four widely spaced grids. The broadest psf occurs in the northeastern portion of the map where path coverage is poor.

The psf plots allow us to determine whether or not features of the  $Q_0$  and  $\eta$  images are real or whether they are simply artifacts of poor resolution. The low-Q region just south of the Caspian Sea (Figure 4) is of particular interest. It has long been known that the Caspian Sea is characterized by high attenuation, but our results suggest that those low Q values extend well to the south of the sea. The psf in that region suggests that the southern extension of that low-Q region is real and is not a result of poor resolution.

### Conclusions

$Q_0$  values throughout central and southern Asia range between 200 and 700 and frequency dependence values range between 0.3 and nearly 1.0. No clear relation is apparent between those values. Lowest  $Q_0$  values occur in and south of the Caspian Sea, near the Black Sea, and in a broad band from India to western China. Highest values occur in northern Asia.

Uncertainties in  $Q_0$  and  $\eta$  estimates are high in regions around the periphery of the study area. Additional data with better station coverage will be necessary to reduce those uncertainties.

### References

- Xie, J., and O.W. Nuttli, Interpretation of high-frequency coda at large distances: stochastic modelling and method of inversion, *Geophys. J.*, 95, 579-595, 1988.
- Xie, J., and B.J. Mitchell, A back-projection method for imaging large-scale lateral variations of Lg coda Q with application to continental Africa, *Geophys. J. Int.*, 100, 161-181, 1990.

### Figure Captions

Figure 1. Vertical component seismograms from three stations in China. The abscissa indicates the lapse time measured from the earthquake origin time.

Figure 2. Sampling pattern of Lg coda used in this study. Each record of Lg coda is assumed to sample an elliptical area corresponding to the maximum lapse time used in the analysis. When the continental boundary is encountered it is assumed to be a barrier to the Lg wave and the sampling area is taken to be bounded by that boundary rather than by the oceanic portion of the ellipse.

Figure 3. Stacked spectral ratios from which  $Q_0$  ( $Q$  at 1 Hz) and the frequency dependence of Lg coda  $Q$  are obtained. Those parameters are determined by linear regression at frequencies between 0.2 and 2.0 Hz.

Figure 4. Lg coda  $Q_0$  values obtained in this study.

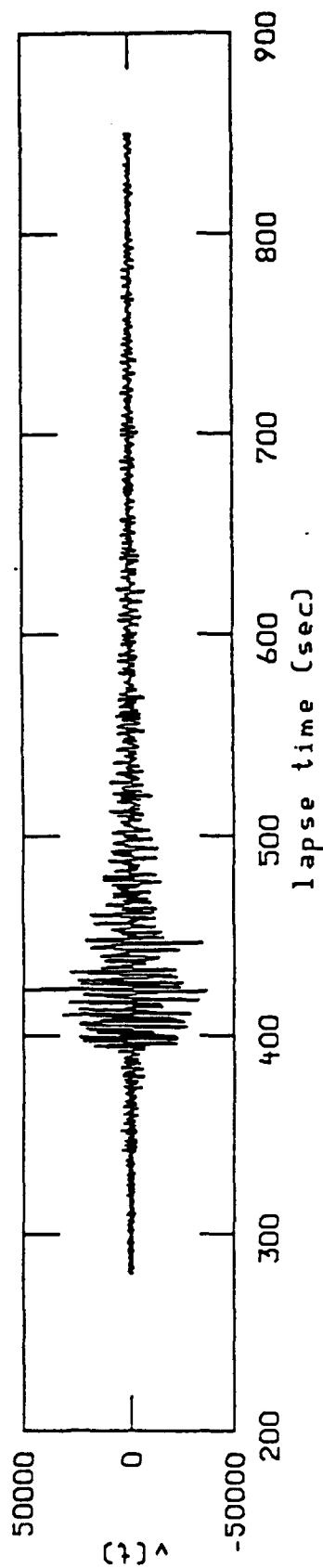
Figure 5. Error distribution for the image of  $Q_0$  variations.

Figure 6. Frequency dependence of Lg coda  $Q$  at frequencies near 1 Hz.

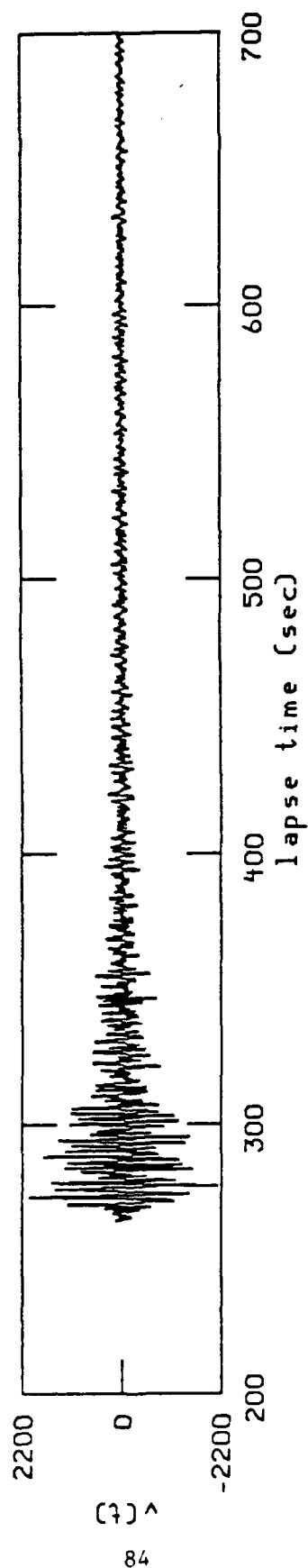
Figure 7. Error distribution for the image of  $\eta$  variations.

Figure 8. Point spreading function plots for four related grids.

MAY 13 1989, BJI, 1400.0 KM



JUL 02 1989, HIA, 938.6 KM



MAY 03 1989, KMI, 633.3 KM

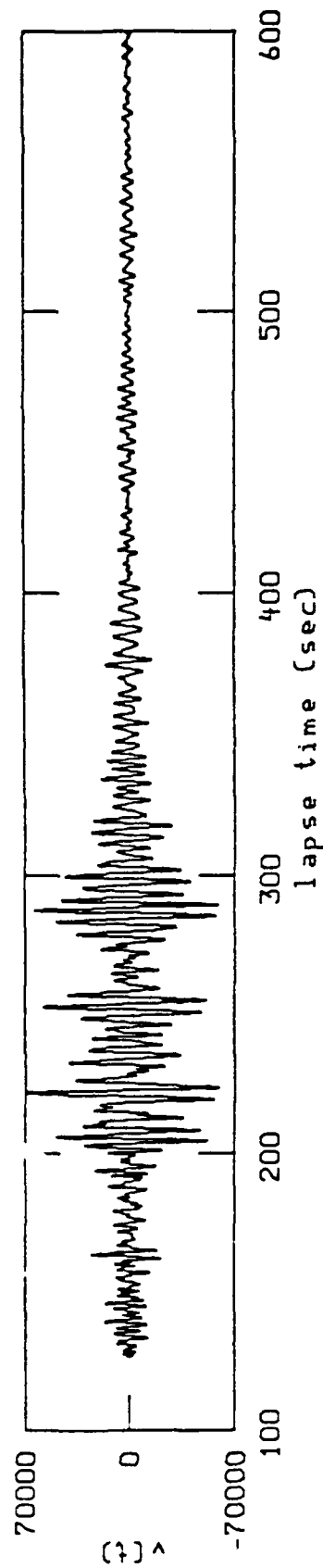


Figure 1



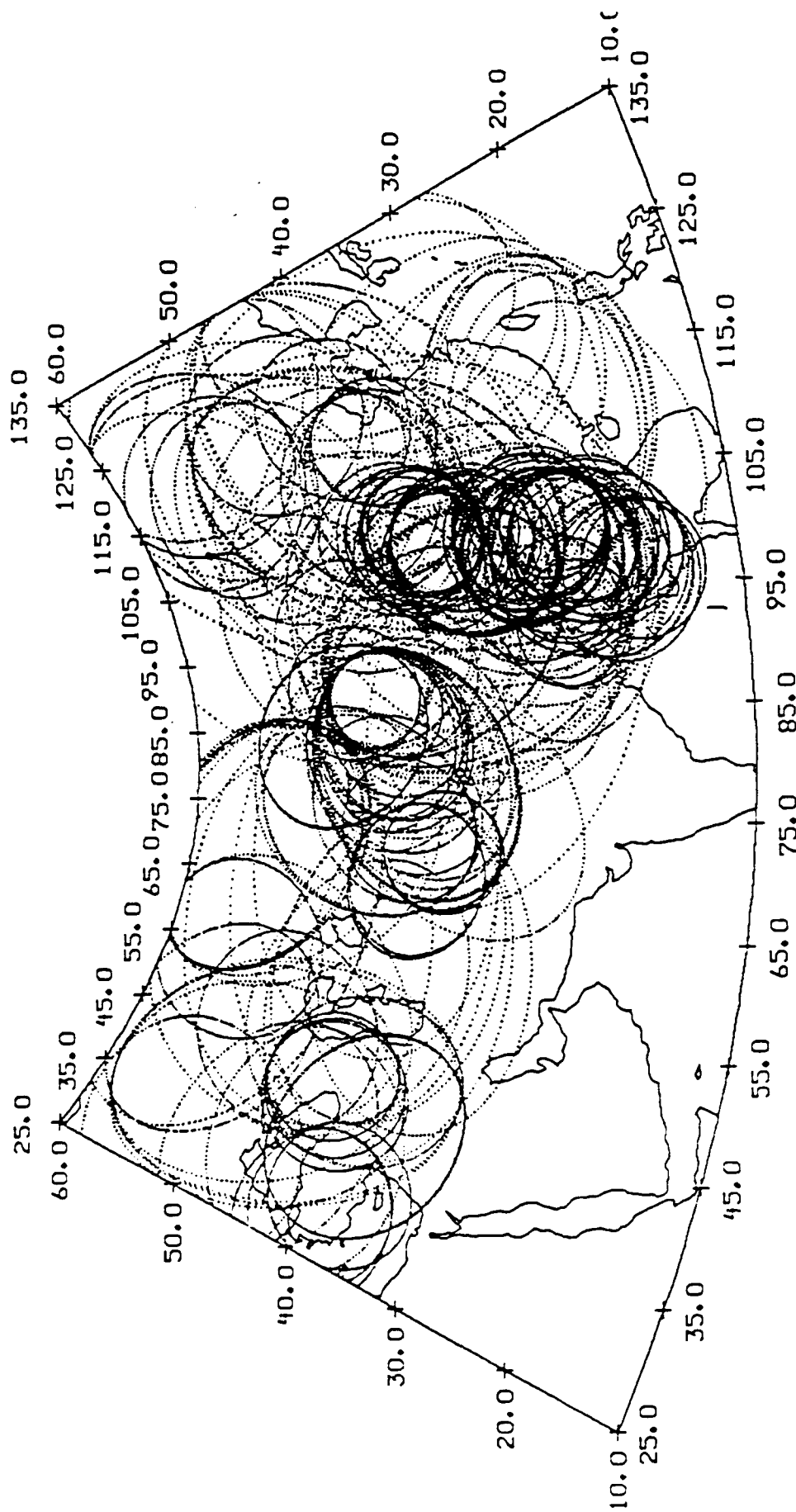
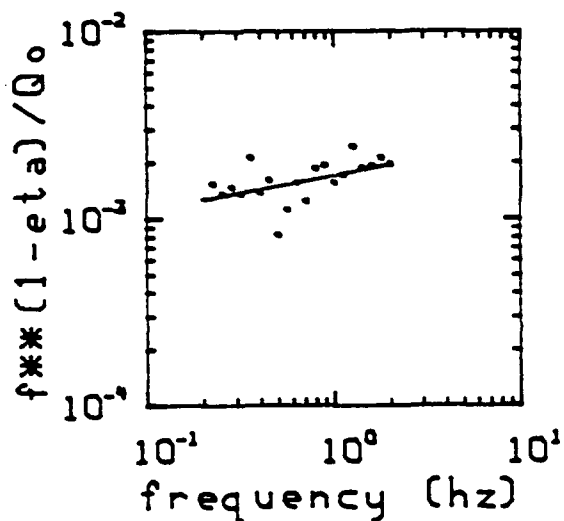


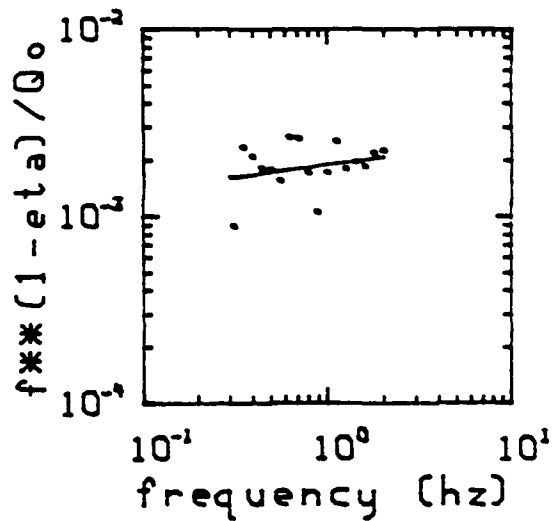
Figure 2

$Q_0 = 576.6 \pm 140.9$ ,  $\eta_2 = 0.75 \pm 0.10$

$Q_0 = 519.7 \pm 157.0$ ,  $\eta_2 = 0.87 \pm 0.13$



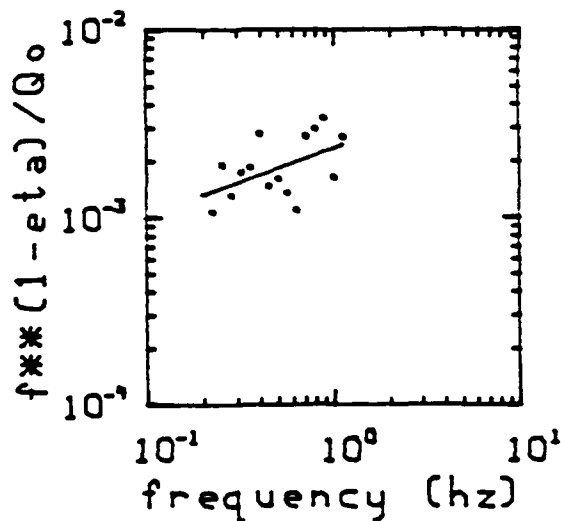
ARU, SEP 14 1990



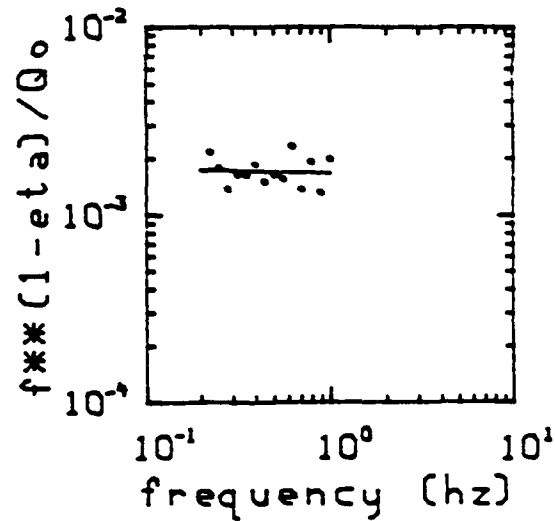
GAR, SEP 14 1990

$Q_0 = 419.8 \pm 153.4$ ,  $\eta_2 = 0.64 \pm 0.17$

$Q_0 = 600.0 \pm 120.5$ ,  $\eta_2 = 1.02 \pm 0.10$



KIV, SEP 14 1990



OBN (LOV GAIN), SEP 14 1990

Figure 3

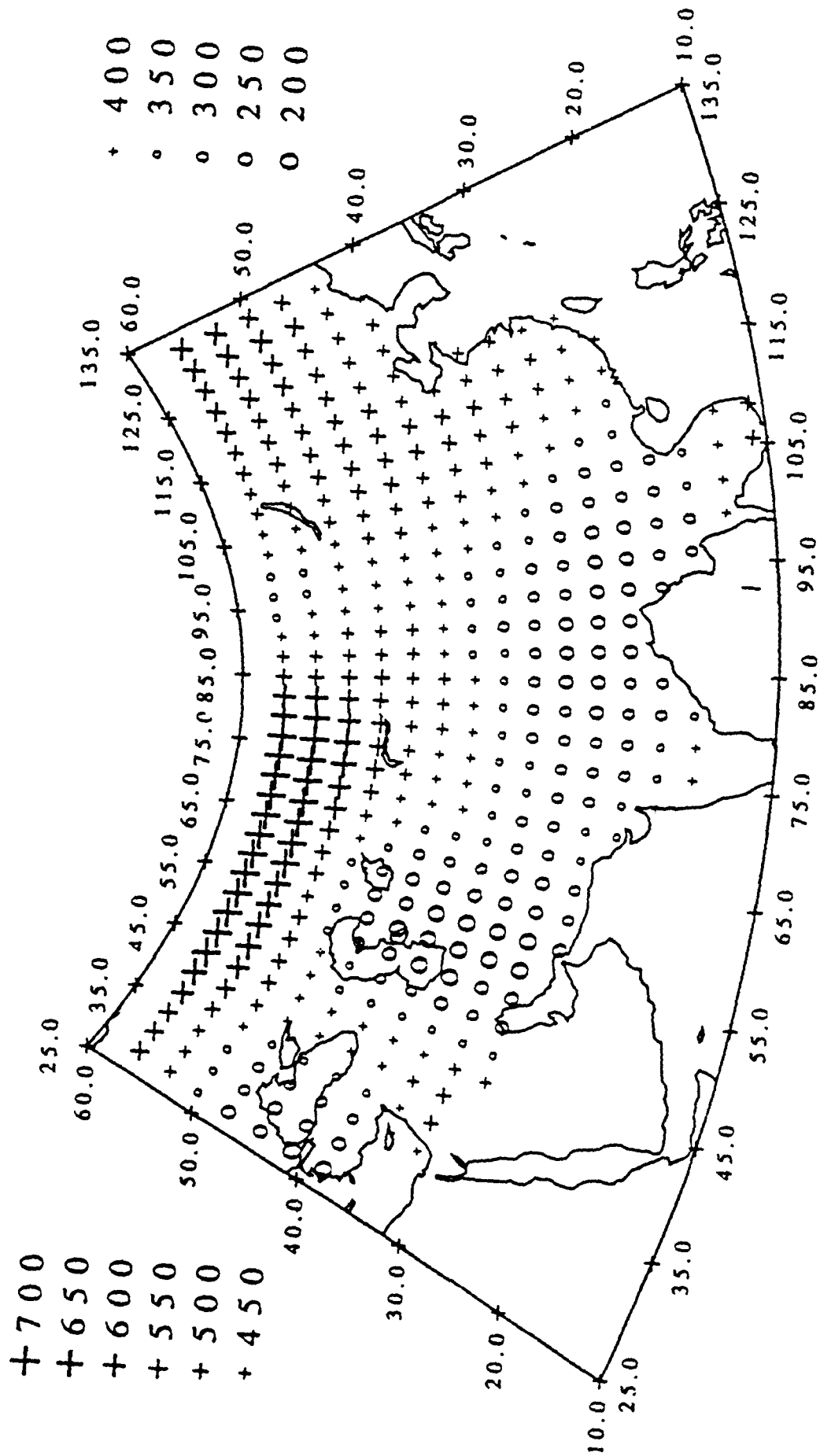


Figure 4

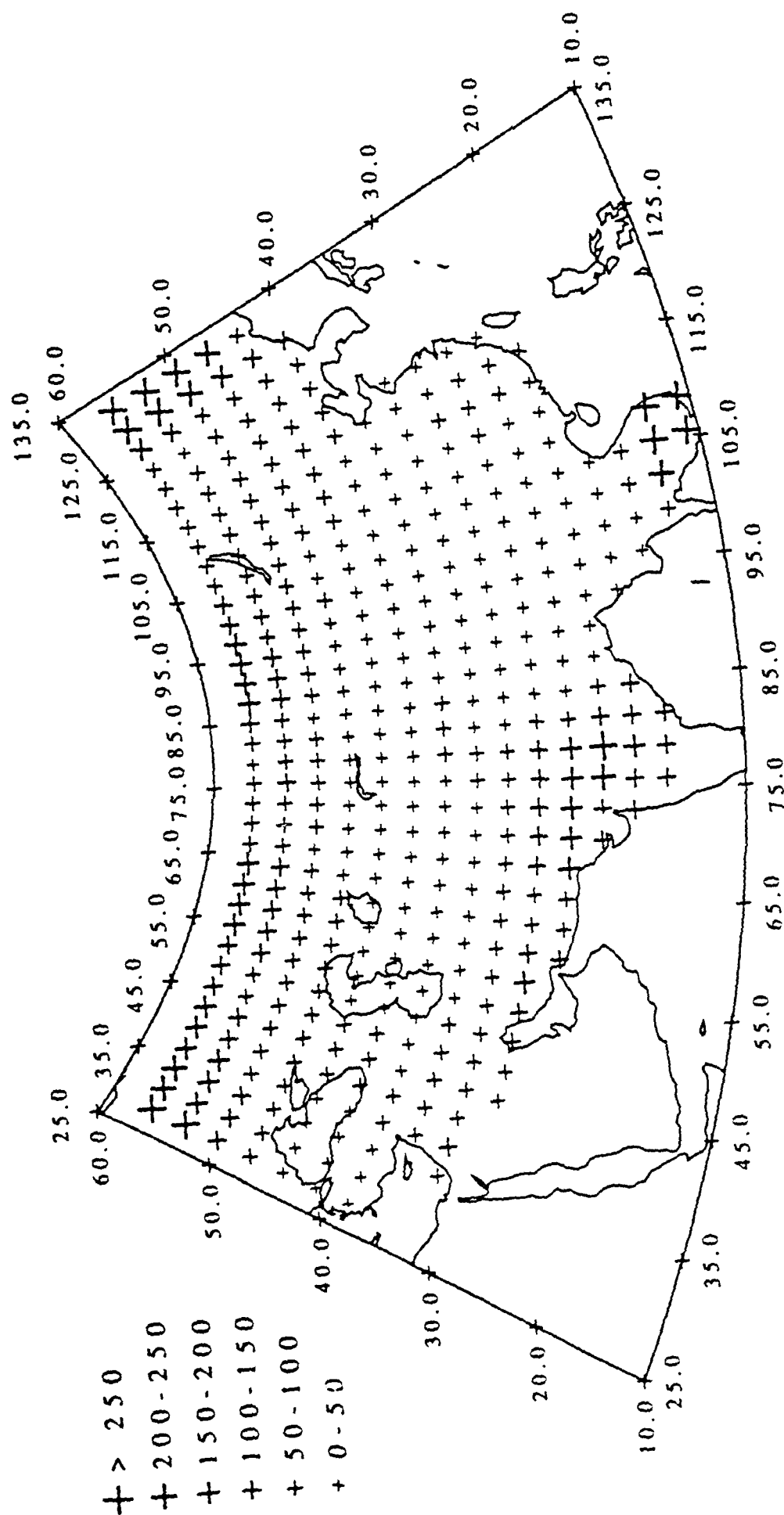


Figure 5

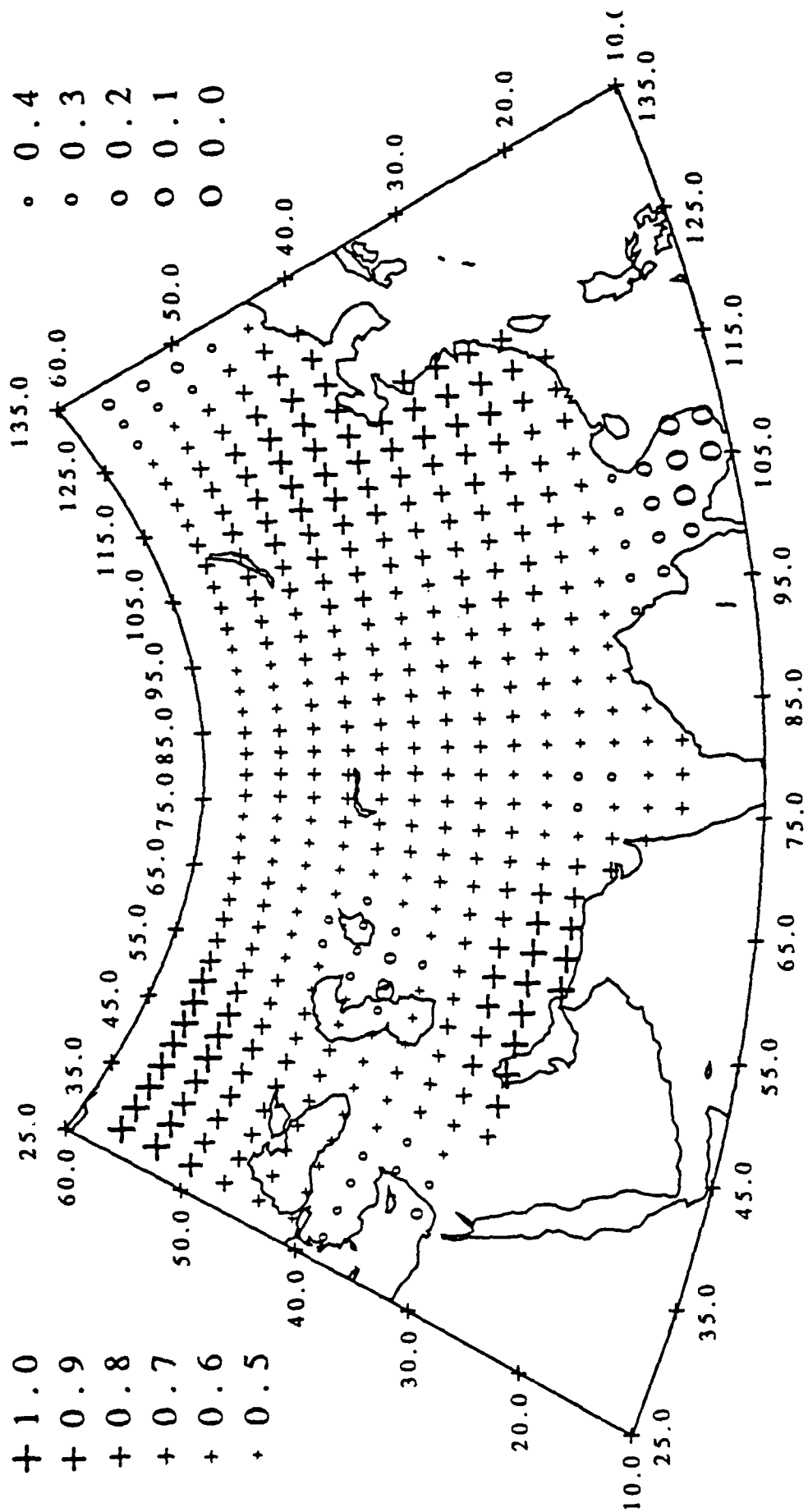


Figure 6

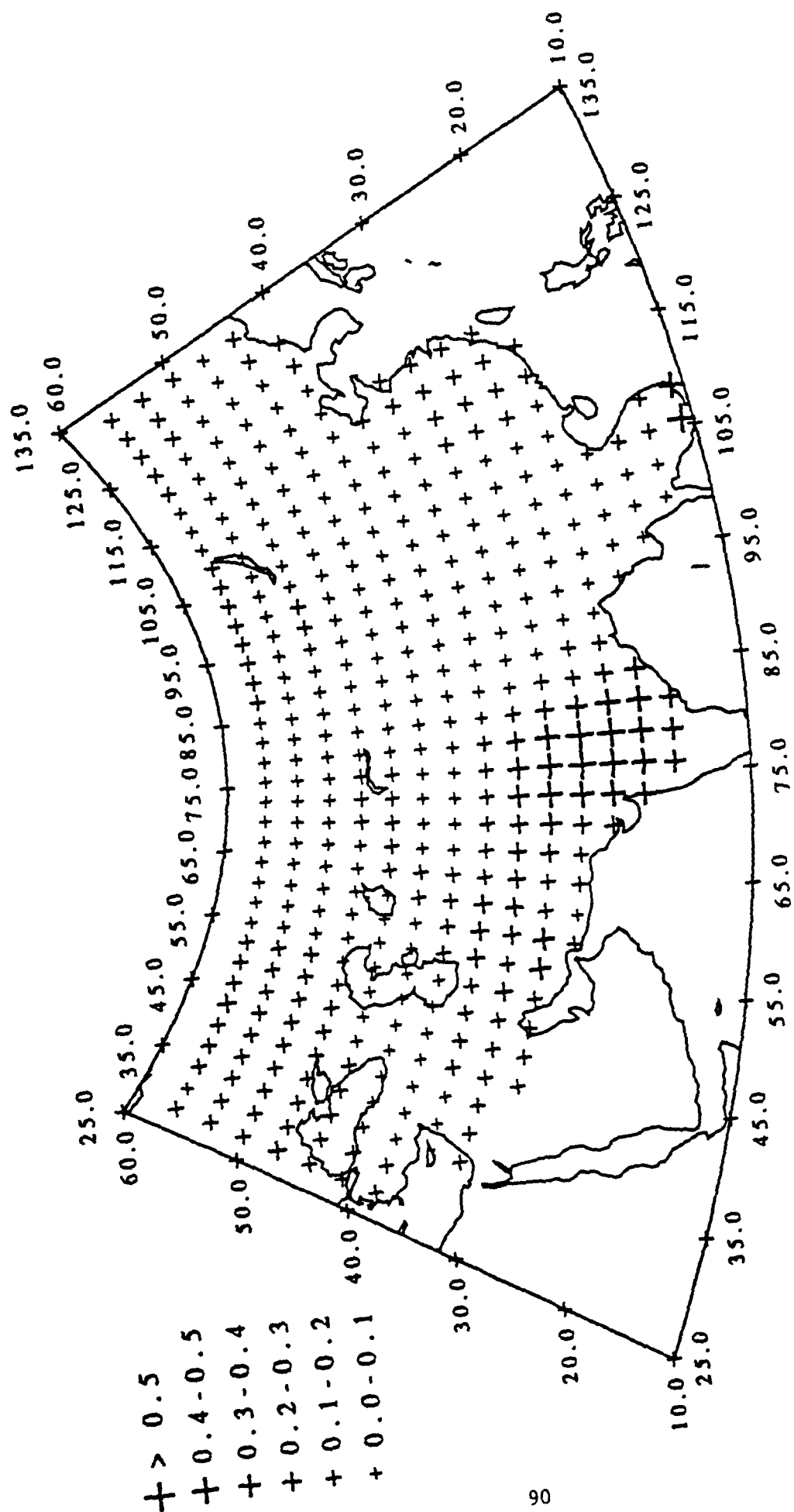


Figure 7

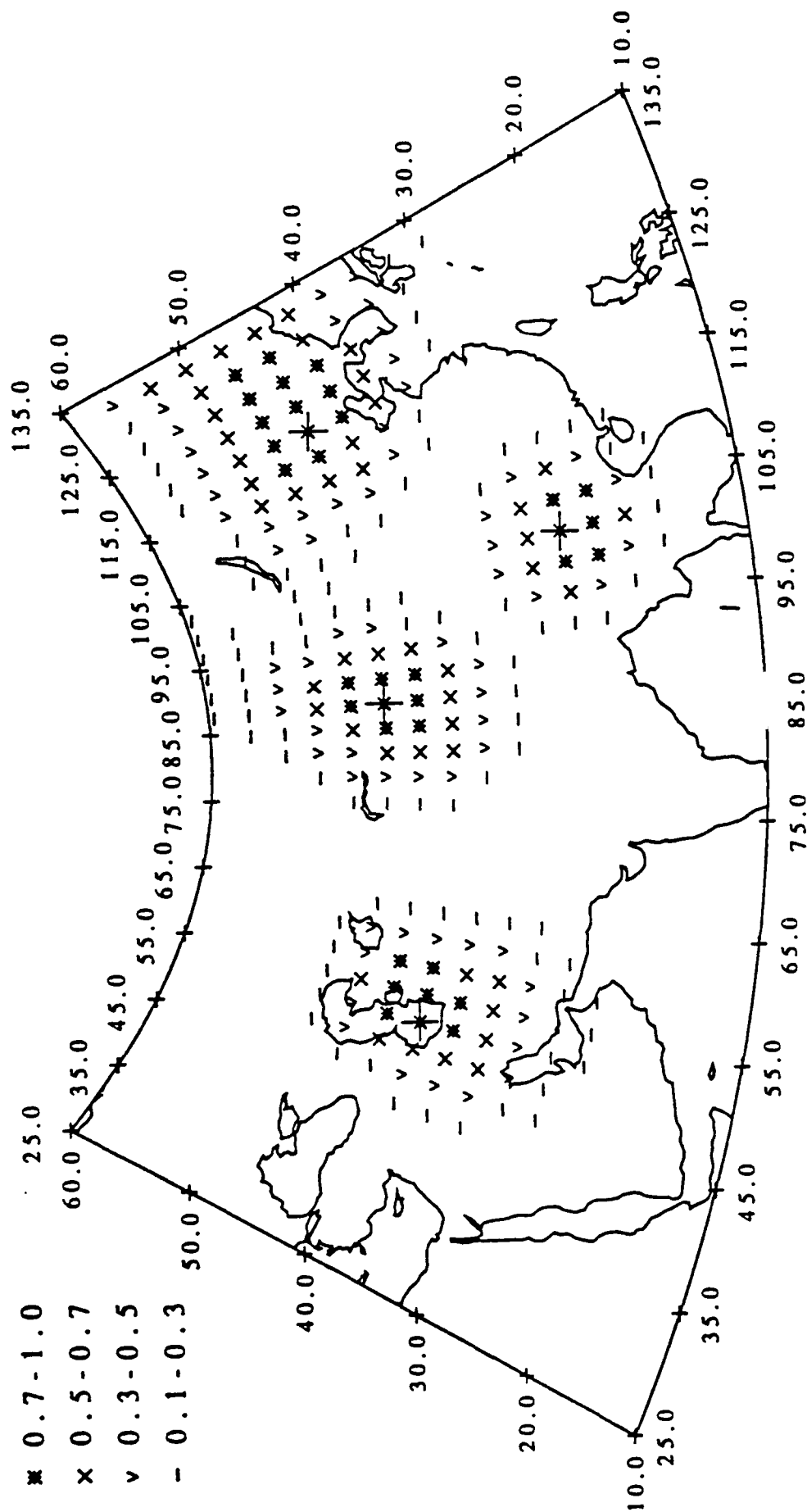


Figure 8

## Chapter 4

### Attenuation of Surface Waves Across the Arabian Peninsula

by

Dogan Seber and Brian J. Mitchell



## ABSTRACT

Amplitude spectra of fundamental-mode Rayleigh and Love waves are used to determine shear-wave  $Q$  ( $Q_\beta$ ) models for the upper crust of the Arabian peninsula. The observed spectra are compared to theoretical spectra computed for earthquakes with known fault-plane solutions. Shear-wave  $Q$  in the upper crust can be obtained by trial-and-error modeling to fit the the slope of the amplitude spectra at short periods (5-30 s), if the source time function is less than about 6 s and if the depth of the earthquake is known to within about 3 km. Shear-velocity  $Q$  values obtained in this way vary from about 60 along the margin of the Red Sea to 100-150 in the central part of the peninsula, to 65-80 in the eastern folded region. These values are unusually low for a stable region and suggest that observed anelasticity there is affected by tectonic and epeirogenic activity which has occurred over the past 30 m.y. The shear-wave  $Q$  models derived from surface waves at periods of 5-30 s closely predict reported values of  $L_g$   $Q$  at 1 Hz; shear-wave  $Q$  therefore appears to be independent of frequency in this region at periods between about 1 and 30 s

## INTRODUCTION

The Arabian peninsula is a relatively small stable continental plate surrounded by two active spreading centers and a zone of continent-continent collision. The crusts of most shields and stable platforms are characterized by low attenuation of seismic waves ( e.g. Mitchell, 1973; Hwang and Mitchell, 1987) whereas high rates of attenuation characterize spreading centers (e.g. Canas *et*

*al.*, 1980; Chan *et al.*, 1989) and zones of plate convergence (Hwang and Mitchell, 1987; Correig *et al.*, 1990). It is therefore interesting to study seismic wave attenuation in the Arabian peninsula to determine if it is low, as it should be if it is typical of that for other shields; or if it is high, as it would be if crustal anelasticity there is influenced by tectonic process along the borders of the Arabian plate.

This study presents determinations of seismic Q for the upper crust of the Arabian peninsula. Various paths across the peninsula allow us to investigate the regional variation of Q to learn whether or not paths close to the Red Sea spreading center differ in their attenuation characteristics from those further to the east. As a by-product of this research, dispersion of Rayleigh and Love waves is determined for several paths across the peninsula and is inverted for the shear wave structure of the crust and upper mantle.

### **Tectonic and Structural Setting**

The geodynamic processes which are active in the Red Sea affect the present geology and tectonics of western Arabia (El-Isa and Shanti, 1989). Geological and geophysical studies indicate that the sea is still opening and that new oceanic crust is being formed there (Girdler and Styles, 1974; Girdler and Underwood 1985 ; Mooney

*et al.* 1985). An area to the south of the Peninsula, in the Gulf of Aden, is also a spreading center. Both the Red Sea and the Gulf of Aden spreading centers are cut by many transform faults oriented in a NE-SW direction (El-Isa and Shanti 1989 ; Fairhead and Girdler 1970). The Arabian Plate is colliding with the Turkish plateau in the north, and with the Persian plateau in the east (McKenzie, 1972). Tectonically, the Arabian Peninsula can be divided into three units (Knopoff and Fouda, 1975). The first unit is the Arabian shield which covers almost one forth of the entire peninsula (Figure 1). The second unit is the stable shelf which surrounds the shield, and the third unit contains the folded zones.

The first unit, which is composed of metasediments, granitic rocks, basic and ultrabasic rocks and volcanic rocks is crossed by many faults that trend northwestward (Brown, 1970). The second unit, the stable shelf, is crossed by major faults. The third unit is the region where most of the folding occurs in the peninsula.

The United States Geological Survey and the Directorate General of Mineral Resources of Saudi Arabia conducted a deep seismic refraction profile to obtain a crustal and upper mantle velocity model for the shield. The results of this research show that P-wave velocities in the crust of the Arabian Shield are about 6.3 km/s in the upper crust, about 7.0 km/s in the lower crust, and between 8.0 and 8.2 km/s in the upper mantle (Mooney *et al.*, 1985). The average crustal thickness is about 40 km but thins to 20 km in the coastal region near the Red Sea. Niazi (1968) obtained an average crustal and upper mantle velocity model using phase and group velocity dispersion curves for the path between stations AAE (Addis Ababa) and SHI (Shiraz). His estimation for the shear velocities was 3.4 km/s for the upper crust, 3.6 km/s for the lower crust and 4.6-4.9 km/s for the upper mantle. Knopoff and Fouda (1975) measured the phase velocity of Rayleigh waves across the Arabian peninsula using three different profiles. They found that there is a low-velocity channel for S-waves throughout the region at a depth of 100-140 km. In the channel the velocities are about 4.25-4.45 km/s. Just above this low velocity zone the shear velocities are about 4.55 or 4.65-4.75 km/s. Ghalib (1987) also determined velocity models from Rayleigh wave dispersion curves. His results indicate shear velocities of about 2-3 km/s near the surface, increasing to about 5 km/s at a depth of 100 km.

#### Surface Wave Attenuation Studies

No measurements of attenuation, from which intrinsic values of  $Q$  for the deep crust and upper mantle can be inferred, have been made for the Arabian peninsula. Ghalib (1987), however, determined  $L_g$  wave attenuation coefficients

and their frequency dependence in the peninsula and surrounding areas. His results show that  $L_g$  attenuation values in the region at frequencies near 1 Hz, vary between 150 and 250 and the frequency dependence of  $L_g Q$  is about 0.6-0.7. Mokhtar (1987) determined the attenuation characteristics in the Arabian Shield at very shallow depths (  $< .5$  km ) using short-period Rayleigh waves obtained from a deep seismic refraction profile transversing the shield. He found that at shallow depths  $Q_\beta$  values vary between 30 and 150.

Various methods have been used to determine  $Q$  at greater depths using seismic surface waves. These include the two-station method where the fall-off of spectral amplitudes is measured directly at two stations along a great circle path from an earthquake (Tsai and Aki, 1969), radiation pattern fitting methods where observed spectral amplitudes are compared with theoretical amplitudes predicted by earthquakes with known fault-plane solutions (Tsai and Aki, 1969), and methods where shapes of amplitude spectra are compared with predicted spectra (Cheng and Mitchell, 1981; Chan *et al.*, 1989). For the last of these methods, Cheng and Mitchell (1981) utilized fundamental-mode and higher-mode Rayleigh waves, whereas Chan *et al.*, (1989) utilized only fundamental-mode waves, but were able to use both Rayleigh and Love waves to advantage.

Two-station paths were not available in the present study, nor was the azimuthal coverage adequate for utilizing radiation pattern methods. The method remaining for us is that of fitting spectral shapes. Because higher modes were poorly recorded on the seismograms available to us, we used the method of Chan *et al.* (1989) where spectral fits were sought for fundamental-mode Love and Rayleigh waves.

## DATA ACQUISITION AND PROCESSING

Data for this study consist of surface waves recorded on long-period instruments at three WWSSN seismic stations, SHI(Shiraz), TAB(Tabriz), and JER (Jerusalem). Five earthquakes, all with known fault-plane solutions, were

employed, four of which occurred in the gulf of Aden, and one in the Red Sea (Figure 1). The location and fault parameters for these events are given in Table 1. The seismograms were digitized at 1 s intervals and the NS and EW components were rotated to obtain the transverse component of ground motion. To separate noise and other modes from the fundamental mode, the seismograms were phase-match filtered using the method developed by Herrin and Goforth(1977). Surface wave group velocities and amplitudes were obtained from a multiple filter analysis (Dziewonski *et al.*, 1969) using the vertical component for Rayleigh and the transverse component for Love waves.

### Velocity Models

Shear velocity structure was determined in two regions, western and eastern, of the peninsula. Average Love and Rayleigh wave group velocity dispersion curves were obtained for these two regions and inverted for velocity structure.

The inversion program used in this study, coded by D. Russell and R. B. Herrmann, makes use of partial derivatives with respect to layer parameters. Group and phase velocities are first calculated for an initial model and partial derivatives of phase and group velocities with respect to shear and compressional velocities are obtained numerically. Compressional velocities are not determined directly in the inversion procedure, but are calculated from shear velocities by assuming a value for Poisson's ratio.

An inversion procedure given by Lawson and Hanson (1974) is used to find the unknown parameters. If  $x$  is the vector containing the unknown parameters,  $A$  is the matrix containing the partial derivatives of  $U$  with respect to the unknown parameters, and  $b$  is the difference between observational and theoretical values, then the least-squares solution to this problem is

$$(Ax-b)^T (Ax-b)+\sigma^2 x^T x= \min. \quad (1)$$

where  $\sigma$  is an adjustable damping parameter which determines the tradeoff between resolution and standard deviations in the model and can be set to achieve a desired degree of smoothness. Matrix  $A$  can be written in terms of multiplication of three matrices by using a singular decomposition technique.

$$A = U \Lambda V^T \quad (2)$$

$U$  and  $V$  matrices satisfy the relation

$$UU^T = U^T U = VV^T = V^T V = I \quad (3)$$

where  $I$  is the identity matrix. Then the unknown parameter vector can be written

$$x = V(\Lambda^2 + \sigma^2 I)^{-1} \Lambda U^T b, \quad (4)$$

the variance-covariance matrix  $C$  is

$$C = V(\Lambda^2 + \sigma^2 I)^{-1} \Lambda^2 (\Lambda^2 + \sigma^2 I)^{-1} V^T, \quad (5)$$

and the resolution matrix  $R$  is

$$R = V(\Lambda^2 + \sigma^2 I)^{-1} \Lambda^2 V^T. \quad (6)$$

In the inversion procedure a 15-layer model was used where the maximum depth of interest was taken to be 120 km. By using a large number of layers and underdetermined approach we avoid forcing features into a model which might be obtained using layers which are thicker than those in the Earth. Smoothness can be forced into the model by selecting a suitable value for the damping factor  $\sigma$ . The ratio of compressional velocity to shear velocity has been held at  $\sqrt{3}$ , which implies that Poisson's ratio is 0.25. Observed and predicted group velocity dispersion curves, and the corresponding shear velocity structures for the western and eastern part of the peninsula are given in Figures 2 and 3. As seen from Figure 2, standard deviations for Love and Rayleigh wave group velocities

are greater for the western region. This is probably due to the complex tectonic structure there. The western peninsula velocity model (Figure 2) includes a low-velocity zone starting at a depth of about 70 km. The resolving kernels, however, are poor at this depth. Since the Red Sea is an active spreading center, a low-velocity zone under that part of the peninsula is not unexpected. The eastern region does not include a significant low-velocity zone in the same depth range. In the eastern region shear velocities in the crust are lower than those of the western region. Because of the absence of a low-velocity zone in the eastern model, they are, however, higher than those in the western region at depths greater than 70 km.

### THEORETICAL SPECTRA

Theoretical spectra were calculated using the formulation of Haskell (1963,1964) as programmed by Wang (1981). The calculations require knowledge of the earthquake focal parameters and the velocity-density-Q model along the path of propagation. The focal parameters include the depth, strike and slip of the fault as well as the source time function and moment. The effects of all these parameters except moment on amplitude spectra will be examined in the following paragraphs. Moment is neglected because it affects only the level and not the slope of the spectra.

To study the effects of different source and fault parameters on the surface wave amplitude spectra, we performed a sensitivity analysis. The spectra were calculated for a source having a depth of 5 km, a dip of 30°, a slip of 30°, a strike of 30°, a four-second parabolic source-time function and a moment of  $5 \cdot 10^{24}$  dyne-cm, using the eastern peninsula model. Spectra were computed for an imaginary station, 2000 km away from the source and at an azimuth of 0°. The Q values were taken to be 150 for the first 20 km and 300 for the underlying half space. Spectra were computed for cases in which each parameter was allowed to vary through a range of values while holding the others fixed at the above

values.

#### *The effect of focal depth*

The effect of the focal depth on the spectra has been studied by many authors (Tsai and Aki, 1970,1971; Ben-Menahem and Singh,1981). In this study, the effect of focal depth on the Rayleigh and Love wave spectra is discussed for focal depths of 5 km, 10km, 15 km, and 20km. The amplitude spectra for these synthetics are given in Figure 4. As the depth of the focus increases, the energy at the shorter periods is reduced for both Rayleigh and Love waves. The Love wave spectrum for the longer periods is much less sensitive to the focal depth than it is for shorter periods. The Rayleigh wave spectra, however, are sensitive to the focal depth at both short and long periods.

#### *The effect of source time function*

The duration of the source time function is important because it will affect the shorter periods of the Rayleigh and Love wave spectra. A parabolic source time function with different durations has been used to calculate the amount of the effect. In Figure 4, the Love and Rayleigh wave spectral amplitudes calculated for 1 sec, 2 sec, 4 sec and 6 sec durations are given. As the duration increases, the effect of source time function also increases at shorter periods. The effect at greater periods is insignificant.

#### *The effect of fault parameters*

Errors in the determination of the fault parameters using P-wave first motion, centroid moment tensors, or surface wave amplitude spectra are thought to be  $\pm 10^\circ$  for each parameter. To see these effects on the synthetic spectra, spectral amplitudes have been calculated for a fault with dip= $30^\circ$ , slip= $30^\circ$ , strike= $30^\circ$ , and  $\pm 10^\circ$  changes in each parameter.

#### *Dip*



The left side of Figure 5 shows the effect of variations in dip angle on the amplitude spectra for Rayleigh and Love waves. The effect of  $\pm 10^\circ$  changes in the dip angle is seen at all period ranges. For Love waves, the spectrum changes in level more than in shape. Rayleigh wave, however, changes its shapes especially at the longer periods.

#### *Strike*

The center diagrams in Figure 5 shows the effect variation of strike on the amplitude spectra. The Rayleigh wave spectrum varies for periods greater than 15 s. Below 15 s there is almost no change on the spectral shape. The Love wave spectra vary over the entire period range between 5 and 50 s, with maximum changes occurring at a period of about 20 s.

#### *Slip*

The right side of Figure 5 shows the effects of variations in slip angle on the spectral amplitudes. The Love wave amplitude spectra are affected more than those of Rayleigh waves, but the change is very small for both cases.

These computations indicate that the spectra of both Love and Rayleigh waves are affected by changes in the fault parameters, with most significant changes occurring at the longer periods. The slopes of the shorter period portions of the spectra are not sensitive to changes in the fault parameters. Since, as we show in the following section, the effect of crustal Q values which we are interested in, is dominant at short periods, errors in fault parameters will not have adverse effects on our results.

#### *The effect of Q*

The effect of Q on the amplitude spectra is investigated in this section. A two-layer Q model is used in which the upper layer with a thickness of 20 km, overlies a half space. The Q values used here are assumed to be independent of frequency. The effect of some changes in the half space Q values on the spectra

are first investigated. The shear wave ( $Q_\beta$ ) values in the half space were allowed to vary between 150 and 1000 and the  $Q$  value in the layer was held constant at 150. The left side of Figure 6 shows the variations in the amplitude spectra of Rayleigh and Love waves. The half space  $Q$  values have no significant effect on the amplitude spectra at the shorter periods. At the longer periods Rayleigh waves are affected more than Love waves, but the changes are relatively small. In the second step  $Q_\beta$  values in the layer were changed while the half space  $Q$  value was held constant at 300. The right side of Figure 6 shows the crustal  $Q$  effect on the Rayleigh and Love wave spectra. As seen from the figure,  $Q_\beta$  values for the upper crust have a large effect on the amplitude spectra at the shorter periods. The  $Q_\beta$  value in the upper crust, in fact, plays the most important role in shaping the Rayleigh and Love wave spectra.

### CALCULATION OF $Q$ VALUES

We have seen that the source-time function, the depth of focus and  $Q$  values in the upper crust are most important parameters which affect the shorter period portion of the spectra. If therefore, we can constrain the depth of focus and the duration of the source-time function, we should be able to use the slope of the shorter period portion of the amplitude spectra to obtain  $Q$  values in the upper crust. We use a methodology which is similar to that of Chan *et al.* (1989) in which  $Q$  in the upper crust is allowed to vary while all other parameters are held at reasonable values. Chan *et al.* (1989) used spectral shapes to obtain  $Q$  values in the Iceland Plateau. Since the crustal thickness is very small near an oceanic ridge, they model asthenospheric  $Q_\beta$  values. Their procedure differs from the present study because they try to match the longer period portion of the amplitude spectra whereas we use the shorter period portion.

The depth of each event should be known fairly well when using this technique. The error limits should not exceed  $\pm 3$  km to obtain a reliable  $Q$  values. The earthquakes that are used in the present study are mid-ocean ridge type

earthquakes, for which the focal depths are usually less than 15 km. In Table 1, the source and fault parameters are given for the earthquakes used. In the forward modeling we started with an initial depth obtained from the ISC and fault parameters obtained from centroid moment tensor solutions. Necessary changes were made whenever the match between observed and theoretical spectra were not satisfactory at the longer periods. Since the Rayleigh wave amplitude spectra are affected over almost all periods with changing depth, it will not be possible to obtain a match at the longer periods if the depth is incorrect, even though we have the correct fault-plane solutions. Another constraint that we can bring into our calculations is to use more than one station for the same earthquake. A single-station amplitude spectrum may be matched by more than one set of fault parameters if the depth of the earthquake is changed. Using two or more station records will more strongly constrain the fault parameters and the depth because the same parameters must satisfy all amplitude spectra. The use of Love wave amplitude spectra to constrain the depth of focus will not be useful because the depth effect is only seen at the shorter periods, where they may trade-off against the effect of  $Q$ . The Love wave spectra may be helpful, however, in constraining the fault parameters since they are very sensitive to those parameters.

The source-time function is the least constrained unknown parameter in our calculations. There is no work that discusses the source characteristics of earthquakes in this region. However, there are many studies that discuss characteristics of earthquakes in other regions ( Tsai and Aki, 1970; Pacheco and Nabelek 1988 ; Chan et al. 1989). Tsai and Aki (1970 ) state that an event of magnitude less than 6 and with a fault length about 10 km will have a rise time of about 1 s. Pacheco and Nabelek (1988) determined the source characteristics of Palm Springs earthquakes having magnitudes of about 6.0 and estimated durations of those earthquakes to be about 4-4.5 s. Chan et al. (1989) estimated source-time durations for mid-ocean ridge earthquakes with magnitudes less

than 5.1 to be about 4.5 s or less. A general conclusion from those studies is that the duration of the source-time function is less than 5 s for an earthquake with a magnitude around 5.0. The earthquakes that we use in the present study have magnitudes between 4.9 and 5.3. For this reason, it is not likely that the duration of source functions will be higher than 5 s for the earthquakes used in this study. Figure 4 indicates that source time functions which might have a significant effect on the spectra have durations of 6 s or greater. For this reason, if the source time duration is less than six seconds, the effect on the calculations will be insignificant. Since six seconds is the minimum duration that might affect our calculated  $Q$  values, uncertainties in source duration should not affect our results. If the duration of the source time function is greater than six seconds, the actual  $Q$  values will be higher than what we obtain. For 10 s duration of the source time function, the estimated increase in the  $Q$  values will be about 20. A 4 s parabolic source time function has been assumed for all events.

In the determination of  $Q$  models we have not been able to use Love wave spectral amplitudes for all stations due to the high noise levels on some seismograms. However, at least one Love wave spectrum for each event was used. The use of Love spectra is important because they help to constrain the fault parameters and also provide additional  $Q$  determinations for the same event and path as that provided by Rayleigh waves.

Event #1 is located in the Gulf of Aden (Figure 1). For this earthquake we have records from two stations, SHI and TAB. Because of the high noise level we could not obtain usable Love wave spectra for station TAB. We therefore have both Love and Rayleigh wave spectra for station SHI and Rayleigh wave spectra only for station TAB. The total of three spectra are sufficient to constrain the depth of focus and the fault parameters. We begin the forward modeling process using initial values of fault parameters obtained from published centroid moment tensor solutions and an initial value of depth obtained by the ISC. We observe the match between theoretical and observed spectra at the longer

periods and change the model parameters and the depth value until we get a satisfactory fit for the longer period portion of the amplitude spectra. Then we introduce the  $Q$  values to our calculations. We change the  $Q$  model until we get a good match over the short periods. For event #1 our results show that  $Q_\beta$  values of about 65 for Rayleigh waves and about 75 for Love waves give good matches to the spectra at station SHI. The other path gives a  $Q_\beta$  value of about 75 at station TAB (Figure 7).

Event #2 is also located in the Gulf of Aden (Figure 1). The available spectra for this event are for Rayleigh waves at SHI and for both Love and Rayleigh waves at TAB. The models that give a good fit to the observed spectra have  $Q_\beta$  values between 65 and 70 (Figure 7).

Event #3 is located very close to event #2 (Figure 1). The available records for this event are for Love and Rayleigh waves at SHI and for Rayleigh waves at TAB. Our models for the path to SHI gives  $Q_\beta$  values about 60 and 85, respectively, for Rayleigh and Love waves. For the path to TAB a  $Q_\beta$  value of 60 gives the best match to the observed Rayleigh spectrum (Figure 7).

Event #4 is located in the Red Sea. The available records for this event are for Love and Rayleigh waves at SHI and for Rayleigh waves at JER. These paths cover different areas and their azimuths are also different from the other paths. The results from our modeling give  $Q_\beta$  values of about 100 and 110, respectively, for Rayleigh and Love wave paths to SHI and about 60 for the Rayleigh wave path to JER (Figure 8). As seen from this figure, the spectrum for the path to JER has lost its much higher frequency content. That loss of higher-frequency energy is caused by lower  $Q_\beta$  values for this path. This low  $Q$  value may be associated with partial melting near the axis of the Red Sea spreading center since the path is almost parallel and very close to the ridge axis.

Event #5 was recorded only at station JER. Well-determined Love and Rayleigh wave spectra are, however, available for that station. Since there is only one station record, fault parameters and depth estimation for this event are not

well constrained. Matching the spectra gives a  $Q_\beta$  value about 150 for the upper crust in the central part of the Arabian peninsula (Figure 8).

The results obtained from forward modeling show that crustal  $Q_\beta$  values across the Arabian Peninsula vary between 60 and 150. In the coastal regions  $Q_\beta$  values are smaller than those of inland regions in the peninsula (Figure 9).

#### Predicted $L_g$ Q values.

In order to compare the results obtained in the present study with results obtained by Ghalib (1987), synthetic  $L_g$  waves were generated using the western velocity and Q models. Synthetic  $L_g$  waves were generated for a source at 0.5 km depth and recordings have been obtained from an imaginary station at different distances with an azimuth of  $0^\circ$ . The source parameters for that source are  $30^\circ$  dip,  $30^\circ$  slip, and  $30^\circ$  strike. By assuming that the relation

$$A(r) = A_0 r^{-5.6} e^{-\gamma r} \quad (7)$$

where  $\gamma$  is the attenuation coefficient,  $r$  is epicentral distance, and  $A_0$  is the initial amplitude, it is possible to find  $L_g \gamma$  by measuring the fall-off of  $L_g$  amplitudes with distance (Mitchell and Hwang, 1987). Then  $L_g Q$  is found using

$$Q = \frac{\pi f}{U \gamma} \quad (8)$$

where  $f$  is frequency and  $U$  is group velocity.

In the synthetic  $L_g Q$  calculations,  $U$  was taken to be 3.5 km/s. Calculations give a predicted  $L_g Q$  value of about 237 for this region, a value which is in good agreement with the average observed  $L_g Q$  value of  $230 \pm 50$  obtained by Ghalib (1987).

## DISCUSSION AND CONCLUSIONS

Crustal  $Q_\beta$  values across the Arabian peninsula have been obtained using surface-wave amplitude spectra for both Love and Rayleigh waves. Theoretical amplitude spectra calculated for a Q model consisting of a single layer over a

half-space gives a satisfactory fit to the observed data. The  $Q_\beta$  values obtained here include both intrinsic and scattering effects. Since they are relatively low, however, it is likely that intrinsic effects predominate (Hwang and Mitchell, 1987).

Shear wave velocity models were also obtained from the inversion of Rayleigh and Love wave group velocity dispersion curves. The results from the inversion show that shear velocities are about 2.5-3 km/s in the sediments and increase to 4-4.5 km/s in the deep crust. The results indicate a low-velocity zone in the western part of the peninsula but not in the eastern part. The depth to the top of that low-velocity layer is about 70 km.

Our results pertain to average  $Q_\beta$  values in the upper crust of the Arabian peninsula.  $Q_\beta$  values in the half-space are not determined since this method is not sensitive to  $Q$  values in that depth range. Average upper crustal  $Q_\beta$  values are about 60 in the western coastal region, 100-150 in the central region, and about 60-85 in the eastern region.  $Q_\beta$  values in all parts of the Arabian peninsula are lower than those in other stable regions such as the eastern United States and Canadian shelf. Such low values are normally expected only in areas having undergone relatively recent tectonic activity (Mitchell, 1975; Hwang and Mitchell, 1987).

Bohannon *et al.* (1989) described the development of the western portion of Saudia Arabia as beginning with volcanism and rifting in the Red Sea 30-32 m.y. ago, followed by rotational block faulting and detachment faulting beginning about 25 m.y. ago, and uplift (2.5 - 4.0 km) beginning 13.8 m.y. ago. The low  $Q$  values located in western Saudia Arabia are most likely due to that recent activity. Relatively low values in central Saudia Arabia suggest that the activity near the Red Sea had pervasive effects across much of the peninsula.

The low values (60-85) in the eastern part of the study region are difficult to explain in terms of activity near the Red Sea since it is more than 500 km from the spreading axis. One possibility that slow deformation, which may be

associated with past and current tectonic activity in the Zagros thrust zone, produces those low values. Another possibility is that the low  $Q_\beta$  values there are caused by the thick blanket of sediments which covers the southeastern part of the Arabian peninsula. Total sedimentary thicknesses reach 6000 meters and depths to the base of Mesozoic sediment reach 4500 meters in that region (Brown, 1972). Mitchell and Hwang (1987) showed that young sediments could cause a significant reduction in  $Q$  values for surface waves and  $L_g$  in stable regions.

These  $Q_\beta$  models predict values of  $Q_{L_g}$  which are very close to those ( $230 \pm 50$ ) obtained by Ghalib (1987). This correspondence indicates that  $Q_\beta$  is not only low in this region, but it is very nearly independent of frequency over the period range 1-30 s. If frequency dependence did occur, observed  $L_g$   $Q$  values at 1 Hz would be higher than those predicted by the model obtained from surface waves (Mitchell 1980).



## ACKNOWLEDGMENTS

This research was supported by the Advanced Research Projects Agency of the Department of Defense and monitored by the Geophysics Laboratory under contract F19628-89-K-0021.

## REFERENCES

- Ben-Menahem, A. and Singh, S.J., 1981. Seismic waves and sources. Springer-Verlog Inc., New York, pp.291-300.
- Bohannon, R.G., Naeser, C.W., Schmidt, D.L. and Zimmermann, R.A., 1989. The timing of uplift, and rifting peripheral to the Red Sea: A case for passive rifting? J. Geophys. Res., 94:1683-1701.
- Brown, G.F., 1970. Eastern margin of the Red Sea and the coastal structures in Saudi Arabia. Philos. Trans. R. Soc. London, Ser.A, 267:75-77.
- Brown, G.F., 1972. Tectonic map of the Arabian peninsula,, U.S. Geological Survey.
- Canas, J.A., Correig, A.M., and Mitchell, B.J., 1980.  $Q_\beta^{-1}$  models for the East Pacific rise and the Nazca plate. In: P.A. Davies and S.K. Runcorn (Editors), Mechanics of continental drift and plate tectonics. Academic press, pp.123-133.
- Chan, W.W., Sacks, I.S. and Morrow, R., 1989. Anelasticity of the Iceland Plateau from surface wave analysis. J. Geophys. Res., 94:5675-5688.
- Cheng, C. and Mitchell, B.J., 1981. Crustal Q structure in the United States from multi-mode surface waves. Seism. Soc. Am. Bull., 71:161-181.
- Correig, A.M., Mitchell, B.J. and Ortiz, R., 1990. Seismicity and coda Q values in the eastern Pyrenees: First results from the La Cerdanya network. Pure and Appl. Geophys. 132:311-329.
- Dziewonski, A., Bloch, S. and Landisman, M., 1969. A technique for the analysis of transient seismic signals. Seis. Soc. Am. Bull., 59:427-444.
- El-Isa, Z.H. and Shanti, A.A., 1989. Seismicity and tectonics of the Red Sea and western Arabia. Geophys. J., 97:449-457.

- Fairhead, J.D. and Girdler, R.W., 1970. The seismicity of the Red Sea, Gulf of Aden and Afar triangle. *Phil. Trans. Roy. Soc. Lon., A.* 267:49-74.
- Ghalib, H., 1987. Velocity structures and  $L_g$  attenuation values across the Arabian Peninsula, unpublished paper, St. Louis University, Saint Louis, Missouri.
- Girdler, R. and Styles, R., 1974. Two stage Red Sea floor spreading. *Nature*, 247:7-11.
- Girdler, R. and Underwood, M., 1985. The evolution of early oceanic lithosphere in the southern Red Sea. *Tectonophysics*, 116: 95-108.
- Haskell, N.A., 1963. Radiation pattern of Rayleigh waves from a fault of arbitrary dip and direction of motion in a homogeneous medium. *Bull. Seis. Soc. Am.*, 53:619-642.
- Haskell, N.A., 1964. Radiation patterns of surface waves in a multi-layered medium. *Bull. Seis. Soc. Am.*, 54:377-393.
- Herrin, E. and Goforth, T., 1977. Phase-matched filters: Application to the study of Rayleigh waves. *Bull. Seis. Soc. Am.*, 67:1259-1275.
- Hwang, H.G. and Mitchell, B.J., 1987. Shear velocities,  $Q_\beta$ , and the frequency independence of  $Q_\beta$  in stable and tectonically active regions from surface wave observations. *Geophys. J.R. astr. Soc.*, 90:575,613.
- Knopoff, L. and Fouda, A.A., 1975. Upper-mantle structure under the Arabian Peninsula. *Tectonophysics*, 26:121-134.
- Lawson, C.L. and Hanson, R.J., 1974. Solving least squares problems. Prentice-Hall Inc., Englewood cliffs, New Jersey.
- McKenzie, D.P., 1972. Active tectonics of the Mediterranean region. *Geophys. J. Roy. Ast. Soc.*, 30:109-185.

- Mitchell, B.J., 1973. Radiation and attenuation of Rayleigh waves from the southeastern Missouri earthquake of October 21, 1965. *J. Geophys. Res.*, 78:886-899.
- Mitchell, B.J., 1975. Regional Rayleigh wave attenuation in North America, *J. Geophys. Res.*, 80: 4904-4916.
- Mitchell, B.J., 1980. Frequency dependence of shear wave internal friction in the continental crust of eastern North America. *J. Geophys. Res.* 85:5212-5218.
- Mitchell, B.J. and Hwang, H.G., 1987. Effect of low Q sediments and crustal Q on Lg attenuation in the United States. *Bull. Seis. Soc. Am.*, 77:1197-1210.
- Mokhtar, T.A., 1987. Seismic velocity and Q models for the shallow structure of the Arabian Shield from short period Rayleigh Waves. Ph.D. Thesis, Saint Louis University, St.Louis, Missouri, 167 pp.
- Mooney, W.D., Gettings, M.E., Blank, H.R. and Healy, J.H., 1985. Saudi Arabian seismic deep-refraction profile. A travel time interpretation of deep crustal structure. *Tectonophysics*, 111:173-246.
- Niazi, M., 1968. Crustal thickness in the Central Saudi Arabian Peninsula. *Geophys. J. R. Astr. Soc.*, 15:545-547.
- Pacheco, J. and Nabelek, J., 1988. Source mechanisms of three moderate California Earthquakes of July 1986. *Seism. Soc. Am. Bull.*, 78:1907-1929.
- Tsai, Y.B. and Aki, K., 1969. Simultaneous determination of seismic moment and attenuation of surface waves. *Bull Seism. Soc. Am. Bull.*, 59:275-287.
- Tsai, Y.B. and Aki, A., 1970. Precise focal depth determination from amplitude spectra of surface waves. *J. Geophys. Res.*, 75:5729-5743.
- Tsai, Y.B. and Aki, K., 1971. Amplitude spectra of surface waves from small earthquakes and underground nuclear explosions. *J. Geophys. Res.*, 76:3940-3952.

Wang, C.Y., 1981. Wave theory for seismogram synthesis. Ph.D. Thesis, Saint Louis University, St. Louis, Missouri, 235 pp.

Table 1. Earthquake source parameters.

Event	Date	Lat.	Lon.	Ori. time	Depth	Mag.(Ms)	Dip	Slip	Strike
#1	02/28/77	14.78	54.94	08:43:55.6	6 km	4.9	70	-105	270
#2	12/17/77	13.19	51.01	23:57:55.0	4 km	5.0 Mb	80	-85	280
#3	02/11/78	13.20	50.98	12:54:18.0	9 km	5.3	65	-115	290
#4	01/17/78	16.52	40.28	15:00:31.0	3 km	5.3	50	170	5
#5	01/28/84	13.96	51.74	22:47:50.8	7 km	5.3	70	150	150

## Figure Captions

**Figure 1.** Tectonic units (After Knopoff and Fauda, 1975), location of the earthquakes and stations, and path coverage in the Arabian peninsula.

**Figure 2.** Western peninsula dispersion curves and shear velocity model. The solid squares are observed velocities. The solid lines are theoretical dispersion curves. Resolving kernels for selected depths are given below the velocity model.

**Figure 3.** Eastern peninsula dispersion curves and shear velocity model. The solid squares are observed velocities. The solid lines are theoretical dispersion curves. Resolving kernels for selected depths are given below the velocity model.

**Figure 4.** Amplitude spectra of Love waves and Rayleigh waves calculated for various source depths (left) and source durations (right).

**Figure 5.** Amplitude spectra of Love and Rayleigh waves calculated for various dip values (left), strike values (center), and slip values (right).

**Figure 6.** Amplitude spectra of Love and Rayleigh waves calculated for various values of  $Q_\beta$  at depths greater than 20 km (left), and at depths less than 20 km (right).

**Figure 7.** Theoretical and observed amplitude spectra at SHI and TAB for event 1 (top), event 2 (center), and event 3 (bottom). The solid circles are observed spectral values and the solid lines are the theoretical amplitude spectra calculated for a single layer over a half space model. The broken lines are the theoretical amplitude spectra calculated for upper crustal  $Q_\beta$  values which are greater than,

and less than, the derived value by 20.

**Figure 8.** Theoretical and observed amplitude spectra at stations SHI and JER for event 4 (upper) and event 5 (lower). See the caption of Figure 7 for explanations of the symbols.

**Figure 9.**  $Q_\beta$  values in the upper crust of the Arabian peninsula.



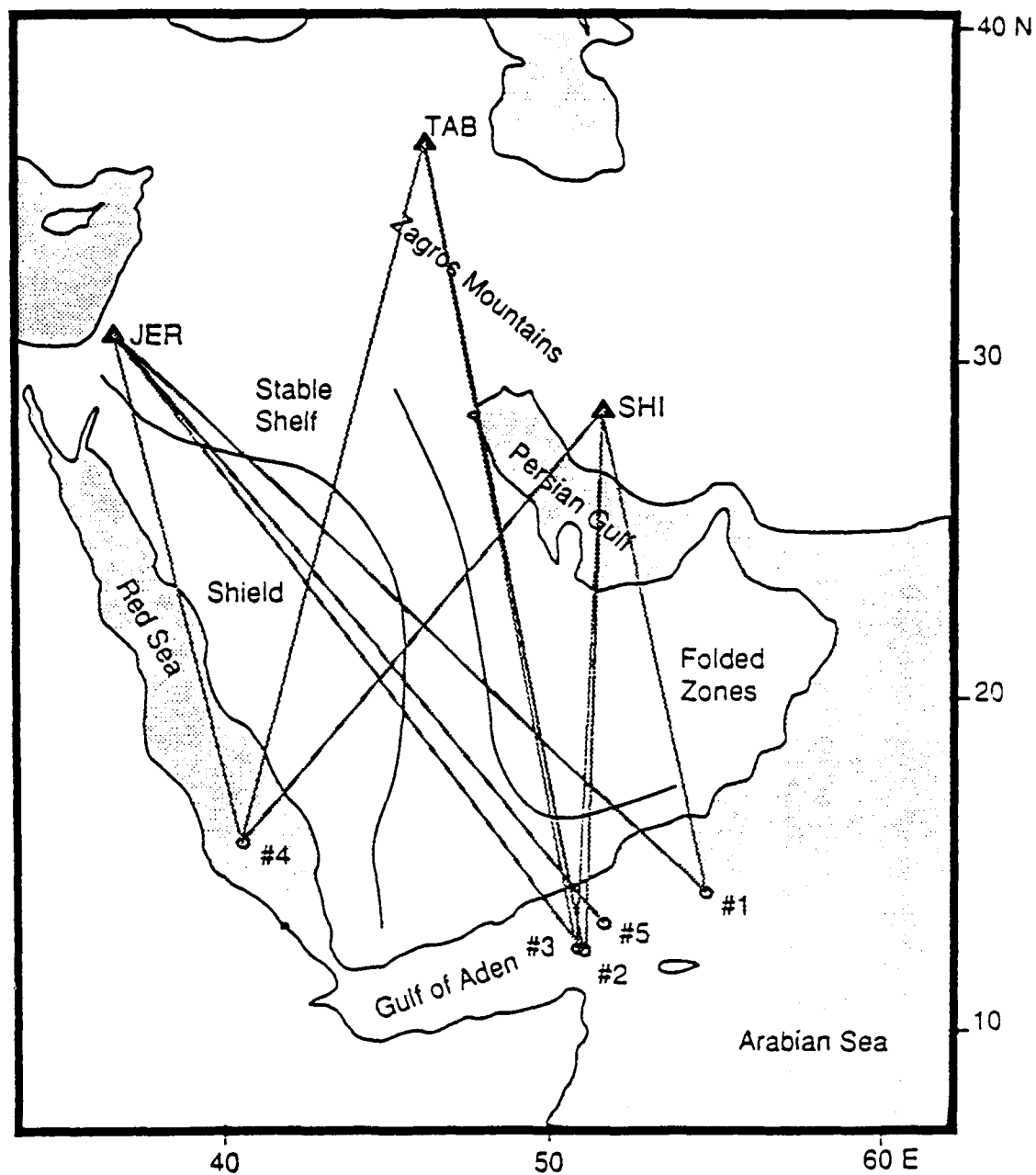


Figure 1

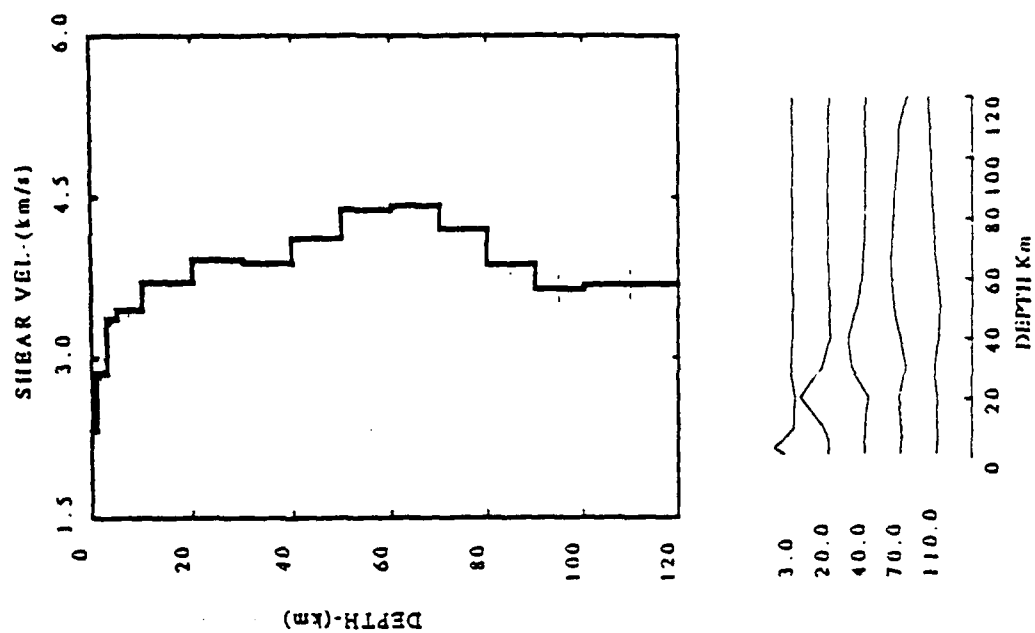
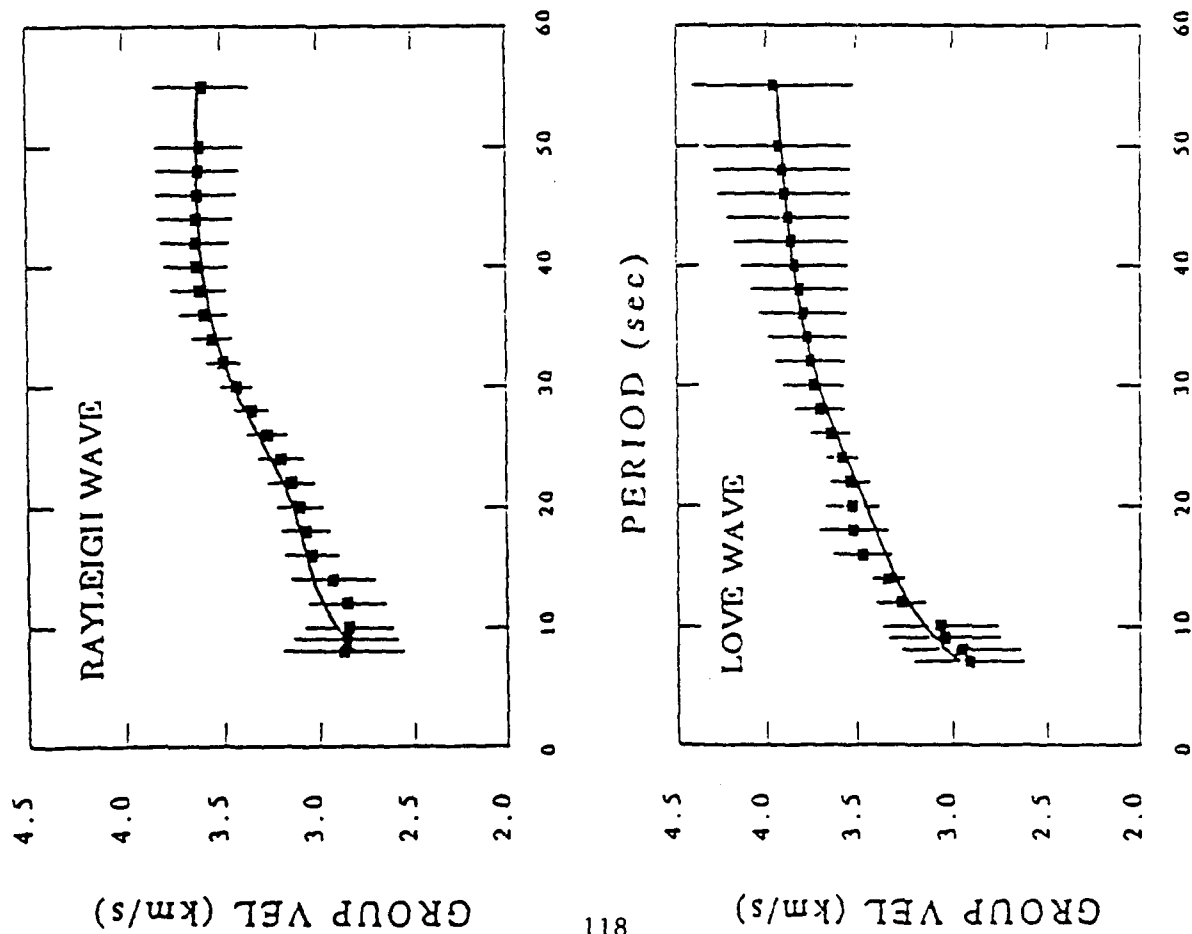


Figure 2

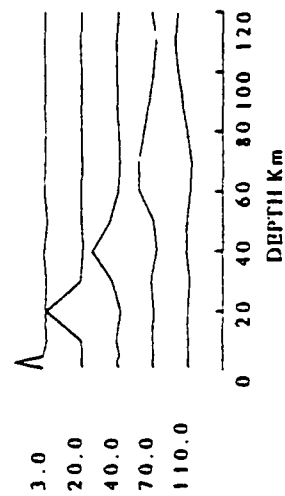
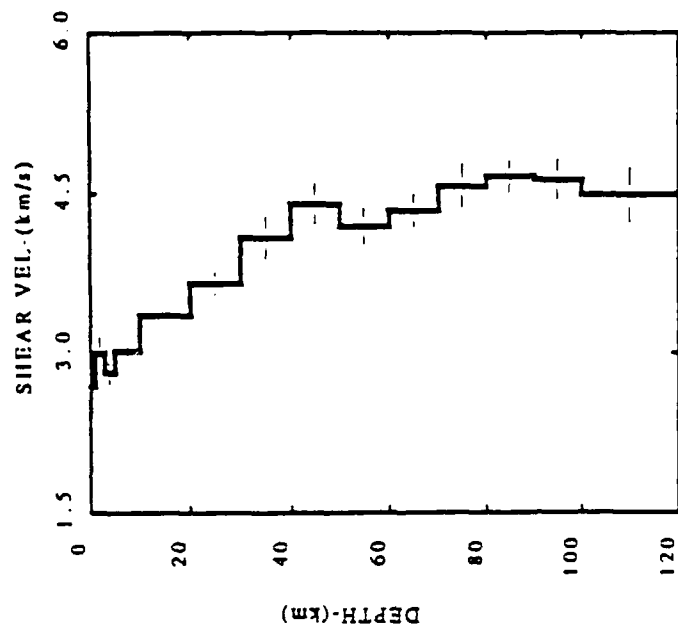
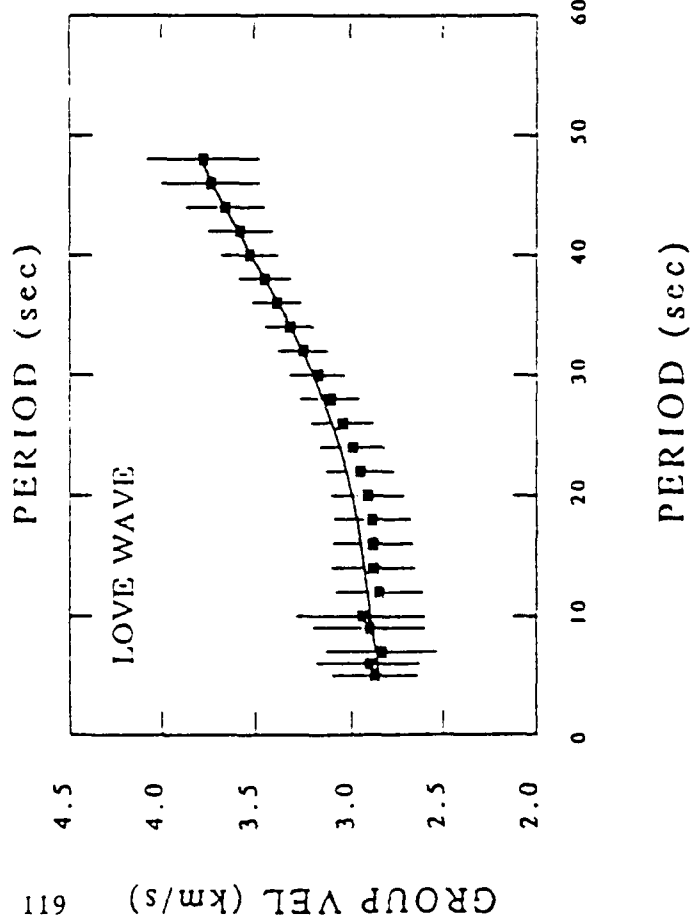
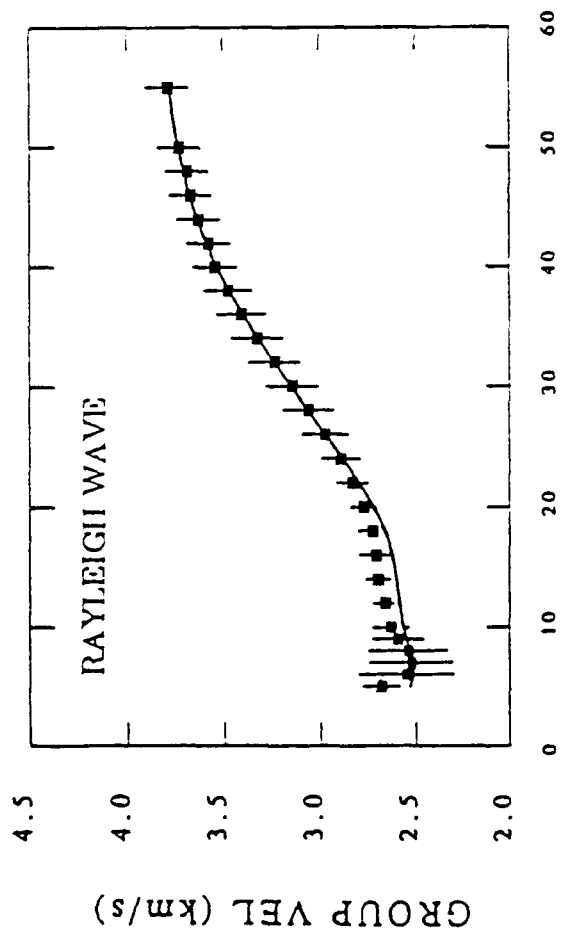


Figure 3

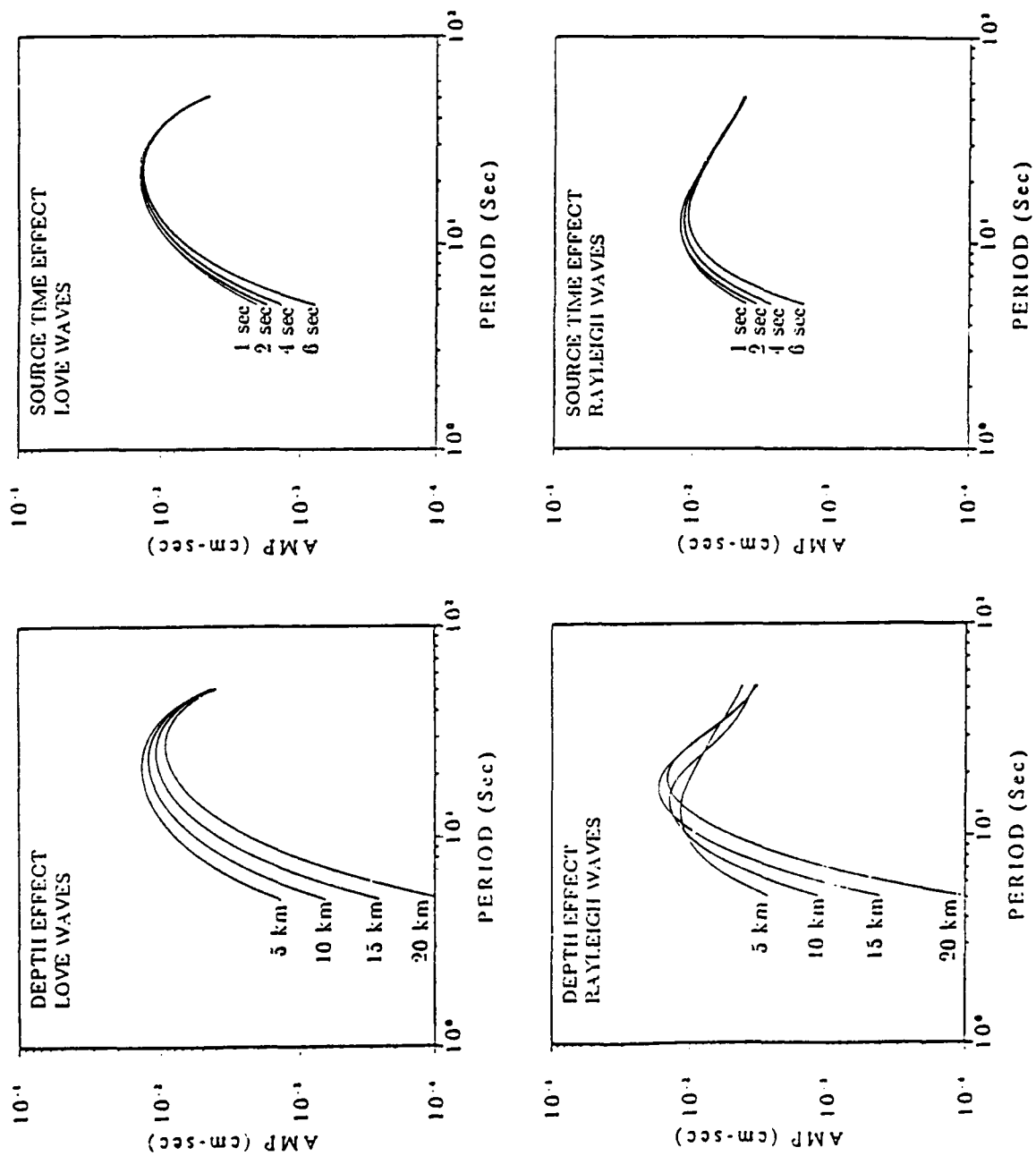


Figure 4

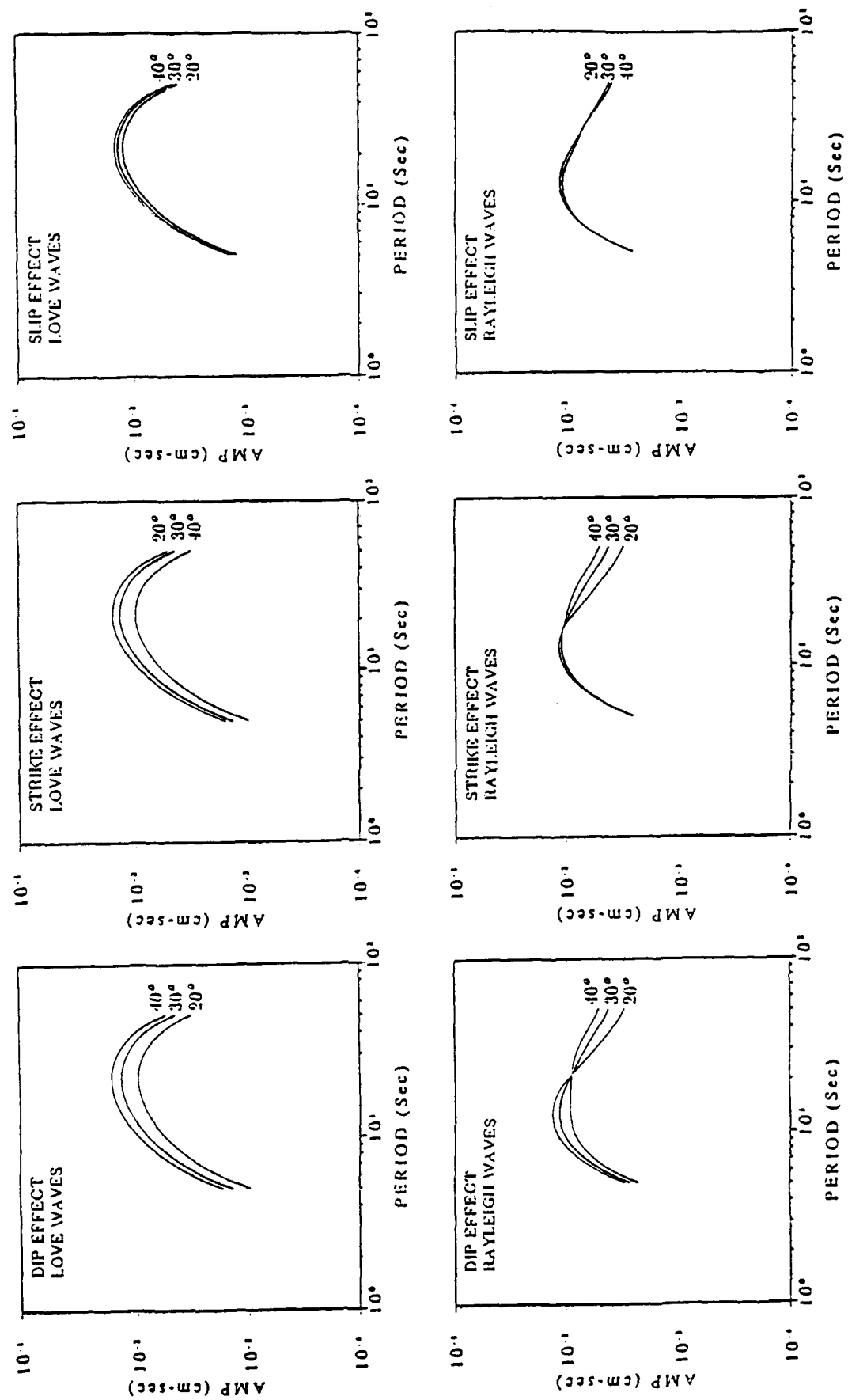


Figure 5

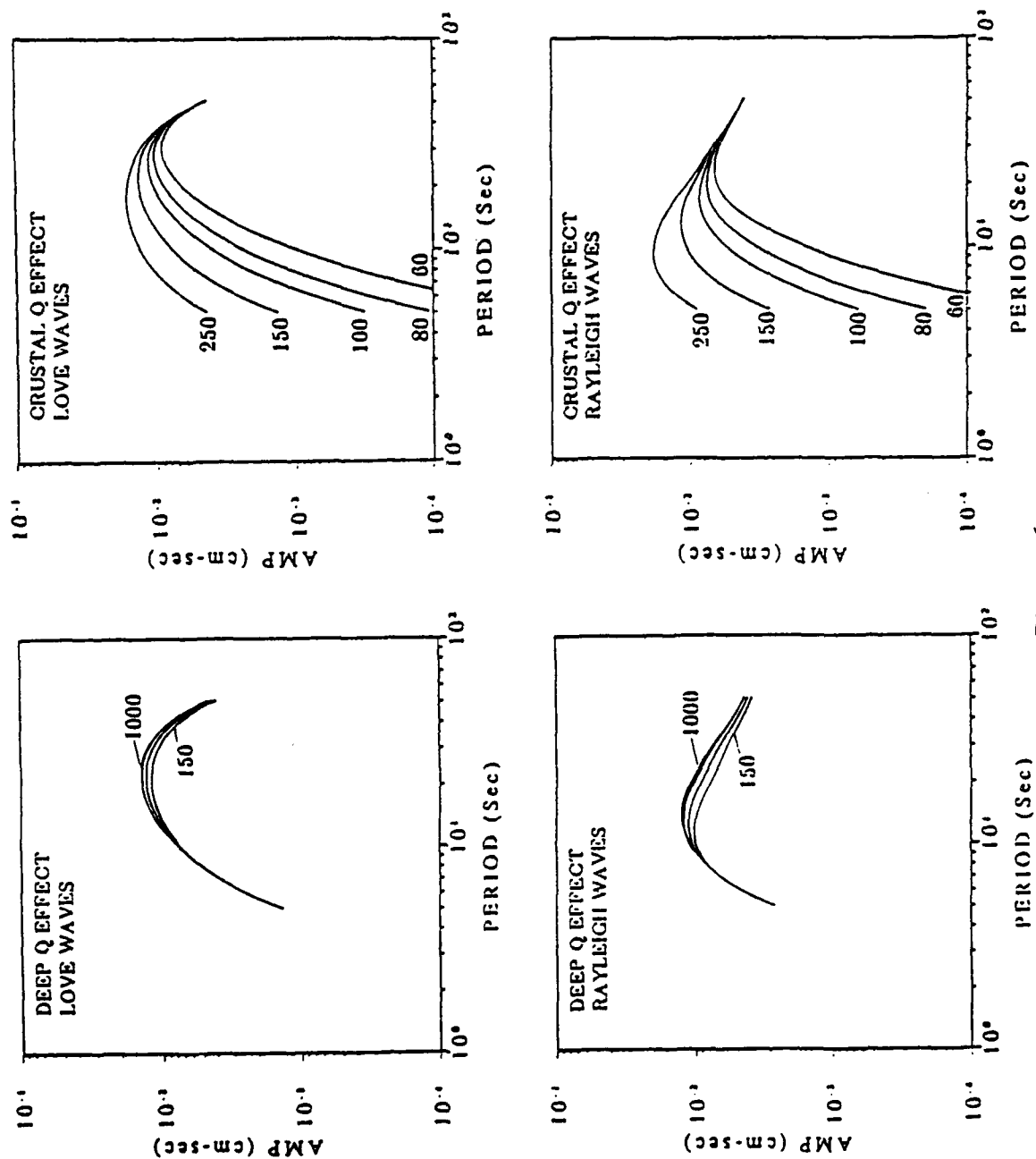


Figure 6

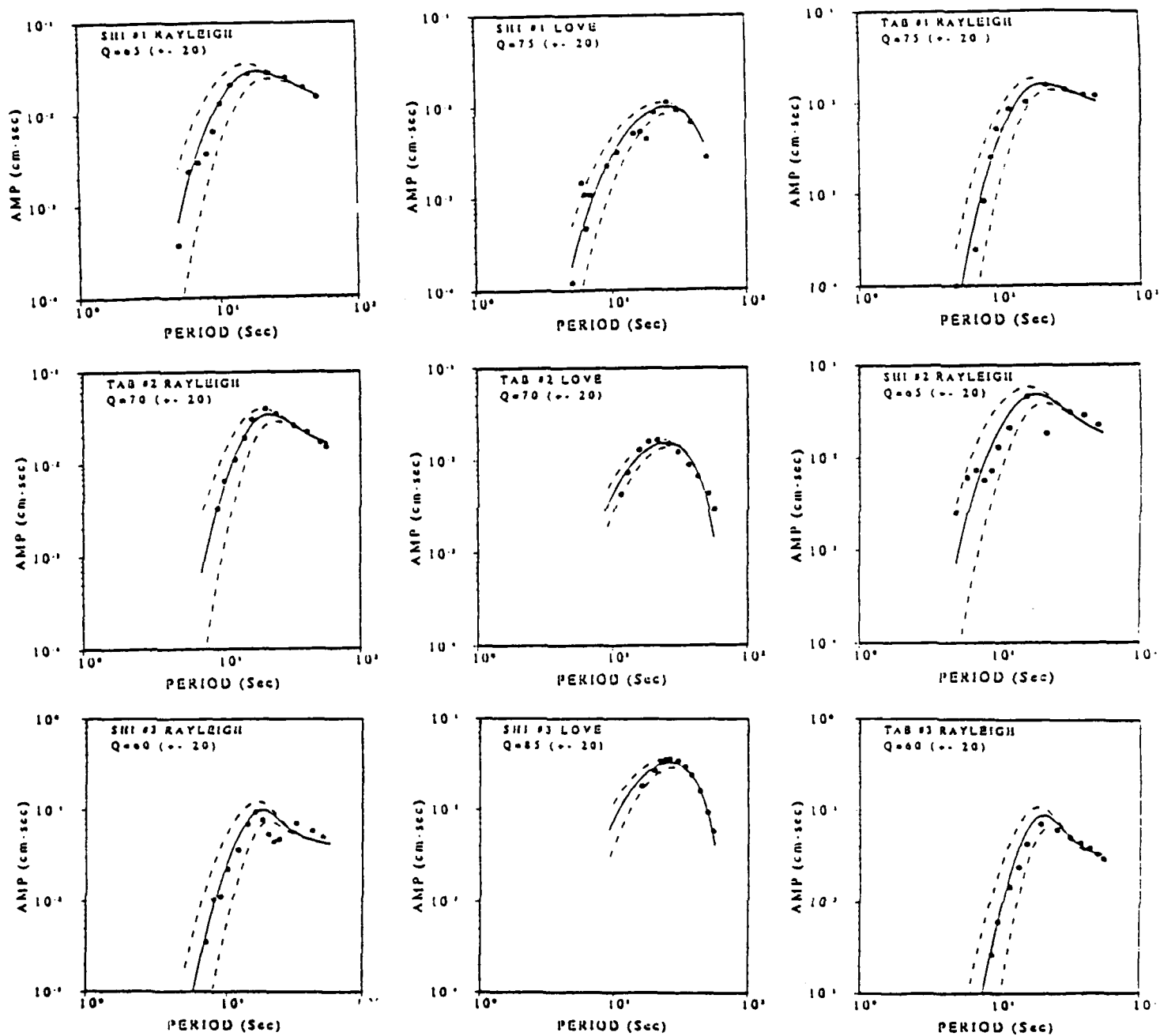


Figure 7

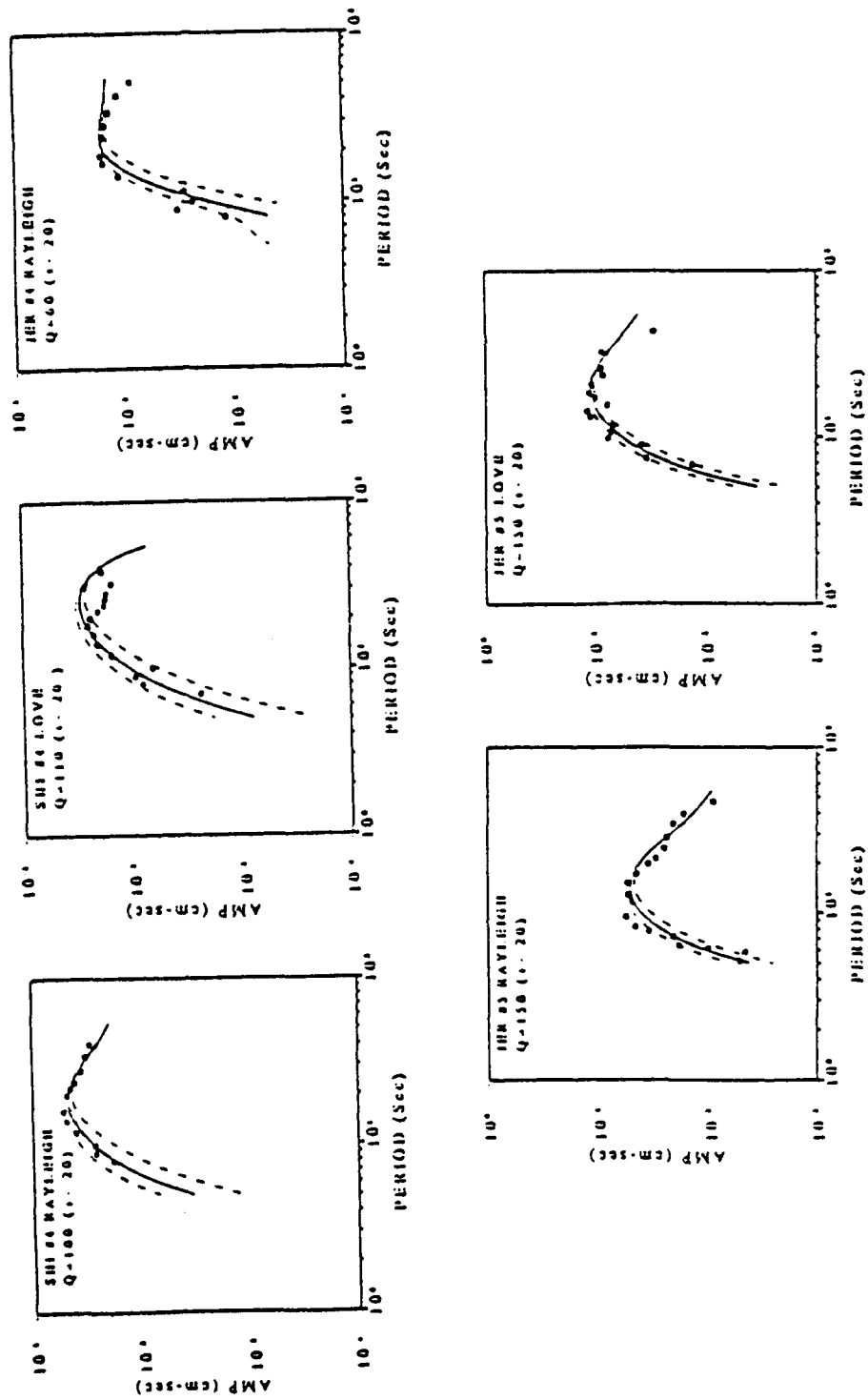


Figure 8



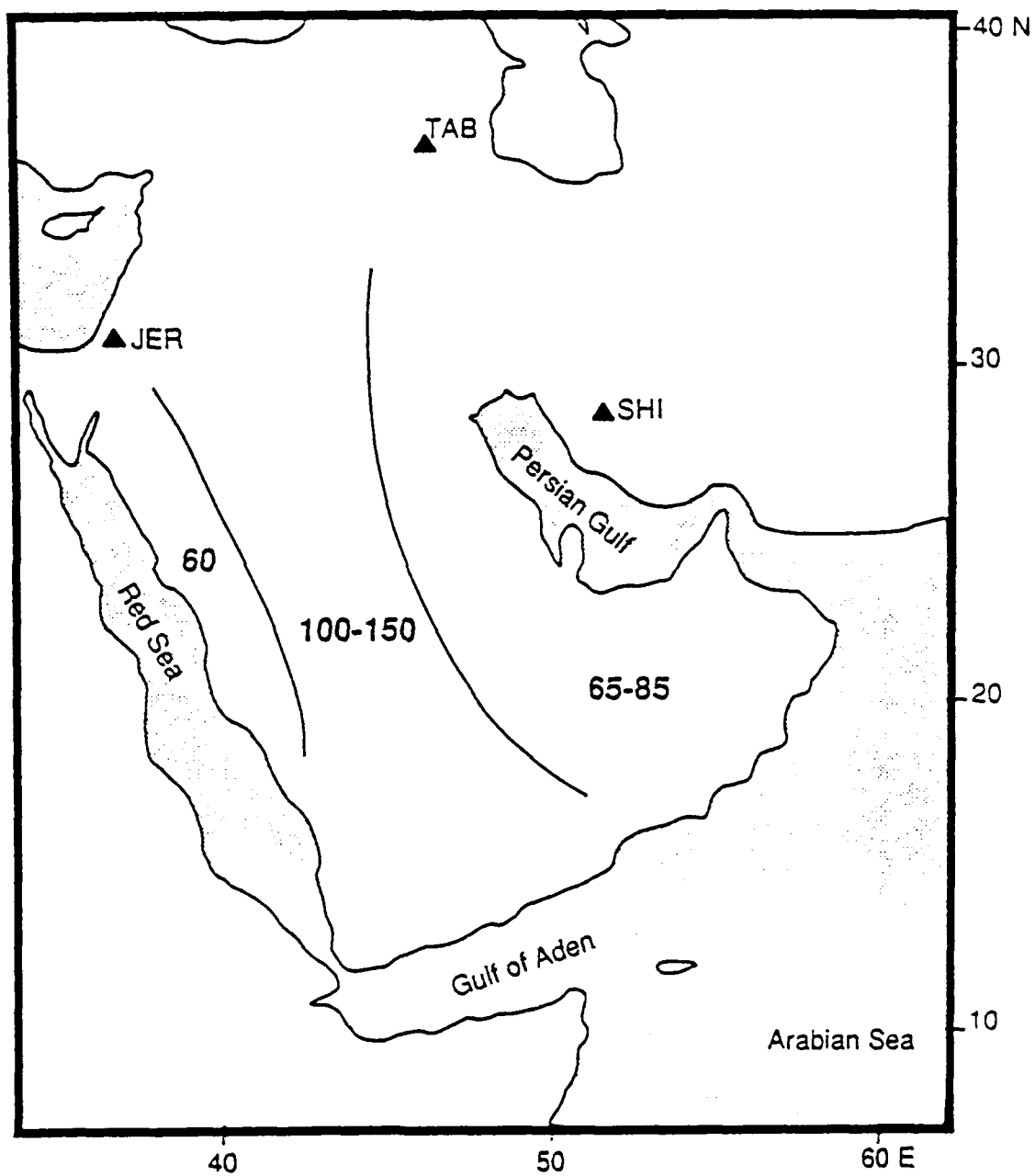


Figure 9

## **Chapter 5**

**Learned Estimation of Focal Depths with  
Multilayered Neural Networks: Application  
to Continental and Oceanic Earthquakes**

**by**

**Gagan B. Patnaik, Dogan Seber and Brian J. Mitchell**

## ABSTRACT

A novel technique based upon neural network learning has been applied to the estimation of earthquake focal depths from observed amplitude spectral ratios of surface waves. The network learning exploits mapping relationships between the spectral ratios of fundamental-mode synthetic Love to Rayleigh wave spectra and corresponding source depths. On a partially trained network with a continental velocity model, 4608 noise-free synthetic spectral ratios corresponding to various source orientations were consistently classified into 8 preassigned focal depth groups with over 80% accuracy when the networks were simulated with varying numbers of hidden layers and varying numbers of processing units in each layer. With this satisfactory performance of trained neural networks on synthetic spectra, well-calibrated events from eastern North America were processed and the corresponding focal depths were estimated. The events studied in this paper were the New Brunswick earthquake of 09 Jan 1982 and three of its aftershocks. The data for all events of the New Brunswick sequence were retrieved from GDSN stations within continental North America (ALQ, ANMO, JAS, LON). Phase-matched filtered fundamental-mode surface wave signals were extracted for the construction of spectral ratios. Focal depths obtained in all cases were consistent with those reported by others.

A second neural network with a different architecture was trained using spectral ratios computed from an oceanic velocity model derived from the inversion of surface wave dispersion across the southeast Indian Ocean for focal depth estimation of oceanic events. The network, after partial training with 3240 synthetic spectral ratios, classified them into 5 preassigned focal depth groups with over 90% accuracy. Two events which occurred on the southern Indian Ocean were chosen for testing. The depth of one of the events agreed within  $\pm 2.5$  km of the reported centroid depth as well as the ISC reported depth from body wave phases (pP - P). The estimated depth of the other event also agreed with the depths assumed for that region by the NEIS. Since the synthetic spectral ratios were noise-free, a noise tolerance test was also performed using a subset (300) of the spectral ratios generated with the oceanic model. Upon training and

testing at various noise levels it was observed that even with 40% noise added to the spectral ratios (a S/N degradation of 8dB), the network was still able to classify the spectral ratios into 3 preassigned depth groups at nearly the 70% level. The noise tolerance test implied that it might even be possible to use observed spectral ratios with low signal-to-noise for depth estimation. Further testing with many observations will be necessary to determine whether or not this will be possible.

## Introduction

Recent developments in the field of neural computing have provided efficient non-linear transfer function approximation mechanisms (e.g., Rumelhart, *et al.* 1986; Clark, 1988; Moody and Darken, 1989) that can be applied to many seismological problems. Neural computing may also be viewed as a decision-making process where a neural network is trained to identify the class which may best represent an input pattern. This, in turn, requires that a network has already been adapted to recognizing such classes, by means of *learning* earlier examples. The learning can essentially be viewed as a non-linear system modeling process. It so happens that these networks, in some restricted sense, are capable of performing certain low-level tasks such as, combining numerical information and pattern recognition. Solutions to the problem of the present study, focal depth estimation, are sought by exploiting this capability of neural networks.

The depth dependence of surface wave amplitude spectra has been well studied, (e.g., Toksoz *et al.*, 1964; Harkrider, 1964,1970; Tsai and Aki, 1970,1971; Masse *et al.*, 1973; Herrmann, 1979; Yan and Alexander, 1990). The underlying principle can be described as follows. There is a strong dependence of observed surface Rayleigh wave amplitude spectra on the depth of the source for many focal mechanisms. The spectral holes of fundamental-mode Rayleigh waves shift towards lower frequencies as the focal depth increases. In addition, the high-frequency spectrum of Love and Rayleigh waves attenuate as the depth increases and the slope of the spectrum becomes steeper with decreasing cut-off frequency. There is also a strong azimuthal dependence of the spectrum for a given source mechanism. These facts have been used in the past to estimate the source parameters of shallow events.

The aim of this study is to estimate focal depths from observed surface wave amplitude spectral ratios by processing those ratios through a neural network that has been *a priori* adapted to learn the nonlinear functional relationship that may exist among the spectral ratios (input), source-crustal response and source mechanisms (system), and the focal depths (output). By using Love to Rayleigh wave spectral ratios, we effectively cancel out attenuation factors (geometrical spreading and anelasticity). Incorporating a well-constrained source-crustal model response and combinations of source mechanisms into the neural network learning process, variations in the spectral ratios can be attributed to changes in source depths.

In the following sections we present brief introductions to neural computing, depth estimation from surface wave amplitude spectral ratios, and preprocessing methods applied to the observed data. We then apply the present technique to four events of New Brunswick sequence and two events in the Indian Ocean with reported focal depths.

## Neural Computing

Detailed theoretical developments of neural networks have been presented by many researchers, primarily in the fields of electrical engineering, physics, biology and computer sciences (e.g., Hopfield, 1982; Hopfield and Tank, 1985; Rumelhart and McClelland, 1986; Sejnowski *et al.*, 1986; Takeda and Goodman, 1986; Lippmann, 1987; Peterson and Anderson, 1987). A neural network is shown in Figure 1. It consists of  $<N>$  layers, each containing  $S[i]$  nonlinear processors (neurons),  $i = 1, \dots, n$ . Successive layers are fully interconnected in the forward direction (feed-forward). This architecture is computationally complete (Lippmann, 1987) in the sense that any arbitrary classification boundary can be approximated with this topology. Each processor acts as a thresholding unit, turning "on" or "off" depending on whether or not the sum of its inputs exceeds a threshold value. This output of a processor becomes an input to the other processors after being multiplied by a set of interconnection weights. Determination of the appropriate interconnection weights (strengths) among all the processors such that the dynamic system as a whole (the network) produces a desirable output constitutes the network *learning*. In general, when a network has *learned*, an energy functional has been minimized, and the matrix representing the interconnection topology yields a *trained* neural network. This can be achieved using a numerical iterative procedure, by solving a system of stiff ordinary differential equations representing the network dynamics.

In our case a network *learns* the given spectral ratio inputs and the corresponding focal depth outputs in a *best match* sense and the heart of this learning is an iterative nonlinear optimization process where a large number of *weak* constraints are simultaneously satisfied. The underlying nonlinear system which is modeled is the layered-medium response to the matching of given spectral ratios and corresponding focal depths. There are several ways that a neural network can be trained. The following paragraphs describe two of those which are used in this study.

### *The Back-Error-Propagation Learning Algorithm*

This is a recently developed, effective learning algorithm for the multi-layer neural network (multilayer perceptron) shown in Figure 1. Following Rumelhart and McClelland (1986), and Khotanazad and Lu (1990), learning can be accomplished by the optimization of a criterion function, where constraint satisfaction can be achieved by

estimating the discrepancy between the desired and actual output values, feeding back an error signal layer by layer to the inputs, and then adjusting the interconnection weights in such ways as to modify them in proportion to their contribution to the total mean-square-error. This is computationally the fastest deterministic algorithm; however, it is also the most susceptible to *local minima* problems. Following Khotanazad and Lu (1990), this learning procedure can be briefly described as follows. The connection weights  $W_{ij}$  are initialized to small random values. A feature vector (spectral ratio) is fed forward through the multilayer neural network. Then the output of processor (neuron)  $j$  which is a nonlinear sigmoidal over its total input becomes,

$$S_j = \text{sig}(\sum_i W_{ij} S_i + \theta_j) = \frac{1}{1 + e^{-\sum_i W_{ij} S_i + \theta_j}} \quad (1)$$

In (1),  $S_i$  is the output of the  $i^{\text{th}}$  neuron in a previous layer. The function  $\text{sig}(x)$  is of the form of  $\tanh$  or of a *modified Heaviside* function.  $W_{ij}$  and  $\theta_j$  are interconnection weights and thresholds, respectively. The squashing function  $\text{sig}(x)$  with a sigmoidal shape controls the nonlinear behavior of each processor. Next, an error term  $\delta_j$  for a processor at the output layer is computed. That term is given by

$$\delta_j = (O_j - S_j) S_j (1 - S_j) \quad (2)$$

where  $O_j$  is the desired output controlled by an *a priori* teaching signal, and  $S_j$  is a neural output. Similarly, using the chain-rule of differentiation, the error term for a hidden layer processor is computed,

$$\delta_j = S_j(1 - S_j) \sum_k \delta_k W_{jk} \quad (3)$$

where  $k$  runs over all processors in the layer above processor  $j$ . Finally, the connections are adjusted by using,

$$W_{ij}^{\text{new}} = W_{ij}^{\text{current}} + \eta \delta_j S_i + \alpha (W_{ij}^{\text{current}} - W_{ij}^{\text{old}}). \quad (4)$$

The parameter  $\eta$  is a learning rate similar to step size in gradient search algorithms, and  $\alpha$  is a constant that reflects the effect of past weight changes. The latter is somewhat similar to *momentum*, a parameter that effectively filters out high-frequency variations of an error surface and helps avoid local minima. Thus, in (4) not only the gradient, but also the previous change in interconnections has been used to adjust the connection vectors. This is analogous to a second-order dynamic system that has better convergence properties than a first-order system (gradient descent without  $\alpha$  term in (4)).

All training input vectors are presented either cyclically or randomly to the neural network, errors are propagated backwards and the cycles are continued until the connection matrix stabilizes. The nonlinear squashing function used in each processor may

be replaced by other simpler ones (e.g., linear or piece-wise linear functions), if the feature space is simple. This would effectively speed up the learning process. In our simulations, however, all the processors have a sigmoidal threshold.

### *Statistical Mechanics Analogy*

In neural network learning processes constraint satisfaction is achieved through large scale nonlinear optimization such that, either a functional describing the goodness of fit is maximized, or equivalently, a functional describing the energy of a dynamical system (state of the network) is minimized. The other learning algorithm, Mean Field Theory, used in this study, utilizes this energy minimization criteria from a statistical physics perspective. The main advantage of this over other deterministic procedures is its ability to overcome the problem of *local minima*. In a physical system the tendency is always to evolve from highly energetic states to states of minimal energy. From this perspective the neural network dynamics may completely be described as thermodynamical systems that seek stable minimum energy states, or *attractor* states (Hopfield, 1982, 1985). Many recent investigations (e.g., Moussouris, 1974; Choi and Huberman, 1983; Geman and Geman, 1984; Sejnowski, *et al.* 1986; Sompolinsky, 1988; and Clark, 1988), report exhaustive analytical descriptions of neural networks through *attractor dynamics* and study their behavior as deterministic chaotic. Most of these studies are of theoretical importance and we will restrict ourselves to only application-oriented analyses.

Since constraint satisfaction is an energy minimization problem, an analogy may be drawn to metal *annealing* processes, which involve heating the material and then cooling it very slowly, so that the temperature settles gradually and the material at molecular level coalesces, giving rise to a global energy minimum. Hence, the idea of *simulated annealing* of a dynamical system to bring it to a stable state which, in turn, yields the appropriate global solution. In practice, it is done through a probabilistic update rule,

$$P \left[ S_i(t)=1 \right] = \frac{1}{1+e^{-net_i/T}} \quad (5)$$

where  $T$  is a global *temperature* parameter and the term  $net_i$  corresponds to (1). In this case, the processors may become continuous, depending upon the probability distribution in (5) and the system as a whole becomes stochastic.

### *The Mean-Field-Theory Learning Algorithm*

Mean Field Theory (MFT) approximation is a well known technique in spin-systems (e.g., Glauber, 1963). Peterson and Anderson (1987) have improved an earlier non-deterministic learning algorithm (the Boltzmann Machine) using this approximation such that the solutions to a set of deterministic equations could be used to describe the dynamic state of a network. The application of MFT to neural network learning results

in a statistical mechanical system that uses a simulated annealing relaxation technique to search for the best possible connection weights (globally minimum energy) over a large solution space.

An energy functional may be written as,

$$E(S) = -\frac{1}{2} \sum_{i,j=0}^{N+h} W_{ij} S_i S_j \quad (6)$$

where  $S = (S_1, \dots, S_i, \dots, S_N)$  describes a state of the network,  $W_{ij}$  are interconnection weights,  $h$  is the number of hidden processors, and  $S_{i,j}$  are binary valued processors (neurons). Differentiating (6) with respect to  $S_i$  and noting the symmetric coupling,  $W_{ij} = W_{ji}$ , the system can be made to relax to a local energy minima with a step function updating rule,

$$\begin{aligned} S_i &= +1 ; \sum_j W_{ij} S_j > 0 \\ &= -1 ; \sum_j W_{ij} S_j < 0. \end{aligned} \quad (7)$$

The simulated annealing technique is applied, in practice, to avoid any local minima and the relaxation is done according to the Boltzmann distribution,

$$P(S) \propto e^{-E(S)/T} \quad (8)$$

where  $P(S)$  is the probability that the state  $S$  will occur given the temperature  $T$ .

Peterson and Anderson (1987) derived an average of a network state function in (8) as,

$$\langle F(S) \rangle = \frac{1}{Z} \sum_S F(S) e^{-E(S)/T} \quad (9)$$

where  $Z$  is the so-called partition function,

$$Z = \sum_S e^{-E(S)/T}. \quad (10)$$

The summation is taken over all the processor configurations, therefore, the sum over the binary processor,  $S = \pm 1$  in (7), can be replaced by an integral over continuous mean field variables. With further reductions the solutions to the neural network represented in (6) may be written in their final form as

$$S_j = \tanh(\sum_i W_{ij} S_i / T). \quad (11)$$

Note that the unit step function approximation used in (7) is now replaced by a sigmoidal updating rule. The algorithms based on (11) are deterministic and can be solved iteratively by



$$S_i^{\text{new}} = \tanh(\sum_j W_{ij} S_j^{\text{old}} / T). \quad (12)$$

In brief, each spectral ratio (feature vector) is passed through two phases (clamped and free running) each with an annealing schedule. Statistics are collected at the end of each phase and the interconnection weights are updated. The steps are repeated until no more changes in  $W_{ij}$  take place.

Both learning algorithms, the back-error-propagation and the mean-field-theory, have been used in the present study.

### Spectral Ratios

Following Haskell (1964) and Harkrider (1964, 1970), the spectral far-field surface displacements for Love and Rayleigh waves due to a double-couple source in a layered earth may be written as,

$$U = S k^m e^{-i(1+2m)\pi/4} \chi(\theta, h) E e^{-ikr} r^{-1/2} \quad (13)$$

where  $S$  is the spectral source function,  $k$  is the angular wave number ( $k=\omega/c$ ),  $\chi$  is the source radiation pattern,  $h$  is the source depth,  $\theta$  is the azimuth from source to station, and  $r$  is the epicentral distance. (13) may be separated into Love and Rayleigh component displacements as

$$U_L = S k_L e^{-i3\pi/4} \chi_L(\theta, h) E_L D_L(k_L, r) \quad (14)$$

and

$$U_R = S k_R e^{-i3\pi/4} \chi_R(\theta, h) E_R D_R(k_R, r). \quad (15)$$

where  $D_{L,R}(k, r)$  represents attenuation effects. This follows from the fact that in (13),  $m=1$  for a double-couple source. The quantities  $E_L$  and  $E_R$  can be determined from the amplitude responses,  $\Delta_{L,R}$ , the wave numbers,  $k_{L,R}$ , and the Rayleigh wave ellipticity,  $\epsilon_0$ , using  $E_L = \Delta_L k_L^{-1/2}$  and  $E_R = \epsilon_0 \Delta_R k_R^{-1/4}$ .  $D_{L,R}(k, r)$  can be written as

$$D_{L,R}(k, r) = r^{-1/2} e^{-ik_{L,R}r} e^{\frac{-\pi fr}{Q_{L,R}U_{L,R}}}$$

which includes attenuation due to both geometrical spreading and anelasticity.  $Q_{L,R}$  in this equation represents the quality factor for either Love and Rayleigh waves, and  $U_{L,R}$  is the corresponding wave group velocity. Since we are interested in spectral ratios of Love to Rayleigh waves, with the assumption that the attenuation coefficients for both these waves are approximately the same for the frequency range of observable continental dispersion (e.g., Tsai and Aki, 1970; Yan and Alexander, 1990), the ratio

$D_L(k_L, r)/D_R(k_R, r)$  is very close to 1, *i.e.*, the terms involving attenuation and geometrical spreading cancel out. The quantity in (13) that remains to be defined is the complex radiation pattern function given by

$$\chi(\theta, h) = d_0 + i(d_1 \sin \theta + d_2 \cos \theta) + d_3 \sin 2\theta + d_4 \cos 2\theta. \quad (16)$$

The coefficients  $d_i$ , as given in Harkrider (1970), may be expressed in terms of Thomson-Haskell displacement-stress vector elements (Haskell, 1953).  $\chi(\theta, h)$  are functions of source depth ( $h$ ), dip ( $\delta$ ) and slip ( $\lambda$ ) of the fault plane, and the azimuth ( $\theta$ ).

The amplitude responses,  $\Delta_L$  and  $\Delta_R$ , and hence the quantities  $E_L$  and  $E_R$ , are functions of frequency, mode order and the elastic properties of the layered medium and are independent of source geometry and depth. The term  $S$  in (13) is the source-time-space function (Harkrider, 1970) and will depend on fault displacement, fault dimensions, and rupture velocity. For smaller sources, with magnitudes less than 6.0, the assumption of non-propagating point source may be valid. Therefore, ignoring the source finiteness,  $S$  becomes the same for both Love and Rayleigh waves and will cancel out in the ratios for periods greater than 10 seconds. Taking the ratio between (14) and (15) we get,

$$\left| \frac{U_L}{U_R} \right| = \left| \frac{k_L}{k_R} \frac{\chi_L(\theta, h, \lambda, \delta)}{\chi_R(\theta, h, \lambda, \delta)} \frac{E_L}{E_R} \right|. \quad (17)$$

The first and last quantities on the right-hand-side of (17) are model dependent whereas, the complex radiation pattern terms are dependent on source-crustal model, the source geometry, and the source depth. This formulation has been used by many for source mechanism and source depth estimation (*e.g.* Harkrider, 1970; Masse *et al.*, 1973; Herrmann, 1979; Yan and Alexander, 1990). In the present study we also use (17) to construct the fundamental-mode surface wave spectral ratios.

## Data Processing

It is well known that observed surface wave modes are frequently contaminated by both random and coherent noise due to multipathing and higher-mode interference. Therefore, a direct Fourier amplitude spectrum of the observed signal is not a true representation of the fundamental-mode surface wave spectrum. There are many techniques available for the isolation of the pure fundamental-mode (or any higher mode) spectrum. The phase-matched filtering method has been used by many researchers (*e.g.*, Herrin and Goforth, 1977; Goforth and Herrin, 1979; Russell, 1987) for surface wave studies. This method essentially involves compression of energy in the time domain so that a zero-phase signal with energy concentrated about zero-lag results. The resulting signal with no phase is equivalent to a time-domain pseudo-autocorrelation

function. Then by time-windowing the pseudo-autocorrelation function,  $\psi(t)$ , with a symmetric, zero-phase window,  $w(t)$ , and taking a Fourier transform, the desired signal spectrum is isolated from other modes and noises. The amplitude spectrum of the pseudo-autocorrelation function may be written as,

$$Ae^{i\delta kx} = \int_{-\infty}^{\infty} \psi(t) w(t) e^{-i\omega t} dt \quad (18)$$

where  $\delta kx = (\bar{k} - k)x$  represents a residual phase error term. This error will depend on the initial estimate of the wave number  $k$  which can be iteratively improved as,  $\bar{k}^{\text{new}} = \bar{k} - \delta k$ .

To estimate an initial wave number, Herrin and Goforth (1977) used the multiple-filter technique. Many recent studies involving surface wave dispersion describe this technique in detail (e.g., Dziewonski *et al.*, 1969; Herrmann, 1973; Bache *et al.*, 1978; and Yan and Alexander, 1990). Following Herrmann (1973), a narrow bandpassed filtered seismogram may be constructed as

$$g(t,x) = \frac{\omega_o}{2\pi} \left( \frac{\pi}{\alpha} \right)^{1/2} \sum_m A_m(\omega_o, x) \exp \left[ i \left( \omega_o t - k_{o,m} x \right) \right] \exp \left[ -\frac{\omega_o^2}{4\alpha} \left\{ t - \frac{x}{U_{o,m}} \right\}^2 \right] \quad (19)$$

where  $A_m(\omega_o, x)$  is the amplitude spectrum of the  $m^{\text{th}}$  mode at frequency  $\omega_o$ , and the narrow-band Gaussian filter used to construct (19) has the form,

$$H(\omega) = \begin{cases} \exp(-\alpha \omega^2 / \omega_o^2) & |\omega| \leq \omega_c \\ 0 & |\omega| > \omega_c \end{cases}$$

The cut-off frequency ( $\omega_c$ ) and the filter bandwidth parameter ( $\alpha$ ) have been chosen in this study to be  $\omega_c = \omega_o/4$ , and  $\alpha = 16\pi$ , respectively. Note that in (19)  $U_{o,m}$  is the group velocity of the chosen mode,  $m$ , at frequency  $\omega_o$  which can be written as,  $U_{o,m} = x/t_g$ . Since the epicentral distance  $x$  is known, from the times corresponding to the maxima (group delay time) of the modulus of (19), a group delay curve can be obtained. From these group delay times of the signal at various frequencies, one can construct a group velocity dispersion curve. The application of the multiple-filter technique is effective when the wave trains belonging to two or more modes are superimposed in time, so long as these superimposed modes occur at different frequencies. From the group delay times of the fundamental mode signal at various frequencies, one can construct a phase spectrum given by

$$\phi = \int_0^{\omega} t_g d\omega. \quad (20)$$

This equation is used to compute the initial estimate of the wave number,  $k$ , ( $\phi = kx$ ) for the phase-matched filter. In practice, a family of wave numbers will result corresponding to multiples of  $2\pi$ . This can be resolved with a knowledge of one stable phase velocity estimate at a given period for the region under consideration.

The time-domain windowing (18) of the pseudo-autocorrelation function results in biased estimates in frequency domain. Detailed considerations for reducing the bias and a suitable choice of window functions used in the present study are given in Jenkins and Watts (1968) and Russell *et al.* (1988). A Parzen window is used for processing the phase spectrum while a cosine-tapered window is used to extract the amplitude spectrum. The total bias error due to windowing can safely be under 5%. Since we are interested in normalized spectral ratios, such bias may not be significant. In this study, both of these filtering techniques were utilized to extract the fundamental-mode amplitude spectra from each observed long-period seismogram.

## Simulations and Observations

A schematic drawing (Figure 2) shows the overall methodology adopted in this study. First, a suitable velocity model is chosen for the region under study. Synthetic spectral ratios of Love to Rayleigh waves are computed and a carefully designed neural network is then trained with these synthetic data. Necessary tuning of the network is done during the training and testing phase. If the performance becomes satisfactory upon testing with the training data set, synthetic spectral ratios at intermediate depths (other than those chosen for training) are generated for testing. Next, observed surface wave spectral ratios are constructed from as many recorded seismograms as possible, which when processed through the above trained network provides a focal depth estimation for that event. However, if for a given region well distributed observed events are available with pre-estimated focal depths, then a network may be constructed with the corresponding observed spectral ratios. Such a network should be ideally desirable, the advantage being that inherent noise, characteristic to the area under consideration, would also be incorporated in the learning process. Since such situations (enough observations for an appropriate mapping) are rarely true, our alternative, training a network with synthetic data derived from well constrained velocity models representing an area may be useful for focal depth estimations.

### *Synthetic Spectral Ratios*

Well constrained shear-velocity models for Eastern United States have been derived by many investigators (*e.g.*, Mitchell and Herrmann, 1979; Taylor and Toksoz, 1982). In this study, the Taylor and Toksoz (1982) velocity model (Figure 3), derived from the inversion of surface wave group and phase velocities, has been used. This model has also been used by Yan and Alexander (1990) for the estimation of focal depth and fault

orientations of the New Brunswick sequence. Since one of our aims is to compare the results obtained from our technique for the aftershock depths with those of Yan and Alexander (1990), it is essential to use the same model. Those authors showed that the velocity model explained the observed average dispersion along the paths from the New Brunswick source region to GDSN stations used in their study, very well.

Using the normal mode summation technique (Wang, 1981), fundamental-mode Love and Rayleigh wave spectra were generated and the corresponding ratios obtained. Since the neural network training process is very time consuming, we restricted the source parameters as follows: depths were restricted to 3 km and 17 km with an interval of 2 km, dip ranged from  $10^\circ$  to  $80^\circ$  with an interval of  $10^\circ$ , slip ranged from  $10^\circ$  to  $150^\circ$ , with an interval of  $10^\circ$  and strike ranged from  $175^\circ$  to  $225^\circ$  with an interval of  $10^\circ$ . The fault parameters were given by Yan and Alexander (1990). These parameters were chosen so as to incorporate all known source mechanisms of the New Brunswick sequence. Ideally, we would have liked to compute synthetics for all possible ranges with finer increments, but the training time would have become prohibitively long. A total of 4608 spectral ratios (feature vectors) were calculated in the period range of 15 to 51 sec (Figure 4).

#### *Neural Network Simulation*

Following Patnaik (1990), several feed-forward networks with 1, 2, or 3 hidden layers and varying numbers of processing units in each of these layers were simulated during our experiments. The input layer in each of these networks feeds a spectral ratio as an input vector and the 8 output units correspond to the 8 focal depths. An example 3-layer (Input-Hidden-Output) network simulated with a subset of the set of 4608 feature vectors is shown in Figure 5. Note the correct classification of all 8 classes corresponding to the 8 depths (3 km to 17 km). The final design of the network, which has been used for subsequent focal depth estimation, has 4 layers consisting of 12, 60, 48, and 8 units. During the training at intermediate steps, the ability of this network to correctly classify training feature vectors was repeatedly tested. The results are shown in Figure 6. Note that within about 700 cycles (where all the patterns have been fed-forward once, errors propagated backward once, and connections adjusted to, constitutes a cycle), the network learned to classify correctly at nearly the 77% level. As the training continued, the total mean-square-errors computed across all the 8 output units decreased, as shown in Figure 7. This curve, also known as network learning curve, implied that the gradient still existed and that there had been no encounter with local minima. This meant that with further training the accuracy or percent correct classification would increase. For these 700 cycles of learning, with the back-error-propagation algorithm (1-4), the time spent were nearly 23 hours of CPU-time on a SUN-4 Sparcstation (12 MIPS). On another simulation of a 3-layer network with the mean-field-theory learning algorithm (5-13), the training process seemed fairly slow. Since we did not encounter any local minima in the back-error-propagation training, the simulation was continued with the same 4-layer network. When the entire training set (4608 features)

was tested at the 80% level, the response of the output units showed correct classifications as shown in Figure 8. The response curves peak at the corresponding depth values.

### *The New Brunswick Sequence*

The January 9, 1982 New Brunswick main-shock and three of its aftershocks studied in this paper are listed in Table 1. The locations of these events and their paths to GDSN stations are shown in Figure 9. The main shock source parameters have been studied by many investigators using body wave and surface wave data (e.g., Choy *et al.*, 1983; Nguyen, 1985; Wetmiller, *et al.*, 1984; Yan and Alexander, 1990). The estimated depth range varies from 7 to 9.5 km in these studies.

Long-period surface wave time signals were obtained from the GDSN stations ANMO, ALQ, SCP, and LON. The instrument responses were removed in the frequency domain. Rayleigh waves were extracted from the vertical components and the horizontal components were rotated to obtain Love waves (transverse component). Spectral ratios between 15 - 51 sec were constructed using the phase-matched-filtered fundamental-mode Love and Rayleigh wave amplitude spectra. Upon testing with the synthetically trained neural network, the estimated depth came out to be  $7 \pm 1$  km for the main shock. Figure 10 shows the output response obtained from the observed spectral ratios. The peak corresponds to a target depth of 7 km and the broadened pulse shape provides the uncertainty, which is  $\pm 1$  km in this case.

Note that the small hump (Figure 10) to the left of the peak at 7 km is a nominal response at 3 km produced by the spectral ratio observed at the station LON. We attribute this to noise, since the majority of the best-matches peak at 7 km.

We also conducted a least-squares search to find the theoretical ratio which matches the main shock spectral ratio at station ANMO. The best fit is shown in Figure 11. The depth corresponding to this theoretical spectral ratio is 7 km. Instead of an exhaustive search, the search range was limited to within  $\pm 10^\circ$  of the known main-shock fault parameters. The spectral ratios corresponding to this search range also constitutes a subset of the original training set of 4608 spectral ratios.

Similar procedures for signal processing were adopted for the three aftershocks (Table 1) of the New Brunswick event, and the corresponding spectral ratios were generated. Testing was done with the same trained 4-layer neural network. The output responses obtained are also displayed in Figure 10. The depths estimated for the three aftershocks agree within  $\pm 1$  km of those reported by Yan and Alexander (1990). A comparative listing of our estimated depths is given in Table 2.

### *Southern Indian Ocean Events*

Since the estimated depths for the New Brunswick sequence were within  $\pm 1$  km of those reported by several authors, the applicability of the present technique seems satisfactory. Therefore, our proposed algorithm (Figure 2) for depth estimation with

multilayered neural networks may be utilized for events that have not been studied. To examine this assertion, we estimated the depths of two oceanic events which occurred in Southern Indian Ocean (Figure 14). Using an earlier derived shear velocity model from the inversion of Love and Rayleigh wave group velocities and using the same techniques for the computation of Love to Rayleigh wave spectral ratios as in the case of New Brunswick sequence, 3240 spectral ratios, within the period range of 18 - 78 sec, were computed (Figure 12). These spectral ratios correspond to five different focal depths (5.0, 7.5, 10.0, 12.5, and 15 km). This chosen depth range is typical of the focal depths of events that occur in this region. The fault parameters chosen were, dip from  $0^\circ$  to  $80^\circ$ , at  $10^\circ$  intervals, slip from  $40^\circ$  to  $150^\circ$ , at  $10^\circ$  intervals and strike from  $175^\circ$  to  $225^\circ$ , at  $10^\circ$  intervals. With the synthetic spectral ratios, several neural networks with various architectures (combinations of number of layers and number of processors in each layer) were simulated. Initial training with the mean-field-theory learning algorithm turned out to be slow, as expected. Finally, a 4-layer feed-forward back-error-propagation network (15, 60, 30, and 5 units) was chosen for the training. The network learning curve after 5200 cycles is shown in Figure 13. The time required for this partial training (at the 90% level) was nearly 37 hours of CPU time on a SUN-4 Sparcstation. As seen in Figure 13, the gradient still exists and the network could learn at higher than the 90% level with more training. The same procedure followed in the previous simulation for training and testing were also followed in the present experiment.

The two events chosen for depth estimation are shown in Figure 14 and listed in Table 3. Long period SRO seismograms were retrieved from the GDSN station NWA0. These were processed, and Love and Rayleigh wave spectral ratios were generated. After testing with the partially trained network for the oceanic model, the output responses were obtained as shown in Figure 15. The estimated depth for the 08 Jun 82 event is  $10 \pm 1$  km which agrees well with a depth of 10 km reported both by NEIS and ISC. The estimated depth for the other event of 10 Apr 82 is  $7.5 \pm 1$  km which is between the Harvard Centroid depth (10 km) and ISC quoted depth  $5 \pm 1.7$  km, determined from the time difference of pP - P. In general, the agreements are quite satisfactory (Table 4).

#### *Noise Tolerance Test*

Since the synthetic spectral ratios used for network training were noise free, we examined the robustness of the learning technique in the presence of noisy feature vectors (spectral ratios). Using the same oceanic velocity model, 300 Love to Rayleigh wave spectral ratios were generated for three focal depths: 5, 10, and 15 km, corresponding to the fault parameters: dip  $10^\circ$  to  $40^\circ$ , at  $10^\circ$  intervals, slip  $10^\circ$  to  $50^\circ$ , at  $10^\circ$  intervals, and strike  $10^\circ$  to  $50^\circ$ , at  $10^\circ$  intervals. The obvious reason for the small number of patterns is to construct a smaller network, and thereby, speed up the training time. A three-layer feed-forward (15, 45, and 3 units) network was designed and trained with this noise-free data set. Pseudo-random noise was generated at 10%, 20%, 30% and 40% levels and added to the spectral ratios. Each of the four sets of these noise-contaminated spectral

ratios were then used to train and test the same network. The network learning curves for all five cases are shown in Figure 16. The solid line is the noise-free data, and open circles, triangles, pluses, and crosses correspond to 10%, 20%, 30% and 40% noise levels, respectively. As is evident from Figure 16, the total mean-square-error remains higher for the training data with higher noise level. However, the important observation is that even with a 40% noise level, the network still learns to correctly classify over 70% of the training set. The gradient in each of the curves indicates that with further training, better performance could be obtained. Figure 17 shows the histograms of the percentage of correct classifications for each target depth. The histograms show results obtained for testing the training sets with different noise levels, after 2000 cycles each.

## Discussion and Conclusions

This study has shown that neural networks can successfully be used with surface wave spectral ratios to obtain focal depths of shallow events. During our initial simulation and subsequent testing with observed data it was seen that success of the resultant networks required accurate source and crustal models. This was also evident in earlier studies directly using spectral ratios (*e.g.*, Harkrider, 1970; Masse *et al.*, 1973; Yan and Alexander, 1990). The neural network technique developed here uses the location of the spectral holes (*e.g.*, Harkrider, 1970; Tsai and Aki, 1970; Masse *et al.*, 1973) as well as the shape of the normalized amplitude spectral ratios to obtain a map between depths and corresponding ratios. Azimuth dependence is included through the choice of many strike possibilities of the source. Although all static source parameters (depth, dip, slip, strike) can, in principle, be obtained with this technique, because of the CPU-time requirements, we restricted our problem only to depth estimation. Determination of all parameters will require a faster computer such as a parallel processor to speed up the training process. Once trained, however, the network can be implemented on a slower machine for application purposes.

One problem with this technique is that, at present, there is no network architecture available which can account for missing data points; therefore, interpolated values must be supplied to fill in those points. It is therefore desirable, when making determinations of focal depth, to use observed spectral frequencies which are identical to those used for training, so that assumed values do not need to be provided.

In the noise tolerance test we have added random noise to the surface wave spectral data. For deterministic signals (well-dispersed surface waves) such noise may not be realistic. Therefore an alternative approach might be to obtain actual noise from long period digital seismograms, over the time interval preceding the signal, and add that to the synthetic data for training.

The generalization capability of a trained neural network for the problem of focal depth estimation must be addressed, where generalization means reasonable response



to unknown inputs. Such inputs may fall outside the mapping boundary of the network. As an example, one of the networks has been trained for the depth range of 3 km to 17 km. Therefore, the network is capable of approximating those spectral features that are continuously mapped in this depth range. If, however, a spectral ratio corresponding to a depth of 30 km is presented to the network, it would produce some response which would be meaningless. This difficulty arises from the fundamental problem inherent in mappings through bounded inputs/outputs. Since the feature space (possible range of focal depths in a region) is unbounded and the output classes are bounded (3 km to 17 km), these difficulties may arise. However, there can always be judicious applications of this useful technique. From a seismological perspective, one may first choose to use deeper event depth identifiers such as pP-P times. If that depth estimate falls outside the depth range of a trained network it should not be used. The present technique is suitable for shallower events only. On the other hand, one may choose to synthesize features for a larger depth range to train a network. This will be limited again by the availability of computing power.

Currently there is no well-established way to predict the internal dynamics of a neural network so as to understand how a network actually learns a given mapping. Approximate techniques such as the analysis of the connection matrix of a trained network is often done for simpler problems and smaller networks (Elman and Zipser, 1988; Gorman and Sejnowski, 1988). For the present application of a 4-layer network, such an analysis would be extremely difficult, and perhaps meaningless. From a physical perspective, the network dynamics is seen as *chaotic* and attempts have been made (e.g., Choi and Huberman, 1983; Geman and Geman, 1984; Clark, 1988) to study the underlying physics. The theory of neural computing is still evolving, and many issues still remain to be answered.

In this study involving neural computing, we have presented a data-intensive, region-specific novel technique of nonlinear transfer function approximation as applied to the estimation of earthquake focal depths from surface wave amplitude spectral ratios. The technique is to train a neural network with the depth-dependent mapping of the spectral ratios such that when an observed spectral ratio is processed through it, a corresponding depth is estimated.

Application of the technique to the 1982 New Brunswick main-shock and three of its aftershocks produced depth estimates within  $\pm 1$  km of the well calibrated depths reported by other investigators.

Application to two events in the southern Indian Ocean provided depths for which, one of the events (04/10/82) agreed to within  $\pm 2.5$  km of the reported centroid depth and ISC reported depth from the (pP - P) times. For the other event (06/08/82), the estimated depth was within  $\pm 1$  km of the depths reported for that region by the NEIS and ISC.

## Acknowledgements

We gratefully acknowledge the comments of Dr. Thomas Bache regarding the problem of bounded input/output. His comments brought the limitations of the presented method to our attention. We would also like to thank Dr. Robert Herrmann for critically reading the manuscript and for pointing out to us the unpublished results of Dr. Nguyen concerning the focal depths of New Brunswick sequence. This research was supported by the Advanced Research Projects Agency of the Department of Defense and was monitored by the Geophysics Laboratory under contract #F19628-89-K-0021.

## References

- Bache, T.C., W.L. Rodi and D.G. Harkrider (1978). Crustal structure inferred from Rayleigh-wave signatures of NTS explosions, *Bull. Seism. Soc. Am.*, **68**, 1399-1413.
- Choi, M.Y. and B.A. Huberman (1983). Dynamic behavior of Nonlinear networks, *Physical Review A*, **28**, No. 2, 1204-1206.
- Choy, G.L., J. Boatwright, J.W. Dewey, and S.A. Sipkin (1983). A teleseismic analysis of the New Brunswick earthquake of January 9, 1982, *J. Geophys. Res.*, **88**, 2199-2212.
- Clark, J.W. (1988). Statistical mechanics of neural networks, *Physics Reports*, **158**, 9-157.
- Dziewonski, A., S. Block, and M. Landisman (1969). A technique for the analysis of transient seismic signals, *Bull. Seism. Soc. Am.*, **59**, 427-444.
- Elman, J.L. and D. Zipser (1988). Learning the hidden structure of speech, *J. Acoust. Soc. Am.*, **83**, No. 4, 1615-1626.
- Geman, S. and D. Geman (1984). Stochastic relaxation, Gibbs distribution, and Bayesian restoration of images, *IEEE Trans. Pattern Anal. and Machine Intell.*, **PAMI-6**, 721-741.
- Glauber, R.J. (1963). Time-dependent statistics of the Ising model, *J. Math. Phys.*, **4**, 294-307.
- Goforth, T. and E. Herrin (1979). Phase-matched filters: application to the study of Love waves, *Bull. Seis. Soc. Am.*, **69**, 27-44.
- Gorman, R.P. and T.J. Sejnowski (1988). Analysis of Hidden Units in a layered Network trained to classify Sonar targets, *Neural Networks*, **1**, 75-89.
- Harkrider, D.G. (1964). Surface waves in multilayered elastic media, 1. Rayleigh and Love waves from buried sources in a layered media, *Bull. Seism. Soc. Am.*, **64**, 627-679.
- Harkrider, D.G. (1970). Surface waves in multilayered elastic media, Part II; Higher mode spectra and spectral ratios from point sources in plane-layered Earth models, *Bull. Seism. Soc. Am.*, **60**, 1937-1987.
- Haskell, N. S (1953). The dispersion of surface waves on multilayered media, *Bull. Seis. Soc. Am.*, **43**, 17-34.

- Haskell, N.S (1964). Radiation pattern of surface waves from point sources in a multi-layered medium, *Bull. Seis. Soc. Am.*, 73 , 1685-1699.
- Herrin, E., and T. Goforth (1977). Phase-matched filters: application to the study of Rayleigh waves, *Bull. Seis. Soc. Am.*, 67 , 1259-1275.
- Herrmann, R. B. (1973). Some aspects of band-pass filtering of surface waves, *Bull. Seism. Soc. Am.*, 63 , 663-671.
- Herrmann, R.B. (1979). Surface wave focal mechanisms for eastern North American Earthquakes with tectonic implications, *J. Geophys. Res.*, 84, No. B7, 3543-3552.
- Hopfield, J.J. (1982). Neural networks and physical systems with emergent collective computational abilities, *Proc. Nat. Acad. Sci.*, 79 , 2554.
- Hopfield, J.J. and D.W. Tank (1985). "Neural" computation of decisions in optimization problems, *Biol. Cybernetics*, 52 , 114-152.
- Jenkins, G. M., and D. G. Watts (1968). *Spectral Analysis and Its Applications* , Holden Day, San Francisco.
- Khotanazad, A. and J.H. Lu (1990). Classification of invariant image representations using a neural network, *IEEE. Trans. ASSP*, 38 , No.6, 1028-1038.
- Lippmann, R.P. (1987). An introduction to computing with neural nets, *IEEE ASSP Mag.*, 4, 4-22.
- Masse, R.P., D.G. Lambert, and D.G. Harkrider (1973). Precision of the determination of focal depth from the spectral ratio of Love/Rayleigh surface waves, *Bull. Seism. Soc. Am.*, 63, 59-100.
- Mitchell, B.J. and R.B. Herrmann (1979). Shear velocity structure in the eastern United States from the inversion of surface-wave group and phase velocities, *Bull. Seism. Soc. Am.*, 69, 1133-1148.
- Moody, J. and C.J. Darken (1989). Fast learning in networks of locally tuned processing units, *Neural Computation*, 1 , 281-294.
- Moussouris, J. (1974). Gibbs and Markov random systems with constraints, *J. Stat. Phys.*, 10 , 11-33.
- Nguyen, B.V (1985). Surface wave focal mechanism, magnitude, and energies from

some Eastern North American earthquakes with tectonic implication, *M.S. Thesis*, Saint Louis University, pp.275.

- Patnaik, G.B (1990). On the simulation of Artificial Neural Networks for seismic surface wave type classification, in *IAMG Studies in Mathematical Geology*, 4, Oxford University Press (in Press).
- Peterson, C. and J. R. Anderson (1987). A Mean Field Theory Learning Algorithm for Neural Networks, *Complex Systems*, 1, No.5 ,995-1019.
- Rumelhart, D.E. and J.L. McClelland and the PDP Group (1986). Parallel distributed processing, *Explorations in the Microstructure of Cognition*, MIT Press, 1, pp. 547.
- Russell, D.R. (1987). Multi-channel processing of dispersed surface waves, *Ph.D. Thesis*, Saint Louis University, pp.150.
- Russell, D.R, R.B. Herrmann and H.J. Hwang (1988). Application of frequency variable filters to surface-wave amplitude analysis, *Bull. Seism. Soc. Am.*, 78, No.1, 339-354.
- Sejnowski, T.J., P.K. Kienker and G.E. Hinton (1986). Learning symmetry groups with hidden units: Beyond Perceptron, *Physica*, 22D, 260.
- Sompolinsky, H. (1988). Statistical mechanics of neural networks, *Physics Today*, 12 , 70-80.
- Takeda, M. and J.W. Goodman (1986). Neural Networks for computation: Number representation and programming complexity, *Applied Optics*, 25, No.18, 3033-3046.
- Taylor, S.R. and M.N. Toksoz (1982). Structure in the Northeastern United States from inversion of Rayleigh waves phase and group velocities, *Earthquake Notes*, 53, No. 4 , 5-24.
- Toksoz, M.N., A. Ben-Menahem, and D.G. Harkrider (1964). Determination of source parameters of explosions and earthquakes by amplitude equalization of seismic surface waves, *J. Geophys. Res.*, 69, 4355-4366.
- Tsai, Y.B and K. Aki (1970). Precise focal depth determination from amplitude spectra of surface waves, *J. Geophys. Res.*, 75 ,5729-5743.
- Tsai, Y.B. and K. Aki (1971). Amplitude spectra from small earthquakes and underground nuclear explosions, *J. Geophys. Res.*, 76, 3940-3952.

Wang, C-Y. (1981). Wave theory for seismogram synthesis, *Ph.D. Dissertation*, Saint Louis University, 235 pp.

Wetmiller, J.A., F.M. Anglin, H.S. Hasegawa, and A.E. Stevens (1984). Aftershock sequences of the 1982 Mirimachi, New Brunswick, earthquakes, *Bull. Seism. Soc. Am.*, 74, 621-653.

Yan, B. and S. Alexander (1990). Source mechanism study of the 1982 New Brunswick, Canada, Earthquake sequence using combined surface wave methods, *Bull. Seis. Soc. Am*, 80, No.2, 296-312.

Table 1  
The New Brunswick Sequence of 1982

Date	Origin Time	Latitude (°)	Longitude (°)	$m_s$	Station/Data
January 9	12:53:51.8	46.984	-66.656	5.7	ANMO, ALQ, SCP, LON
January 9	16:36:42.9	47.023	-66.648	5.1	ANMO, ALQ, SCP
January 11	21:41:07.9	46.975	-66.659	5.4	LON
March 31	21:02:20.0	47.000	-66.600	5.0	ANMO, SCP

\* NEIS

Table 2  
New Brunswick Focal Depths  
(Comparison With Other Estimations)

Authors	Event	Depth (Km)
Choy et al. (1983)	Main Shock	9
Nabelek (1984)	"	7
Wetmiller et al. (1984)	"	7
Nichols (1984)	"	7
Nguyen (1985)	"	9.5
Yan and Alexander (1990)	"	7
Present Study	"	7±1
Yan and Alexander (1990)	09 Jan 82	6
Nguyen (1985)	"	6
Present Study	"	7±1
Yan and Alexander (1990)	11 Jan 82	6
Nguyen (1985)	"	7.5
Present Study	"	5±1
Yan and Alexander (1990)	31 Mar 82	3
Present Study	"	3±1

From Yan and Alexander (1990).



Table 3

## The Southern Indian Ocean Events

Date	Origin Time	Latitude ( $^{\circ}$ )	Longitude ( $^{\circ}$ )	$m_s$	$M_s$	Station/Data
10 Apr 82	06:47:51.9	-33.95	58.0	5.6	5.4	NWAO
08 Jun 82	16:30:41.4	-41.9	88.3	5.4	5.6	NWAO

'NEIS

Table 4  
Indian Ocean Focal Depths  
(Comparison With Reported Depths)

Source	Event	Depth (Km)
NEIS	10 Apr 82	10
HRVD	"	10
ISC (pP - P)	"	$5 \pm 1.7$
Present Study	"	$7.5 \pm 1$
NEIS	08 Jun 82	10
ISC	"	10
Present Study	"	$10 \pm 1$

## Figure Captions

Fig 1. The schematic on the left represents a three-layer neural network which can be trained using a learning algorithm (Error-back-propagation, Boltzmann Machine, or Mean-field-theory). The upper-right figure shows an analog equivalent of the functions within a single neuron (unit). The non-linear element uses a *sigmoidal* function (bottom-right). Note that at 0 activation and high gain, the neuron behaves as a comparator or a flip/flop. However, at low gain and other activation values, the non-linearity controls the overall dynamics of the network.

Fig 2. A schematic representation of focal depth estimation with a neural network. The neural network is trained with synthetic data and tested with observed and/or synthetic data.

Fig 3. The shear-velocity model of Taylor and Toksoz (1982) for the Eastern United States. This model is used for the calculation of synthetic surface wave spectral ratios.

Fig 4. Superposition of 4608 normalized spectral ratios calculated with the Eastern United States velocity model for different combinations of dip, slip, strike and depth.

Fig 5. Schematic of an example 3-layer feed-forward back-error-propagation neural network that has been trained with a subset of Love to Rayleigh wave spectral ratios computed for the eastern United States velocity model. The connection matrices are in the middle. The Input, Hidden and Output responses are shown at the right.

Fig 6. Improvements in network learning by increasing the number of training steps. The histograms show the number of patterns classified at a given target depth. The darker bars are the final network estimates. The lighter shaded bars are the results obtained from intermediate tests using 50 and 450 steps. Note the wider distribution of depths at early learning stages of the network. When the number of training steps increases, the depth distribution for corresponding target depths become sharper. The expected distribution for a classification that is 100% correct is a spike located at that target depth.

Fig 7. The network learning curve (total mean-square-error vs. number of training cycles) of the neural network trained with the spectral ratios computed from the eastern United States velocity model.

Fig 8. Response of the partially trained network upon testing with the training set. Each response curve peaks at its corresponding depth. The sharper the peaks, the better the resolution.

Fig 9. Location of the New Brunswick earthquake and its aftershocks. The DWWSSN stations are LON, ALQ, and SCP. ANMO is the SRO station.

Fig 10. Response of the partially trained network (over 80% learned) to the spectral ratios of the New Brunswick earthquake and three of its aftershocks. The peaks correspond to estimated depths.

Fig 11. A comparison of normalized observed (solid circles) and theoretical (solid line) fundamental mode amplitude spectral ratio of Love to Rayleigh wave for the Eastern United States model.

Fig 12. Superposition of 3240 normalized spectral ratios calculated for the southeastern Indian Ocean velocity model for different combinations of dip, slip, strike and depth.

Fig 13. Network learning curve corresponding to the southern Indian Ocean velocity model. The high-frequency oscillations on this curve are, possibly, the result of underlying dynamics which is often chaotic.

Fig 14. Epicenters of the events located in the southern Indian Ocean and their paths to the GDSN station NWA0.

Fig 15. Response of the partially trained network (over 90% learned) to the spectral ratios of two events in the southern Indian Ocean. The peaks correspond to the estimated depths.

Fig 16. Network learning curve with respect to training at various levels of noise added to the spectral ratios.

Fig 17. The noise tolerance test conducted with a smaller network for 5,10, and 15 km target depths. The histograms show the depth distribution over each target depth with 10%, 20%, 30%, and 40% noise levels. The darkest bars represent the 10% noise level and the lightest bars represent the 40% noise level. When noise level is increased, the percentage of correct classifications gradually decreases. At all the noise levels, the percentage remains almost the same which indicates that the network is relatively noise insensitive.

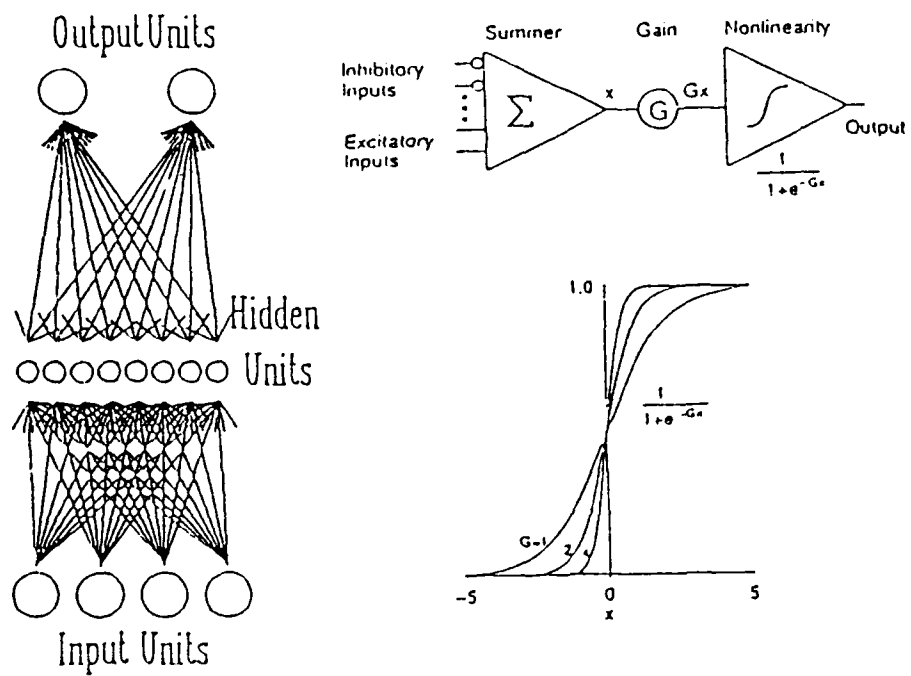


Figure 1

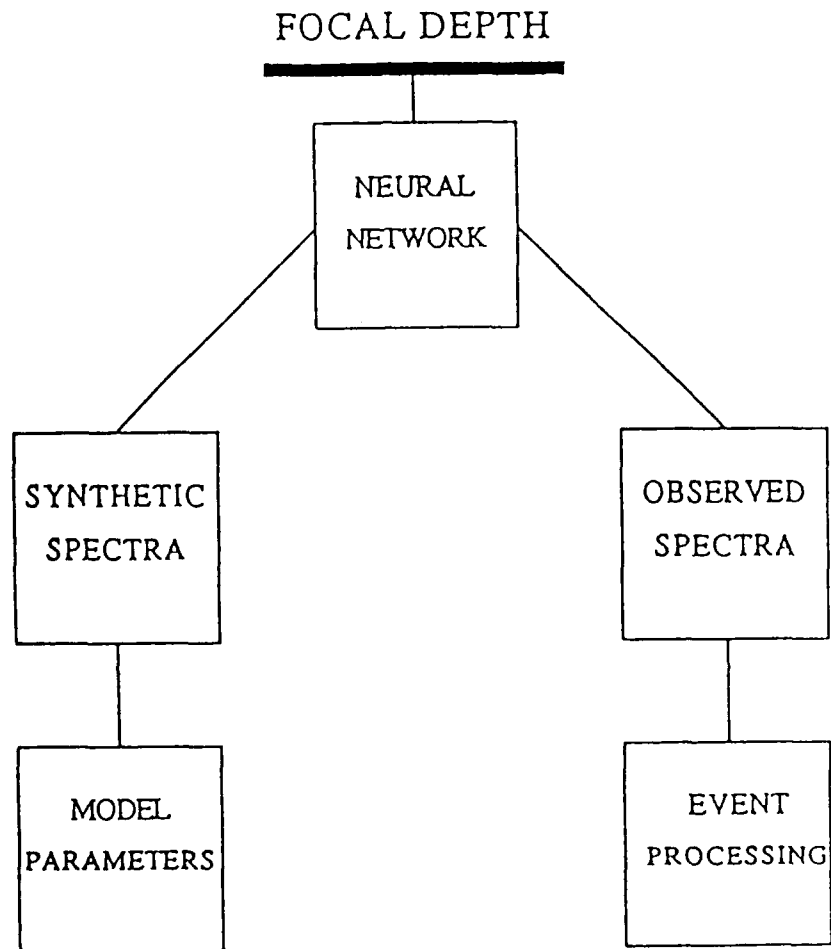


Figure 2

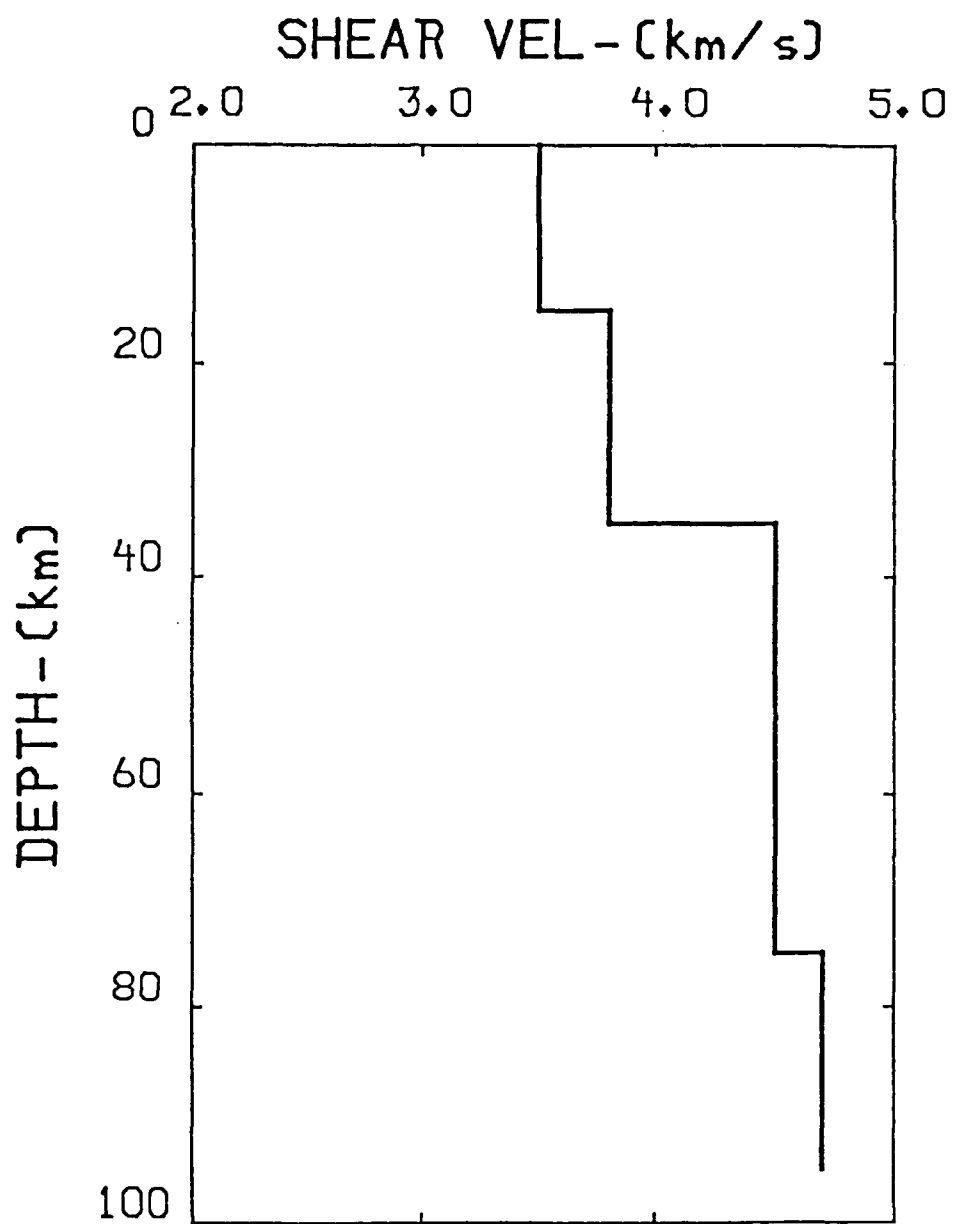


Figure 3

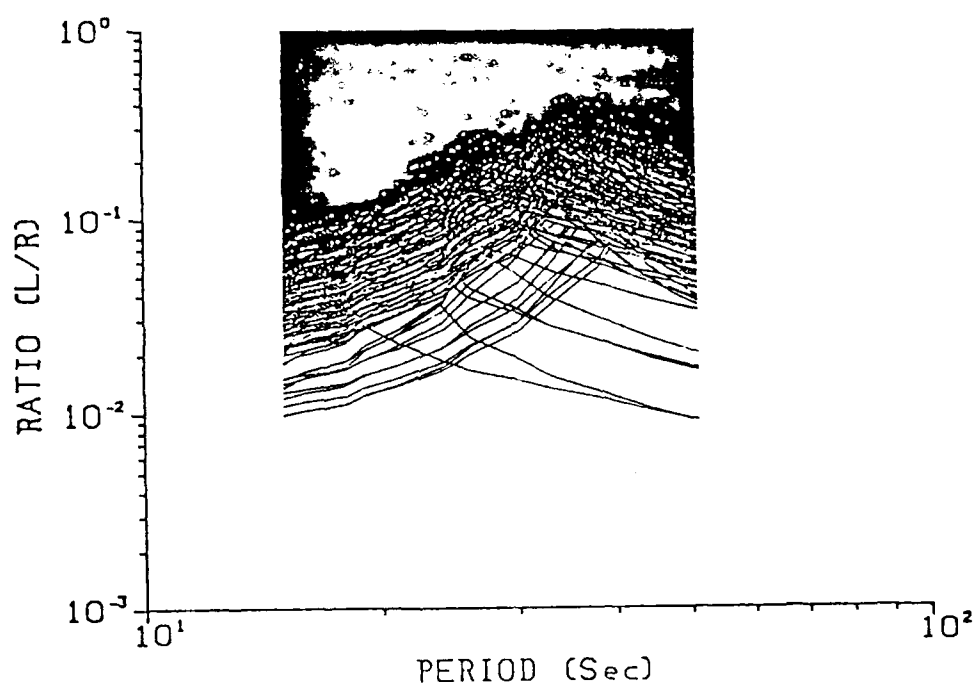


Figure 4



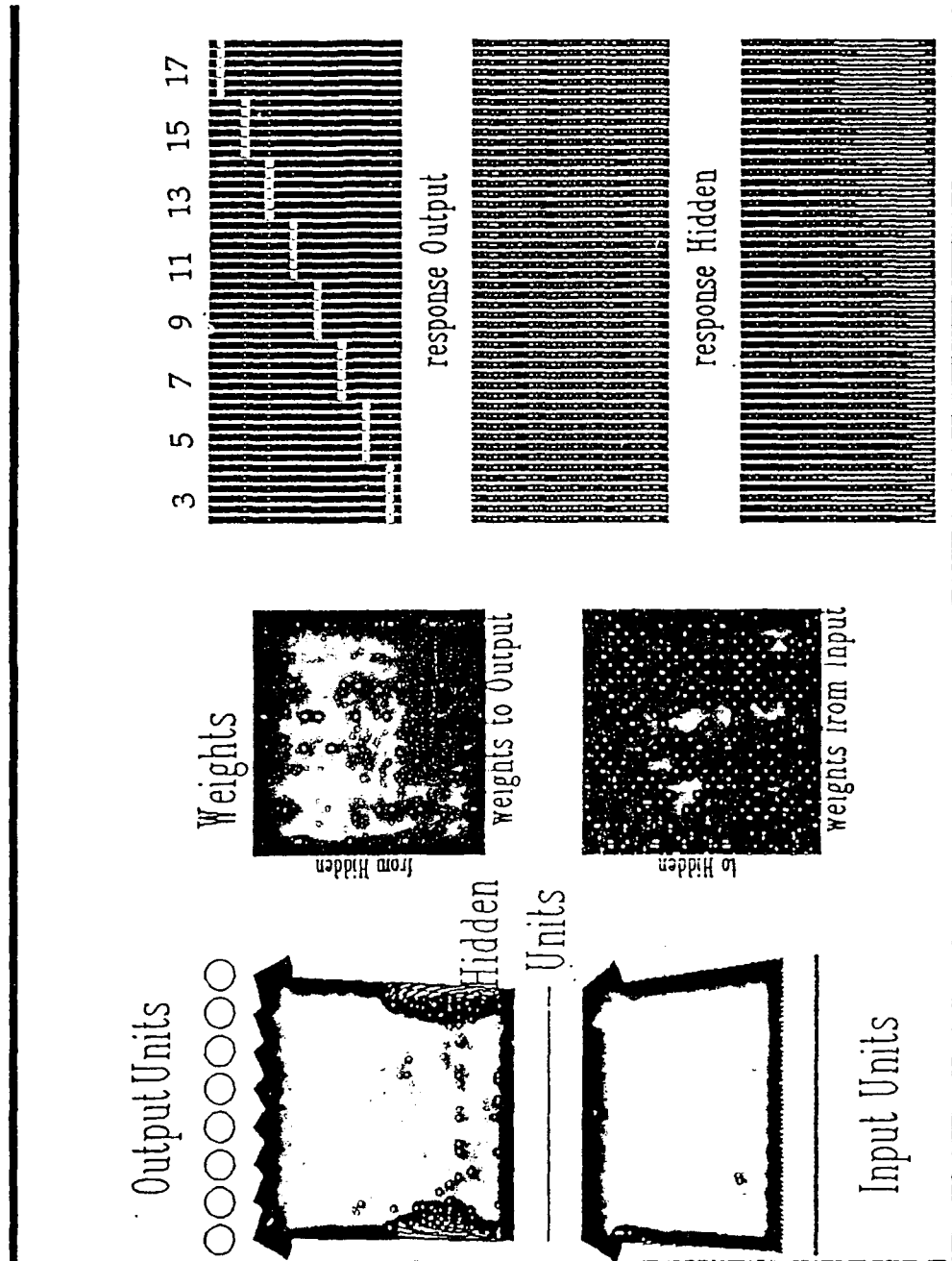


Figure 5

# OVERALL PERCENTAGE CLASSIFICATION

50-steps: 57% ; 450-steps: 74% ; 700-steps: 77%

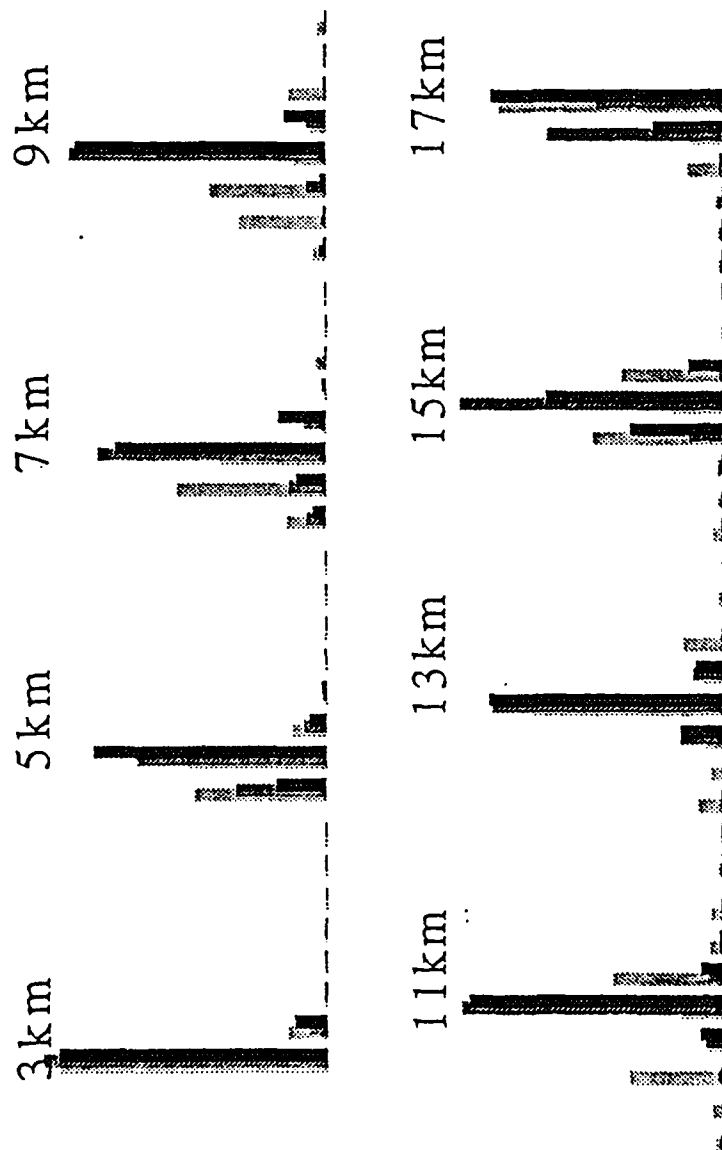


Figure 6

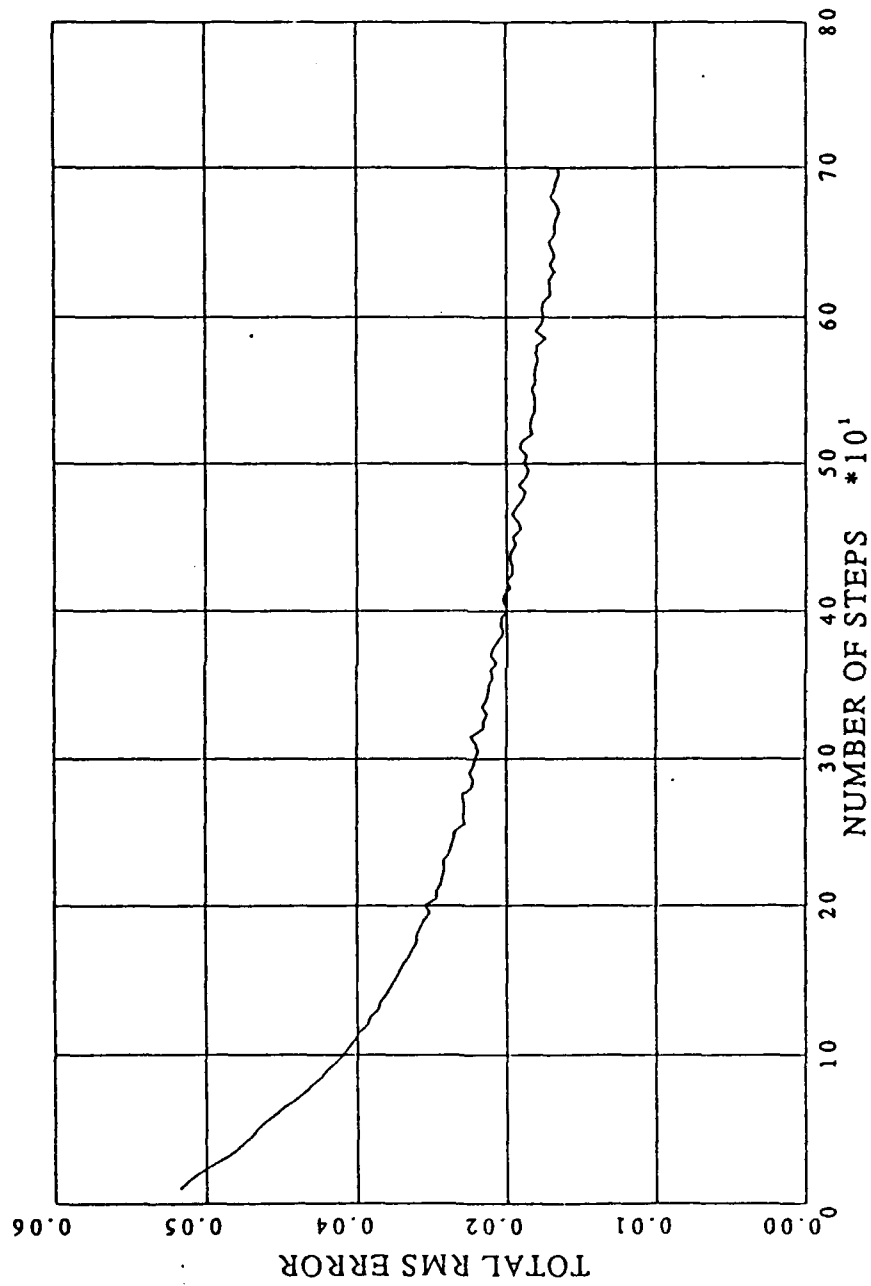


Figure 7

# TESTING THE TRAINING SET (Synthetic Spectral Ratios)

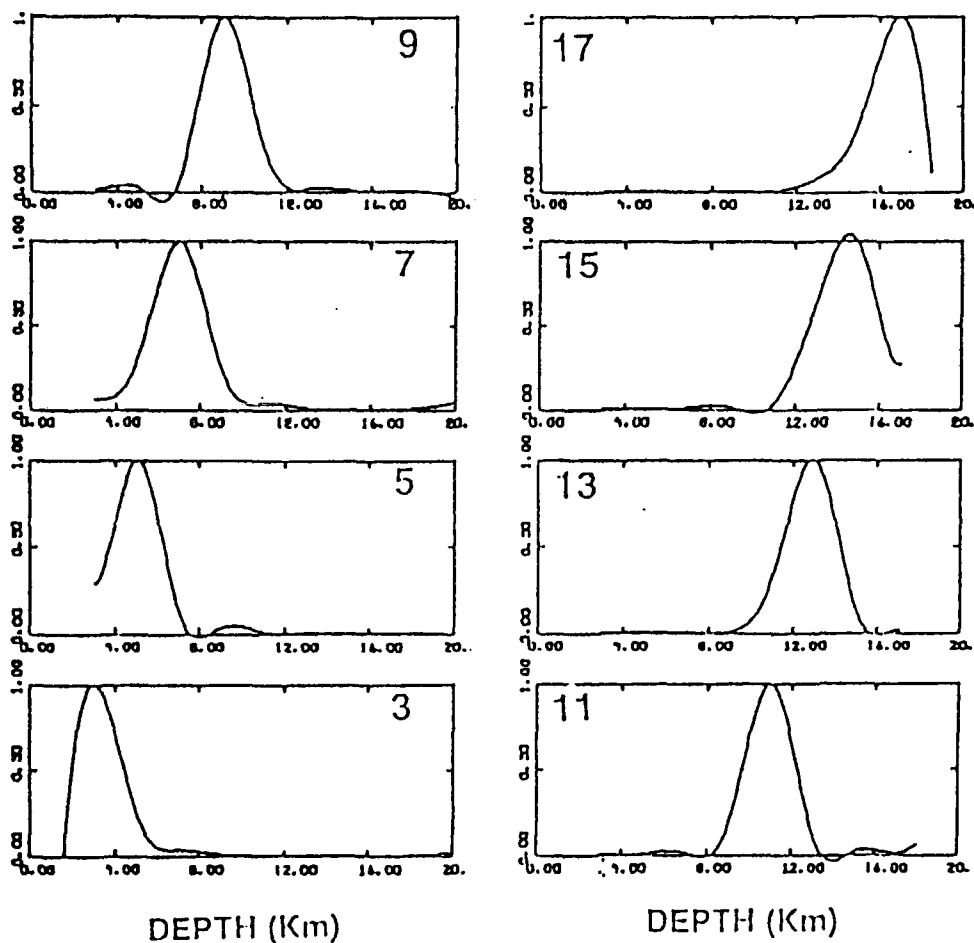


Figure 8

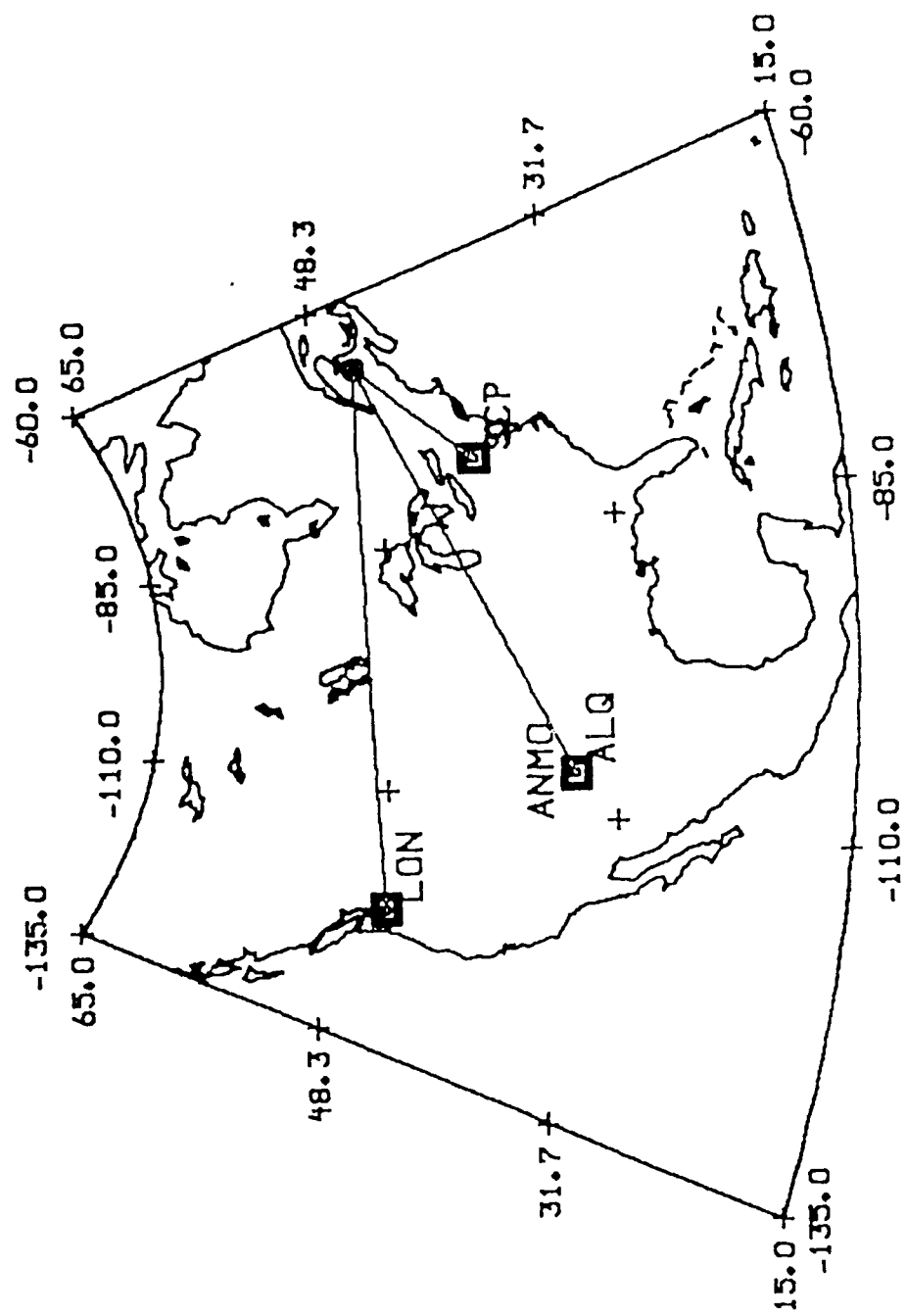


Figure 9

# ESTIMATED DEPTHS (New Brunswick Sequence)

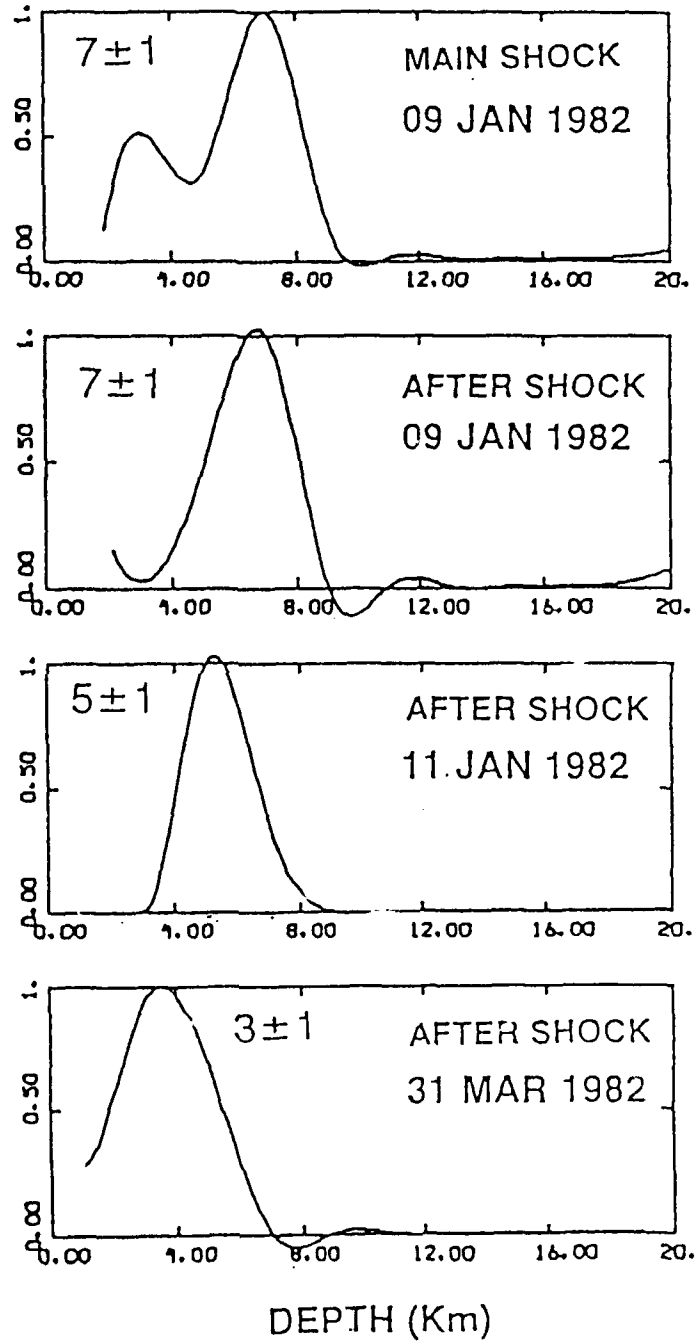


Figure 10

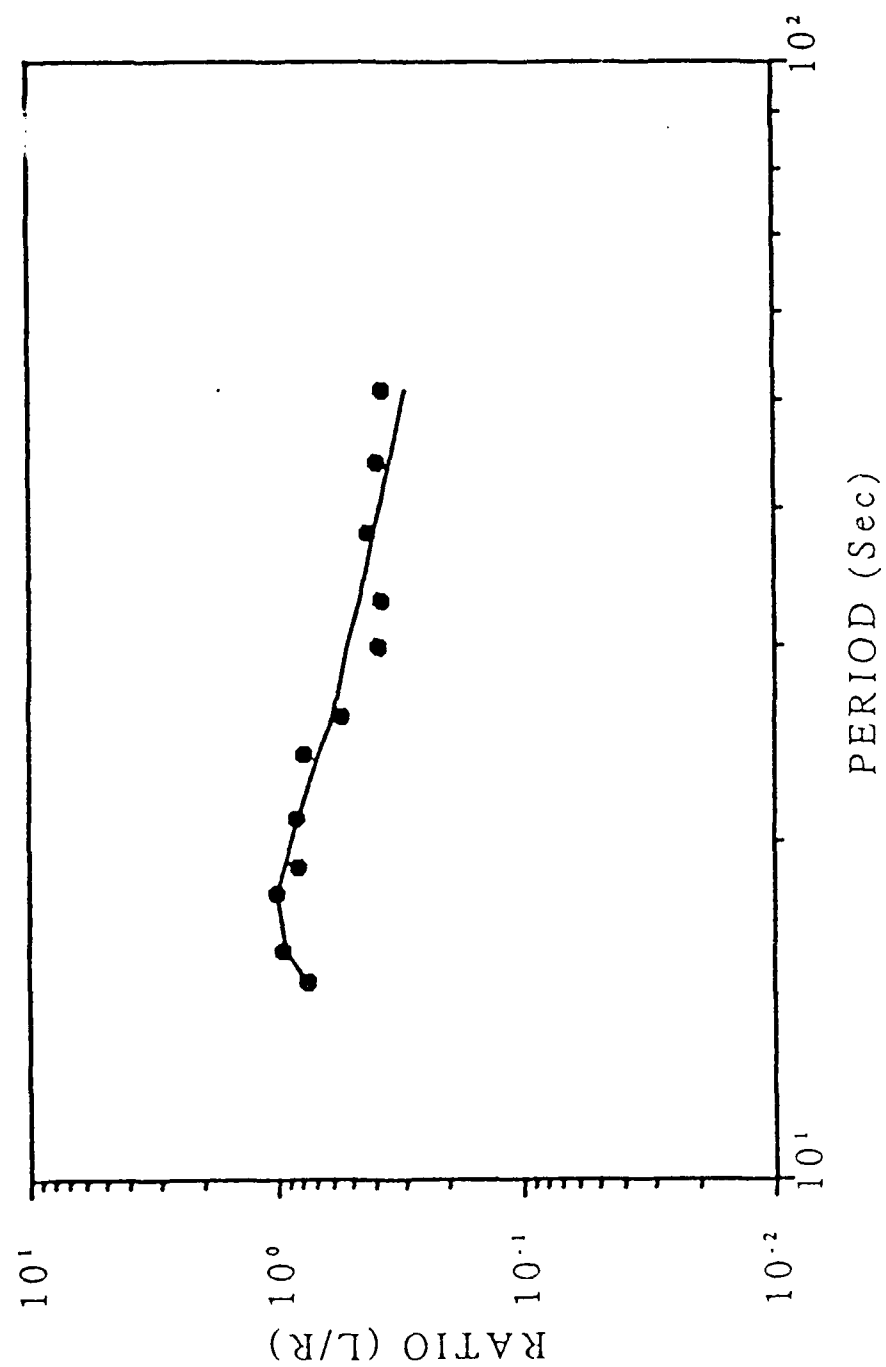


Figure 11

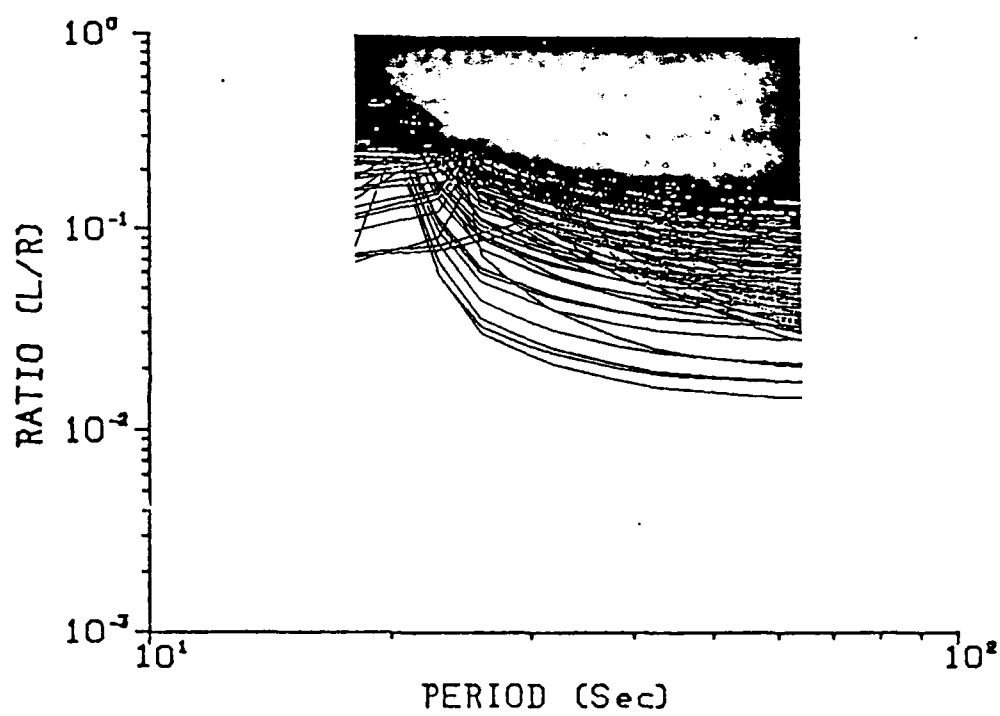


Figure 12



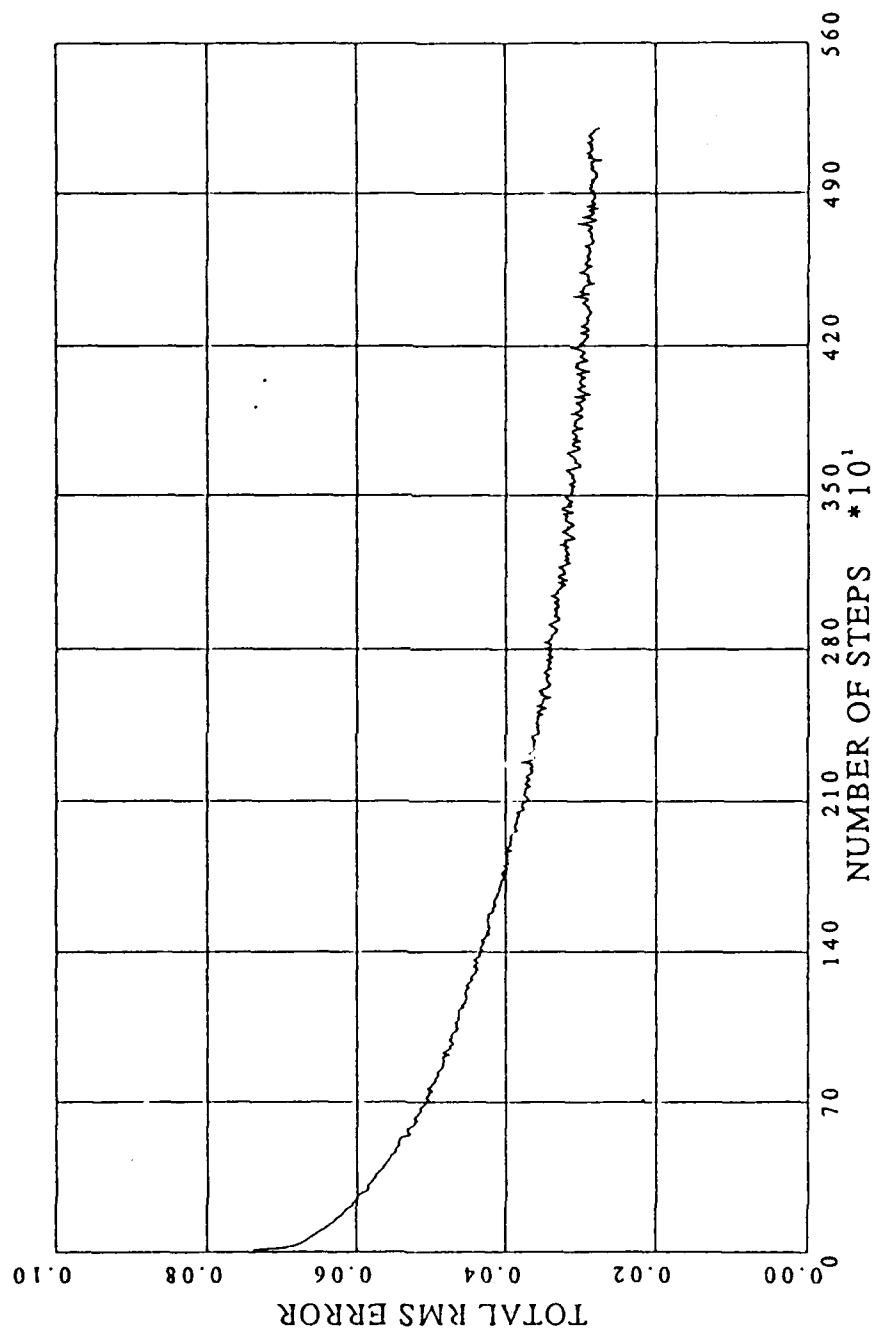


Figure 13

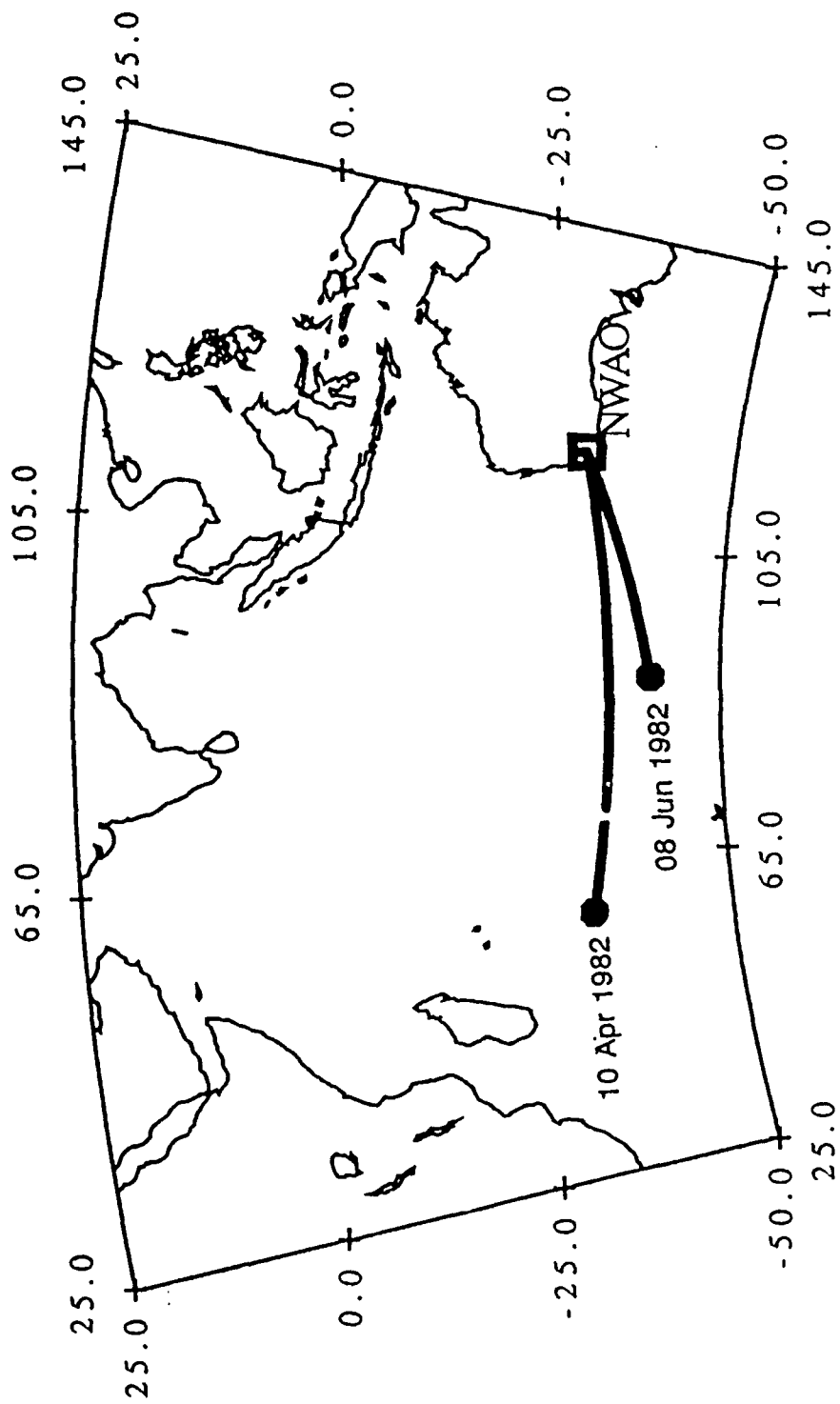


Figure 14

ESTIMATED DEPTHS  
(Southern Indian Ocean Events)

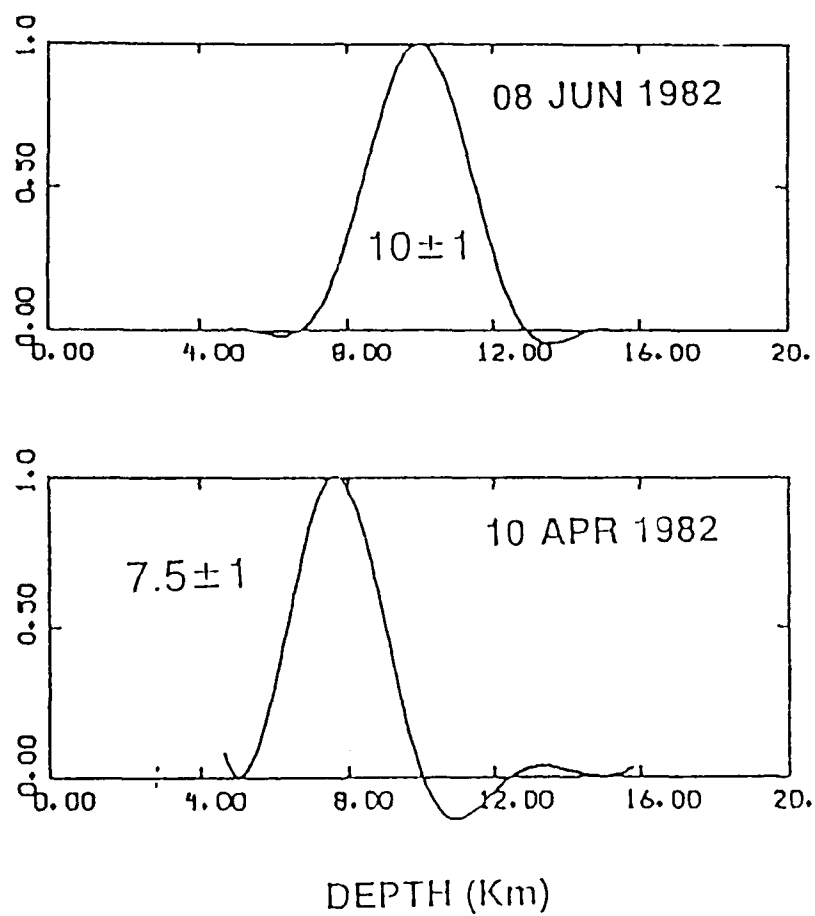


Figure 15

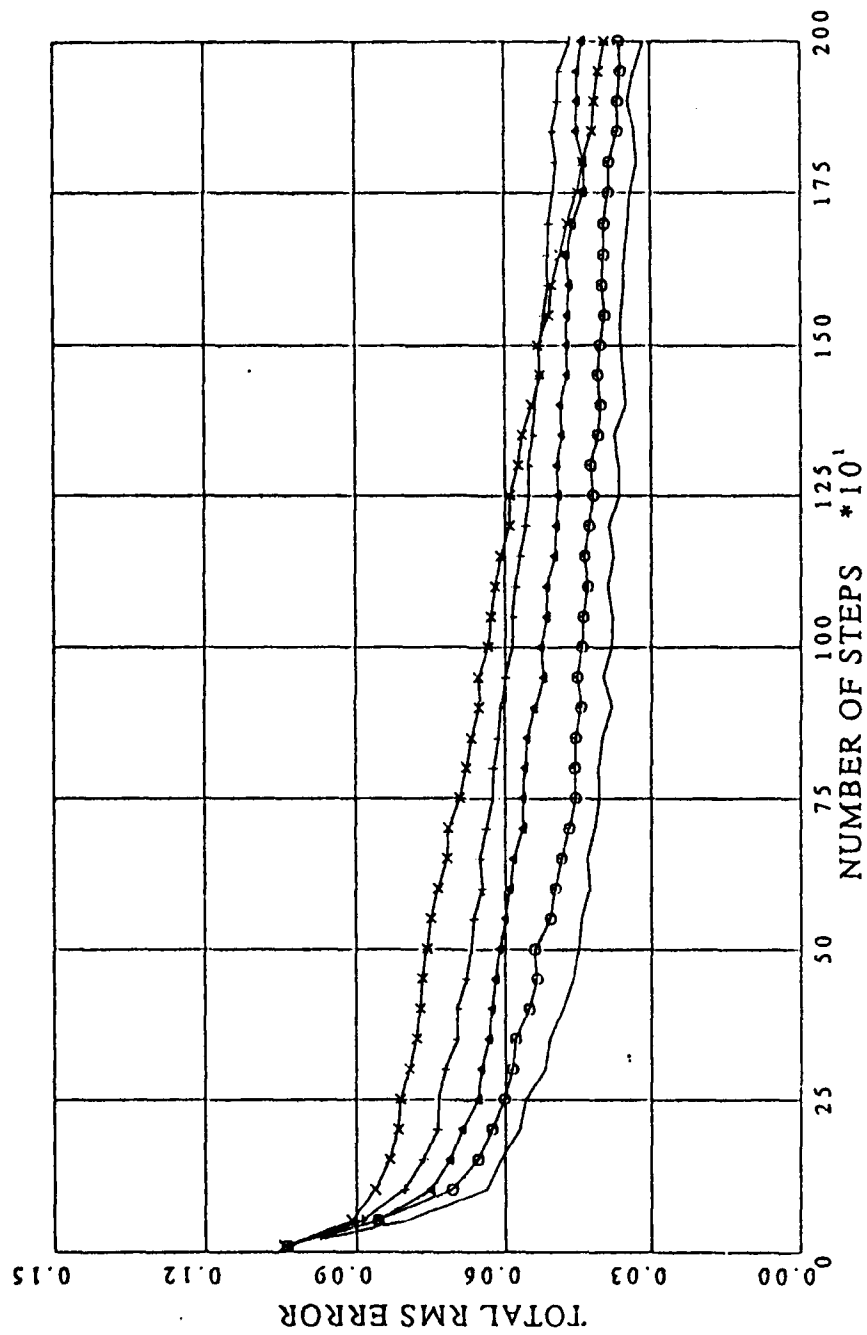


Figure 16

# NOISE TOLERANCE TEST

40% noise; 30% noise; 20% noise; 10% noise

5 km 10 km 15 km

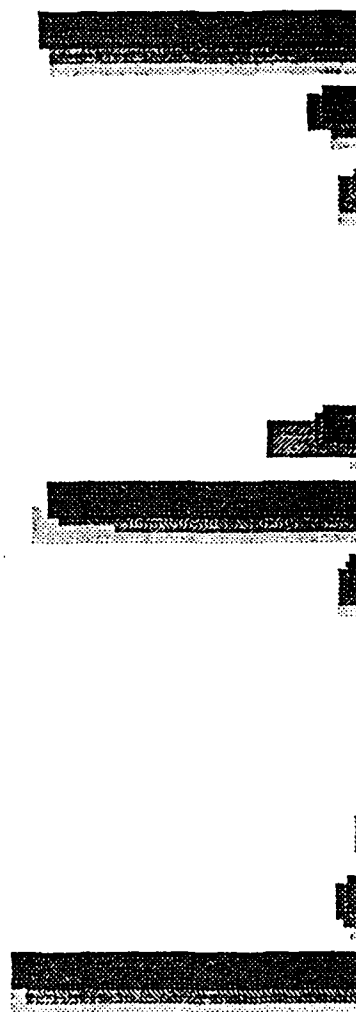


Figure 17

## **Chapter 6**

### **Discrimination Studies Using Regional Phases in the Central United States**

**by**

**M. Amjad and B.J. Mitchell**

## ABSTRACT

The usefulness of amplitude ratios discriminants in the central United States is systematically studied using signals from small earthquakes and explosions recorded at two broad-band stations operated by Saint Louis University. Signals are partitioned into passbands of 0-2 Hz, 2-4 Hz, 4-6 Hz, and 8-10 Hz. Ratios of different phases to one another and of one passband to another for the same phase were tested for 75 events presumed to be explosions and 40 events presumed to be earthquakes recorded at station FVM over the period May 1983 - June 1989. Ratios were determined for the whole signal as well as for the phases Pg, Sg, Lg, and Rg. Some of the ratios appear to provide useful discriminants, with the ability to discriminate increasing with increasing frequency.

Before correcting for instrument response, the amplitudes for earthquakes for the whole signal, Lg, and Rg tend to increase over the range 1-9 Hz and tend to decrease for explosions over the same range. None of the 75 explosions were found to have increasing amplitudes from 0 to 9 Hz on all three components for all three phases. Only 4 out of 40 earthquakes were found to have a decreasing trend on all three components for amplitudes of the same three phases. This variation of amplitudes is not affected by distance at distances between 20 and 340 km, or by source strength.

6 known explosions and 5 known earthquakes were recorded at the IRIS station CCM over the period September 1989 to November 1990. Using the criteria for discrimination suggested by the FVM data, all of these events would be correctly identified.

After correction for instrument responses, ratios at both stations FVM and CCM exhibit decreasing values of ground motion with increasing frequency, but the slope for explosions is significantly greater than that for earthquakes.

## INTRODUCTION

For the past few decades the focus of seismic research for verification of nuclear test ban treaties has been to develop methods for estimating the yield of nuclear explosions from seismic records at large distances. Seismic monitoring networks were installed to enhance the capabilities for better recording at large distances. Research related to nuclear test-ban treaties led to a number of discriminants for out-country verification (Pomeroy *et al.*, 1982), and the methods for estimating yields of large nuclear explosions (Blandford, 1982).

Recently, there have been new developments in test ban treaty negotiations between the U.S.S.R. and the U.S.A. These new developments in negotiations demand on-site verification, and deployment of in-country seismic monitoring capabilities for verification from in-country seismic records. In response to these developments in negotiations, and in anticipation of a range of new test ban treaties, nuclear test ban research has taken new directions. These include attempts to find discriminants between small

nuclear explosions and earthquakes, and to develop methods for estimating yield and source parameters of low yield events. Further research is likely to utilize suitable instruments at short distances, and will focus on finding appropriate discriminants between small explosions and small earthquakes, and on finding methods for estimating yield of small nuclear explosions. This study attempts to find suitable discrimination criteria to separate chemical explosions and earthquakes in the central United States. This region has been found to be similar to large areas of the Soviet Union for wave propagation studies (Sweeney *et al.*, 1986).

The New Madrid seismic zone is a seismically active region of the central United States. Most of the seismic activity occurs in a small region; however, many earthquakes occur in a broader region surrounding the New Madrid fault system. There is also much mining, and quarrying activity taking place in the same region. Most of the mining explosions and quarry blasts occur as strip mining for coal and quarrying for coal and quarrying for limestones, but other forms of surface mining also occur. In addition, underground mining activities for iron, lead, and coal are conducted.

Figure 1 shows the locations of earthquakes and explosions utilized in this study. They occur in the states of Missouri, Illinois, Indiana and Kentucky and were recorded in digital form at two stations, FVM and CCM, operated by Saint Louis University. The size of the explosions for quarry blasts range between 1 ton and 10 tons, and the size of the strip mine explosions range between 1 ton and 50 tons, with the exception of one or two explosions of about 100 Ktons. 10 to 30 small explosions occur every day. Data is available covering the distance range 5-340 km, both for earthquakes and chemical explosions. Comparative studies of signal characteristics can therefore be conducted using these sources. Station FVM has operated in a digital mode since 1980. CCM is an IRIS station (Incorporated Research Institutions for Seismology) installed by Saint Louis University in 1990.

The character of recorded ground motion depends on source parameters, instrument response, and the physical properties of the medium through which seismic waves propagate. The physical properties of the earth affect the seismic signal in various ways, e.g. by anelastic attenuation, scattering, and velocity structure of the crust. These physical properties are determined ultimately by the geology and tectonic setting of the region. Hence seismic records obtained in different regions differ in signal characteristics. It has been realized that discriminants which are useful in one region may not work in others.

The results of previous studies indicate that regional discriminants cannot be used with the same effectiveness everywhere. There seems to be a strong dependence on near-source geology and propagation path, which vary from region to region. Because of the strong regional bias in discrimination criteria, there is a need for a case-based approach to identify an unknown event, whether it is an explosion or earthquake. The most useful approach would be to compare the characteristics of an unknown event with the characteristics of known events in the same region. There is, therefore, a



need to find viable discriminants using known events from different geological regions. Baumgardt and Young (1990) have discussed the importance of a case based approach for discrimination.

### Data Collection and Processing

Data were collected for events at epicentral distances between 5 and 340 km from FVM and between 134 and 417 km from CCM. Seismograms were obtained for 75 presumed explosions and 40 presumed earthquakes recorded by the station FVM from 1983 to 1988 and by 5 known earthquakes and 6 known explosions recorded at CCM in 1989 and 1990. The locations of the stations and events are shown in Figure 1. Since there is no explosion data from the seismically active New Madrid seismic zone, no earthquakes were selected from that region. The magnitudes of the explosions range from 1.9 to 3.4 and the magnitudes of the earthquakes from 1.1 to 3.9. Example vertical-component records at station FVM for some of the events appear in Figure 2.

We rotated the horizontal component records into radial and transverse components. The onsets of the Pg, Sg, Pn and Sn phases were then picked manually and a one-second window was used from the start of the phase selected for analysis. This window was applied to avoid contamination from closely following phases. For the Lg phase, a fixed velocity window from 3.60 km/sec to 3.00 km/sec was used. For each event, radial, transverse and vertical component signals were filtered to obtain records in the frequency ranges 0 to 2 Hz, 2 to 4 Hz, 4 to 6 Hz, 6 to 8 Hz, and 8 to 10 Hz, using a zero-phase, two-pole, time-domain Butterworth filter.

### Tests of Possible Discriminants

We looked at three possible discriminants: (1) amplitude ratios using various phases, (2) ratios between lower and higher frequencies utilizing the same phase, and (3) the variation of amplitudes with frequency for individual seismograms. A summary of the significant results is given in the following paragraphs. A complete presentation of those results appears in Amjad (1991).

Amplitude ratios of various phases have been studied by several authors (e.g. Nuttli, 1981; Pomeroy *et al.*, 1982; Bennett and Murphy, 1986; Taylor *et al.*, 1989; Bennett *et al.*, 1989) with mixed results. In the present study, the ratios between different phases over the same frequency passband for the same component are calculated for Pg/Sg, Pg/Lg, Pg/Pn, Pg/Rg, Sg/Lg, Sg/Rg, Sg/Pn, Lg/Rg, Lg/Pn, and Rg/Pn phases. There are 10 possible ratios of different phases e.g. Pg/Sg for each frequency range. All these possible ratios for radial, transverse, and vertical components were determined as functions of distance and magnitude.

Although there is some suggestion of separation between earthquakes and explosions for some ratios in certain passbands, the separation is never clear-cut. The number of separated events vary from component to component for different phase ratios and for different frequency ranges. For

instance, the ratio  $S_g/R_g$  indicates some separation at higher frequencies, whereas the ratio  $P_g/R_g$  inhibits better separation at low frequencies. In most cases, if there is separation, it tends to increase for higher frequency passbands of 6-8 Hz and 8-10 Hz. Our results generally indicate, however, that the ratio of different phases with respect to each other is not an effective discrimination criterion in the central United States.

Ratios between lower and higher frequencies for regional phases were studied by Murphy and Bennett (1987) and Taylor *et al.* (1988) and were found to be useful in many cases. Bennett *et al.* (1989), however, reported less effectiveness in some regions than in others. In this study, maximum amplitudes, rms values, maximum spectral amplitudes, mean spectral amplitudes, and rms spectral values of  $P_g$ ,  $S_g$ ,  $P_n$  phases, and values of maximum amplitudes of whole signal, of  $L_g$  and  $R_g$  phases were measured. These measurements are made for the whole signal (0-10 Hz), and for 0-2 Hz, 2-4 Hz, 4-6 Hz, 6-8 Hz, and 8-10 Hz frequency passbands for radial, transverse and vertical components for all events. The 0-10 Hz/0-2 Hz, 0-10 Hz/2-4 Hz, 0-10 Hz/4-6 Hz, 0-10 Hz/6-8 Hz, 0-10 Hz/8-10 Hz, 0-2 Hz/2-4 Hz, 0-2 Hz/4-6 Hz, 0-2 Hz/6-8 Hz, 0-2 Hz/8-10 Hz, 2-4 Hz/4-6 Hz, 2-4 Hz/6-8 Hz, 2-4 Hz/8-10 Hz, 4-6 Hz/6-8 Hz, 4-6 Hz/8-10 Hz, and 6-8 Hz/8-10 Hz ratios for  $P_g$ ,  $S_g$ ,  $L_g$ ,  $R_g$ , and  $P_n$  were calculated for radial, transverse and vertical components. These ratios indicated some separation between earthquakes and explosions could be obtained, with best results occurring for the  $L_g$  and  $R_g$  phases.

Figure 3 illustrates results for the  $R_g$  phase recorded at FVM. The low frequency ratio places most explosions below most earthquakes whereas the high-frequency ratio shows the opposite relation. There is some overlap which cannot be explained, but it is possible that some events have been misidentified. A difficulty with  $R_g$  is that, while it can be a large phase for explosions, it can also be readily absorbed on transmission through low-Q material. This seems to have occurred for several of the explosion events shown in Figure 2. Similar separations in ratios in Figure 3 were, however, also observed for  $L_g$  as recorded on all three components.

The most promising discriminant which we found relies on the variation of amplitudes with frequency. After correcting for instrument response, the amplitude decreases with increasing frequency is always greater than that for explosions. Figure 4 shows results for  $L_g$  waves using vertical-component recordings. Similar results were found for radial and transverse components of  $L_g$  and for all components of  $R_g$ .

### Conclusions

Using ratios of different passbands for the same phase is more promising than using ratios of different phases for the same passband in discriminating between earthquakes and explosions in the central United States. The variation of amplitudes with frequency between the 0-2 Hz and 6-8 Hz passbands, however, is the most promising discriminant for found in our study. It appears to apply to all phases, with best results likely to be obtained for the  $L_g$  and  $R_g$  phases.

## References

- Amjad, M., Discrimination between earthquakes and explosions in the central United States, Ph.D. Diss., Saint Louis University, 243 pp., 1991.
- Baumgardt, D.R., and G.B. Young, Regional seismic waveform discriminants and case-based event identification using regional arrays, *Bull. Seism. Soc. Am.*, 80, 1874-1892, 1990.
- Bennett, T.J. and J.R. Murphy, Analysis of seismic discrimination capabilities using regional data from western United States events, *Bull. Seism. Soc. Am.*, 76, 1069-1086, 1986.
- Bennett, T.J., B.W. Barker, K.L. McLaughlin, and J.R. Murphy, Regional discrimination of quarry blasts, earthquakes and underground nuclear explosions, Final Report, GL-TR-89-0114, S-Cubed, La Jolla, CA, 1989. ADA223148
- Blandford, R.R., Seismic event discrimination, *Bull. Seism. Soc. Am.*, 72, S69-S87, 1982.
- Murphy, J., and T. Bennett, A discrimination analysis of short-period regional seismic data recorded at Tonto Forest Observatory, *Bull. Seism. Soc. Am.*, 72, 1351-1366, 1982.
- Nuttli, O.W., On the use of Lg waves in western and central Asia and their use as a discriminant between earthquakes and explosions, *Bull. Seism. Soc. Am.*, 71, 249-262, 1981.
- Pomeroy, P.W., W.J. Best, and T.V. McEvilly, Test ban treaty verification with regional data - a review, *Bull. Seism. Soc. Am.*, 72, S89-S129, 1982.
- Sweeney, J.J., P. Harber, and D. Harris, North American Geophysical Analogs to the USSR: Implications for siting seismic verification stations, Treaty Verification Program, Lawrence Livermore National Laboratory, 28 pp, 1986.
- Taylor, S.R., N.W. Sherman, and M.D. Denny, Spectral discrimination between NTS explosions and western United States earthquakes at regional distances, *Bull. Seism. Soc. Am.*, 78, 1563-1579, 1988.
- Taylor, S.R., M.D. Denny, E.S. Vergino, and R.E. Glaser, Regional discrimination between NTS explosions and western United States earthquakes, *Bull. Seism. Soc. Am.*, 79, 1142-1176, 1989.

### Figure Captions

Figure 1. Map of area of study showing locations of seismic stations (FVM and CCM), explosions, and earthquakes.

Figure 2. Example vertical-component seismograms generated by explosions (left) and earthquakes (right) as recorded at station FVM.

Figure 3. Ratios of Rg amplitudes at various frequencies versus distance as determined from vertical-component records.

Figure 4. Normalized Lg amplitude variations for the vertical component after correcting for instrument response. (Top) Amplitude variations at CCM for explosions (left) and earthquakes (right). (Bottom) Amplitude variations at FVM for explosions (left) and earthquakes (right).

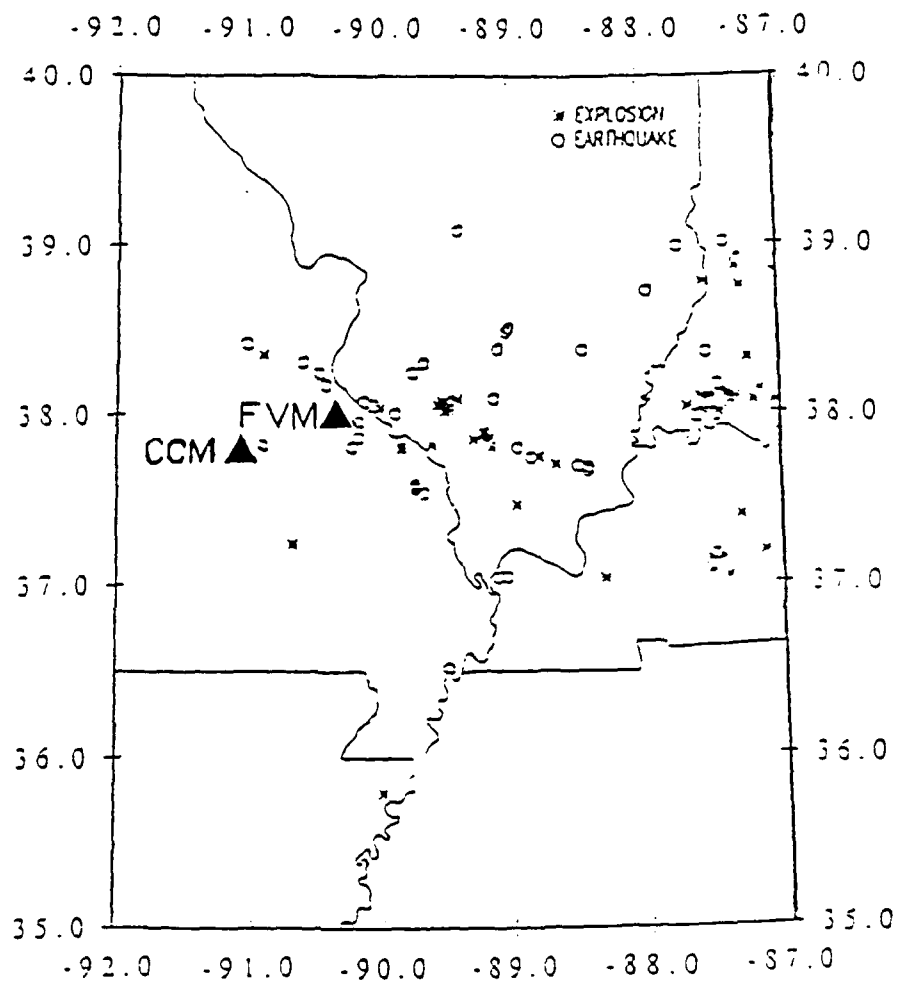


Figure 1

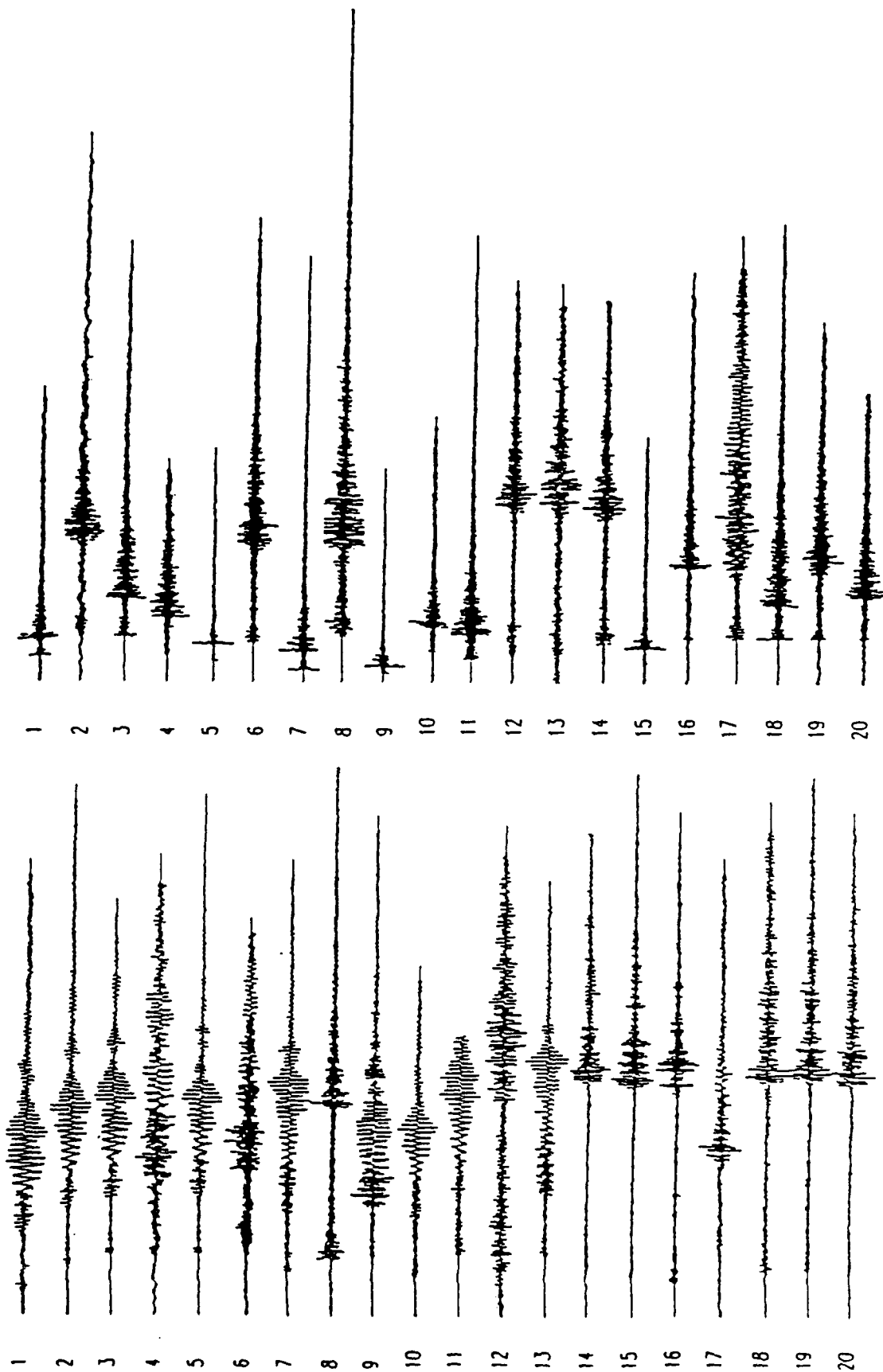


Figure 2

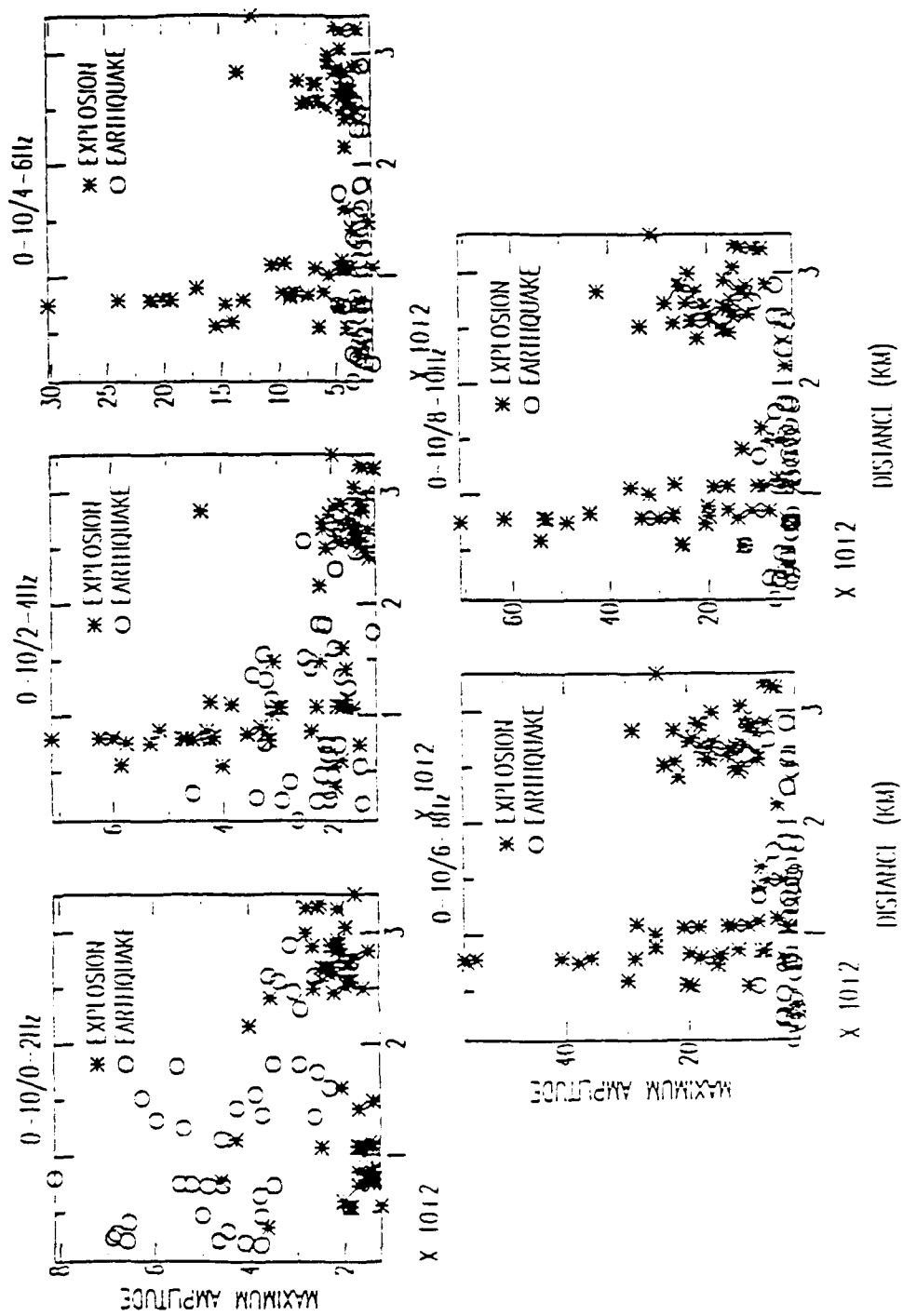


Figure 3

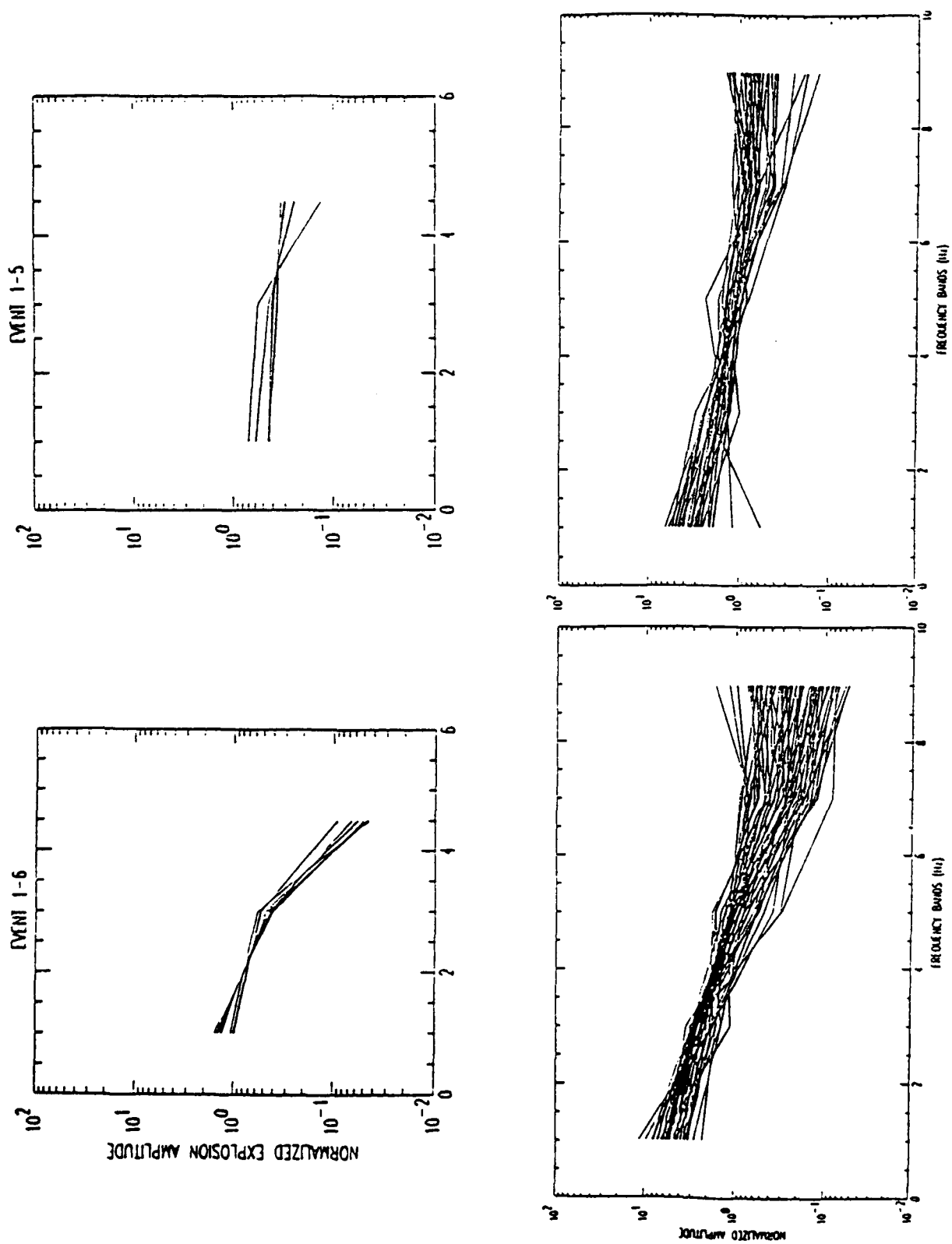


Figure 4



Prof. Thomas Ahrens  
Seismological Lab, 252-21  
Division of Geological & Planetary Sciences  
California Institute of Technology  
Pasadena, CA 91125

Prof. Keiiti Aki  
Center for Earth Sciences  
University of Southern California  
University Park  
Los Angeles, CA 90089-0741

Prof. Shelton Alexander  
Geosciences Department  
403 Deike Building  
The Pennsylvania State University  
University Park, PA 16802

Dr. Ralph Alewine, III  
DARPA/NMRO  
3701 North Fairfax Drive  
Arlington, VA 22203-1714

Prof. Charles B. Archambeau  
CIRES  
University of Colorado  
Boulder, CO 80309

Dr. Thomas C. Bache, Jr.  
Science Applications Int'l Corp.  
10260 Campus Point Drive  
San Diego, CA 92121 (2 copies)

Prof. Muawia Barazangi  
Institute for the Study of the Continent  
Cornell University  
Ithaca, NY 14853

Dr. Jeff Barker  
Department of Geological Sciences  
State University of New York  
at Binghamton  
Vestal, NY 13901

Dr. Douglas R. Baumgardt  
ENSCO, Inc  
5400 Port Royal Road  
Springfield, VA 22151-2388

Dr. Susan Beck  
Department of Geosciences  
Building #77  
University of Arizona  
Tucson, AZ 85721

Dr. T.J. Bennett  
S-CUBED  
A Division of Maxwell Laboratories  
11800 Sunrise Valley Drive, Suite 1212  
Reston, VA 22091

Dr. Robert Blandford  
AFTAC/TT, Center for Seismic Studies  
1300 North 17th Street  
Suite 1450  
Arlington, VA 22209-2308

Dr. G.A. Bollinger  
Department of Geological Sciences  
Virginia Polytechnical Institute  
21044 Derring Hall  
Blacksburg, VA 24061

Dr. Stephen Bratt  
Center for Seismic Studies  
1300 North 17th Street  
Suite 1450  
Arlington, VA 22209-2308

Dr. Lawrence Burdick  
Woodward-Clyde Consultants  
566 El Dorado Street  
Pasadena, CA 91109-3245

Dr. Robert Burrige  
Schlumberger-Doll Research Center  
Old Quarry Road  
Ridgefield, CT 06877

Dr. Jerry Carter  
Center for Seismic Studies  
1300 North 17th Street  
Suite 1450  
Arlington, VA 22209-2308

Dr. Eric Chael  
Division 9241  
Sandia Laboratory  
Albuquerque, NM 87185

Prof. Vernon F. Cormier  
Department of Geology & Geophysics  
U-45, Room 207  
University of Connecticut  
Storrs, CT 06268

Prof. Steven Day  
Department of Geological Sciences  
San Diego State University  
San Diego, CA 92182

Marvin Denny  
U.S. Department of Energy  
Office of Arms Control  
Washington, DC 20585

Dr. Zoltan Der  
ENSCO, Inc.  
5400 Port Royal Road  
Springfield, VA 22151-2388

Prof. Adam Dziewonski  
Hoffman Laboratory, Harvard University  
Dept. of Earth Atmos. & Planetary Sciences  
20 Oxford Street  
Cambridge, MA 02138

Prof. John Ebel  
Department of Geology & Geophysics  
Boston College  
Chestnut Hill, MA 02167

Eric Fielding  
SNEE Hall  
INSTOC  
Cornell University  
Ithaca, NY 14853

Dr. Mark D. Fisk  
Mission Research Corporation  
735 State Street  
P.O. Drawer 719  
Santa Barbara, CA 93102

Prof Stanley Flatte  
Applied Sciences Building  
University of California, Santa Cruz  
Santa Cruz, CA 95064

Dr. John Foley  
NER-Geo Sciences  
1100 Crown Colony Drive  
Quincy, MA 02169

Prof. Donald Forsyth  
Department of Geological Sciences  
Brown University  
Providence, RI 02912

Dr. Art Frankel  
U.S. Geological Survey  
922 National Center  
Reston, VA 22092

Dr. Cliff Frolich  
Institute of Geophysics  
8701 North Mopac  
Austin, TX 78759

Dr. Holly Given  
IGPP, A-025  
Scripps Institute of Oceanography  
University of California, San Diego  
La Jolla, CA 92093

Dr. Jeffrey W. Given  
SAIC  
10260 Campus Point Drive  
San Diego, CA 92121

Dr. Dale Glover  
Defense Intelligence Agency  
ATTN: ODT-1B  
Washington, DC 20301

Dr. Indra Gupta  
Teledyne Geotech  
314 Montgomery Street  
Alexandria, VA 22314

Dan N. Hagedon  
Pacific Northwest Laboratories  
Battelle Boulevard  
Richland, WA 99352

Dr. James Hannon  
Lawrence Livermore National Laboratory  
P.O. Box 808  
L-205  
Livermore, CA 94550

Dr. Roger Hansen  
HQ AFTAC/TTR  
Patrick AFB, FL 32925-6001

Prof. David G. Harkrider  
Seismological Laboratory  
Division of Geological & Planetary Sciences  
California Institute of Technology  
Pasadena, CA 91125

Prof. Danny Harvey  
CIRES  
University of Colorado  
Boulder, CO 80309

Prof. Donald V. Helmberger  
Seismological Laboratory  
Division of Geological & Planetary Sciences  
California Institute of Technology  
Pasadena, CA 91125

Prof. Eugene Herrin  
Institute for the Study of Earth and Man  
Geophysical Laboratory  
Southern Methodist University  
Dallas, TX 75275

Prof. Robert B. Herrmann  
Department of Earth & Atmospheric Sciences  
St. Louis University  
St. Louis, MO 63156

Prof. Lane R. Johnson  
Seismographic Station  
University of California  
Berkeley, CA 94720

Prof. Thomas H. Jordan  
Department of Earth, Atmospheric &  
Planetary Sciences  
Massachusetts Institute of Technology  
Cambridge, MA 02139

Prof. Alan Kafka  
Department of Geology & Geophysics  
Boston College  
Chestnut Hill, MA 02167

Robert C. Kemerait  
ENSCO, Inc.  
445 Pineda Court  
Melbourne, FL 32940

Dr. Max Koontz  
U.S. Dept. of Energy/DP 5  
Forrestal Building  
1000 Independence Avenue  
Washington, DC 20585

Dr. Richard LaCoss  
MIT Lincoln Laboratory, M-200B  
P.O. Box 73  
Lexington, MA 02173-0073

Dr. Fred K. Lamb  
University of Illinois at Urbana-Champaign  
Department of Physics  
1110 West Green Street  
Urbana, IL 61801

Prof. Charles A. Langston  
Geosciences Department  
403 Deike Building  
The Pennsylvania State University  
University Park, PA 16802

Jim Lawson, Chief Geophysicist  
Oklahoma Geological Survey  
Oklahoma Geophysical Observatory  
P.O. Box 8  
Leonard, OK 74043-0008

Prof. Thorne Lay  
Institute of Tectonics  
Earth Science Board  
University of California, Santa Cruz  
Santa Cruz, CA 95064

Dr. William Leith  
U.S. Geological Survey  
Mail Stop 928  
Reston, VA 22092

Mr. James F. Lewkowicz  
Phillips Laboratory/GPEH  
Hanscom AFB, MA 01731-5000( 2 copies)

Mr. Alfred Lieberman  
ACDA/VI-OA State Department Building  
Room 5726  
320-21st Street, NW  
Washington, DC 20451

Prof. L. Timothy Long  
School of Geophysical Sciences  
Georgia Institute of Technology  
Atlanta, GA 30332

Dr. Randolph Martin, III  
New England Research, Inc.  
76 Olcott Drive  
White River Junction, VT 05001

Dr. Robert Masse  
Denver Federal Building  
Box 25046, Mail Stop 967  
Denver, CO 80225

Dr. Gary McCartor  
Department of Physics  
Southern Methodist University  
Dallas, TX 75275

Prof. Thomas V. McEvilly  
Seismographic Station  
University of California  
Berkeley, CA 94720

Dr. Art McGarr  
U.S. Geological Survey  
Mail Stop 977  
U.S. Geological Survey  
Menlo Park, CA 94025

Dr. Keith L. McLaughlin  
S-CUBED  
A Division of Maxwell Laboratory  
P.O. Box 1620  
La Jolla, CA 92038-1620

Stephen Miller & Dr. Alexander Florence  
SRI International  
333 Ravenswood Avenue  
Box AF 116  
Menlo Park, CA 94025-3493

Prof. Bernard Minster  
IGPP, A-025  
Scripps Institute of Oceanography  
University of California, San Diego  
La Jolla, CA 92093

Prof. Brian J. Mitchell  
Department of Earth & Atmospheric Sciences  
St. Louis University  
St. Louis, MO 63156

Mr. Jack Murphy  
S-CUBED  
A Division of Maxwell Laboratory  
11800 Sunrise Valley Drive, Suite 1212  
Reston, VA 22091 (2 Copies)

Dr. Keith K. Nakanishi  
Lawrence Livermore National Laboratory  
L-025  
P.O. Box 808  
Livermore, CA 94550

Dr. Carl Newton  
Los Alamos National Laboratory  
P.O. Box 1663  
Mail Stop C335, Group ESS-3  
Los Alamos, NM 87545

Dr. Bao Nguyen  
HQ AFTAC/TTR  
Patrick AFB, FL 32925-6001

Prof. John A. Orcutt  
IGPP, A-025  
Scripps Institute of Oceanography  
University of California, San Diego  
La Jolla, CA 92093

Prof. Jeffrey Park  
Kline Geology Laboratory  
P.O. Box 6666  
New Haven, CT 06511-8130

Dr. Howard Patton  
Lawrence Livermore National Laboratory  
L-025  
P.O. Box 808  
Livermore, CA 94550

Dr. Frank Pilotte  
HQ AFTAC/TTR  
Patrick AFB, FL 32925-6001

Dr. Jay J. Pulli  
Radix Systems, Inc.  
2 Taft Court, Suite 203  
Rockville, MD 20850

Dr. Robert Reinke  
ATTN: FCTVTD  
Field Command  
Defense Nuclear Agency  
Kirtland AFB, NM 87115

Prof. Paul G. Richards  
Lamont-Doherty Geological Observatory  
of Columbia University  
Palisades, NY 10964

Mr. Wilmer Rivers  
Teledyne Geotech  
314 Montgomery Street  
Alexandria, VA 22314

Dr. George Rothe  
HQ AFTAC/TTR  
Patrick AFB, FL 32925-6001

Dr. Alan S. Ryall, Jr.  
DARPA/NMRO  
3701 North Fairfax Drive  
Arlington, VA 22209-1714

Dr. Richard Sailor  
TASC, Inc.  
55 Walkers Brook Drive  
Reading, MA 01867

Prof. Charles G. Sammis  
Center for Earth Sciences  
University of Southern California  
University Park  
Los Angeles, CA 90089-0741

Prof. Christopher H. Scholz  
Lamont-Doherty Geological Observatory  
of Columbia University  
Palisades, CA 10964

Dr. Susan Schwartz  
Institute of Tectonics  
1156 High Street  
Santa Cruz, CA 95064

Secretary of the Air Force  
(SAFRD)  
Washington, DC 20330

Office of the Secretary of Defense  
DDR&E  
Washington, DC 20330

Thomas J. Sereno, Jr.  
Science Application Int'l Corp.  
10260 Campus Point Drive  
San Diego, CA 92121

Dr. Michael Shore  
Defense Nuclear Agency/SPSS  
6801 Telegraph Road  
Alexandria, VA 22310

Dr. Matthew Sibol  
Virginia Tech  
Seismological Observatory  
4044 Derring Hall  
Blacksburg, VA 24061-0420

Prof. David G. Simpson  
IRIS, Inc.  
1616 North Fort Myer Drive  
Suite 1440  
Arlington, VA 22209

Donald L. Springer  
Lawrence Livermore National Laboratory  
L-025  
P.O. Box 808  
Livermore, CA 94550

Dr. Jeffrey Stevens  
S-CUBED  
A Division of Maxwell Laboratory  
P.O. Box 1620  
La Jolla, CA 92038-1620

Lt. Col. Jim Stobie  
ATTN: AFOSR/NL  
Bolling AFB  
Washington, DC 20332-6448

Prof. Brian Stump  
Institute for the Study of Earth & Man  
Geophysical Laboratory  
Southern Methodist University  
Dallas, TX 75275

Prof. Jeremiah Sullivan  
University of Illinois at Urbana-Champaign  
Department of Physics  
1110 West Green Street  
Urbana, IL 61801

Prof. L. Sykes  
Lamont-Doherty Geological Observatory  
of Columbia University  
Palisades, NY 10964

Dr. David Taylor  
ENSCO, Inc.  
445 Pineda Court  
Melbourne, FL 32940

Dr. Steven R. Taylor  
Los Alamos National Laboratory  
P.O. Box 1663  
Mail Stop C335  
Los Alamos, NM 87545

Prof. Clifford Thurber  
University of Wisconsin-Madison  
Department of Geology & Geophysics  
1215 West Dayton Street  
Madison, WI 53706

Prof. M. Nafi Toksoz  
Earth Resources Lab  
Massachusetts Institute of Technology  
42 Carleton Street  
Cambridge, MA 02142

Dr. Larry Turnbull  
CIA-OSWR/NED  
Washington, DC 20505

DARPA/RMO/SECURITY OFFICE  
3701 North Fairfax Drive  
Arlington, VA 22203-1714

Dr. Gregory van der Vink  
IRIS, Inc.  
1616 North Fort Myer Drive  
Suite 1440  
Arlington, VA 22209

HQ DNA  
ATTN: Technical Library  
Washington, DC 20305

Dr. Karl Veith  
EG&G  
5211 Auth Road  
Suite 240  
Suitland, MD 20746

Defense Intelligence Agency  
Directorate for Scientific & Technical Intelligence  
ATTN: DTIB  
Washington, DC 20340-6158

Prof. Terry C. Wallace  
Department of Geosciences  
Building #77  
University of Arizona  
Tuscon, AZ 85721

Defense Technical Information Center  
Cameron Station  
Alexandria, VA 22314 (2 Copies)

Dr. Thomas Weaver  
Los Alamos National Laboratory  
P.O. Box 1663  
Mail Stop C335  
Los Alamos, NM 87545

TACTEC  
Battelle Memorial Institute  
505 King Avenue  
Columbus, OH 43201 (Final Report)

Dr. William Wortman  
Mission Research Corporation  
8560 Cinderbed Road  
Suite 700  
Newington, VA 22122

Phillips Laboratory  
ATTN: XPG  
Hanscom AFB, MA 01731-5000

Prof. Francis T. Wu  
Department of Geological Sciences  
State University of New York  
at Binghamton  
Vestal, NY 13901

Phillips Laboratory  
ATTN: GPE  
Hanscom AFB, MA 01731-5000

AFTAC/CA  
(STINFO)  
Patrick AFB, FL 32925-6001

Phillips Laboratory  
ATTN: TSML  
Hanscom AFB, MA 01731-5000

DARPA/PM  
3701 North Fairfax Drive  
Arlington, VA 22203-1714

Phillips Laboratory  
ATTN: SUL  
Kirtland, NM 87117 (2 copies)

DARPA/RMO/RETRIEVAL  
3701 North Fairfax Drive  
Arlington, VA 22203-1714

Dr. Michel Bouchon  
I.R.I.G.M.-B.P. 68  
38402 St. Martin D'Herès  
Cedex, FRANCE

Dr. Michel Campillo  
Observatoire de Grenoble  
I.R.I.G.M.-B.P. 53  
38041 Grenoble, FRANCE

Dr. Jorg Schlittenhardt  
Federal Institute for Geosciences & Nat'l Res.  
Postfach 510153  
D-3000 Hannover 51, GERMANY

Dr. Kin Yip Chun  
Geophysics Division  
Physics Department  
University of Toronto  
Ontario, CANADA

Dr. Johannes Schweitzer  
Institute of Geophysics  
Ruhr University/Bochum  
P.O. Box 1102148  
4360 Bochum 1, GERMANY

Prof. Hans-Peter Harjes  
Institute for Geophysic  
Ruhr University/Bochum  
P.O. Box 102148  
4630 Bochum 1, GERMANY

Prof. Eystein Husebye  
NTNF/NORSAR  
P.O. Box 51  
N-2007 Kjeller, NORWAY

David Jepsen  
Acting Head, Nuclear Monitoring Section  
Bureau of Mineral Resources  
Geology and Geophysics  
G.P.O. Box 378, Canberra, AUSTRALIA

Ms. Eva Johannisson  
Senior Research Officer  
National Defense Research Inst.  
P.O. Box 27322  
S-102 54 Stockholm, SWEDEN

Dr. Peter Marshall  
Procurement Executive  
Ministry of Defense  
Blacknest, Brimpton  
Reading RG7-6FRS, UNITED KINGDOM

Dr. Bernard Massinon, Dr. Pierre Mechler  
Societe Radiomana  
27 rue Claude Bernard  
75005 Paris, FRANCE (2 Copies)

Dr. Svein Mykkeltveit  
NTNF/NORSAR  
P.O. Box 51  
N-2007 Kjeller, NORWAY (3 Copies)

Prof. Keith Priestley  
University of Cambridge  
Bullard Labs, Dept. of Earth Sciences  
Madingley Rise, Madingley Road  
Cambridge CB3 0EZ, ENGLAND